COMPARISON OF SIMULATIONS AND DATA FROM SMALL HIGH VOLTAGE SINGLE CRYSTAL DETECTORS FOR DARK MATTER SEARCHES

A Dissertation

by

ELHAM AZADBAKHT

Submitted to the Graduate and Professional School of
Texas A&M University
in partial fulfillment of the requirements for the degree of

DOCTOR OF PHILOSOPHY

Chair of Committee,	David Toback
Committee Members,	Bhaskar Dutta
	Ricardo Eusebi
	Yossef Elabd
Head of Department,	Grigory Rogachev

December 2022

Major Subject: Physics

Copyright 2022 Elham Azadbakht

ABSTRACT

Numerous astronomical observations suggest that dark matter is a new type of particle and makes up the majority of the mass in the Universe. Still, its discovery and further understanding of its nature remain one of the most significant open questions in all of science. Using combined semiconductor and superconducting technologies, the SuperCDMS experiment has set world-leading limits on small-mass dark matter interactions. However, the ability to extend the sensitivity further is limited by the lack of a full understanding of how detectors respond to $\mathcal{O}(1\ \mathrm{eV})$ interactions. In this thesis, we study the response of small high voltage detectors to photon interactions from a laser using simulations. We present a comparison between the full simulation results and the experimental data demonstrating that the SuperCDMS simulation successfully reproduces the main features of the data and can be used in conducting simulation-based dark matter searches.

ACKNOWLEDGMENTS

It truly takes more than a village to finish a PhD dissertation, especially in experimental high energy physics where everything is highly interconnected. This work is built upon the work of many former and current members of the Cryogenic Dark Matter Search (CDMS) experiment and it would have not been possible without their direct and indirect contributions. Although it would be impossible to mention all names, I want to express my deep gratitude to anyone who has contributed to the CDMS/SuperCDMS experiments since 1998.

First of all, I would like to thank my advisor, Dave Toback. I could not ask for a better advisor/mentor for this journey. From day one, Dave has been immensely supportive and his constant guidance and mentorship during the last six years has played a central role in my personal and professional development. I am sincerely grateful for all I have learned from him; from how to be a scientist to always striving for excellence in your work. Furthermore, I deeply appreciate his constant effort in fostering a positive and open work environment for everyone in our group; working in Toback Group has been a great honor and privilege.

I would also like to thank my committee members, Bhaskar Dutta, Ricardo Eusebi, and Yossef Elabd for finding the time to provide feedback on this work despite their busy schedules. In addition, I deeply appreciate Mahmoud El-Halwagi for attending my thesis defense and asking great questions!

I think our group at Texas A&M University is so lucky to have Mike Kelsey! I am very grateful for all his amazing work on the SuperCDMS simulation. Mike has always been there to patiently help with any computing/physics questions and provide constructive feedback. I owe much of what I know about physics and computing to Mike.

Working closely with Ziqing Hong and learning from him was one of the reasons that I decided to work on the HVeV experiment. I am so happy that I made this decision. It was truly fun to work with Ziqing. Especially, I enjoyed the times that I made too simplifying assumptions about the experiment and he reminded me that real experiments are much more complicated than simulations!

I would like to thank Toback group members including Jon Wilson, Jorge Morales, Xuji Zhao, Richard Lawrence, and Josh Winchell, for welcoming me to the group. I have learned a lot from each one of them. Particularly, during the first years when I knew absolutely nothing about high energy physics and how it is done. Later on, I worked closely with Lei Zheng, McKay Osborne, Bhattacharyya, and Warren Perry. Thank you all for being great team/lab mates and taking over some of the tasks that I was working on so I can graduate! Additionally, Iman Ataee has been a great help in solving any computing issues I have faced using the Texas A&M High Performance Research Computing.

Because of the collaborative nature of this work, I have had the privilege to work with and learn from many SuperCDMS collaborators in the US, Canada, and Germany. I would like to thank Ben Smith, Belina von Krosigk, Scott Oser, Sten Hansen, Patrick Lukens, and Jamieson Olsen for their help in DAQ, triggering, and electronics projects. The experimental data presented in this work was collected and analyzed by the HVeV Run 2 folks at Northwestern University and Fermi National Lab including Matt Wilson, Yen-Yung Chang, Valentina Novati, Ziqing Hong, Noah Kurinsky, Brian Nebolsky, Tom Ren, Doug Pinckney, Nader Mirabolfathi, Rupak Mahapatra, Mark Platt, Belina von Krosigk, Miriam Diamond, Enectali (Tali) Figueroa-Feliciano, Francisco Ponce and Elizabeth Wills. I am thankful for their amazing work which made this work possible. Particularly, I would like to thank Tom Ren for helping me with any questions I had about the processing software. Additionally, I thank Tarek Saab, Raymond Bunker, Stefan Zatschler, and Birgtit Zatschler for their feedback during HVeV-DMC meetings.

I would like to express my gratitude to my amazing mentor, Catherine Lefebvre. Catherine has been incredibly helpful in planning my next steps and navigating my transition from high energy physics to quantum computing. I sincerely appreciate all her kind support and encouragement during the final years of my PhD. On a more personal note, I would like to thank my incredible friends, Aysan, Negin, Shahrzad, and Saeed for supporting me through the years and listening to my countless complaints about graduate school. Furthermore, Zahra Nazari has been an inspiration to me and a terrific role model for me since I was a young child, and for that I want to thank her.

I do not even know how to thank my amazing parents for all of their love, dedication, and hard work in building our family. I still remember the times when I was in elementary school and my mom used to spend hours with me solving math puzzles (which later on translated to an interest in physics) and my dad would drive 50 miles to a bigger city to get the books that I wanted. Additionally, I want to thank my siblings, Sarvin and Amin. Their presence brings joy to my life.

Finally, I would like to thank Reza for his unwavering support during the ups and downs of my PhD life and for inspiring me to grow as a person and preserve during challenging times. Without him, it would have been much harder (or even impossible) to cross the finish line. I am forever grateful for everything he has done for me.

CONTRIBUTORS AND FUNDING SOURCES

Contributors

This work was supported by a dissertation committee consisting of Professors David Toback [advisor], Bhaskar Dutta, and Ricardo Eusebi members of the Department of Physics and Astronomy and the Mitchell Institute for Fundamental Physics and Astronomy and Professor as well as Mahmoud El-Halwagi and Yossef Elabd of the Department of Chemical Engineering.

All work for the dissertation was completed by the student, under the advisement of Prof. David Toback of the Department of Physics and Astronomy, and in collaboration with the members of the SuperCDMS Experiment and the NEXUS Collaboration.

Funding Sources

This work was supported by the U.S. Department of Energy (DOE), through a research grant for the SuperCDMS Experiment and in part by the Mitchell Institute for Fundamental Physics and Astronomy as well as a Teaching Assistantship from Texas A&M University. Additionally, portions of this research were conducted with the advanced computing resources provided by Texas A&M High Performance Research Computing and the Texas A&M Brazos Cluster.

TABLE OF CONTENTS

Page

ABSTRACT ii

ACKNOWLEDGMENTS iii

CONTRIBUTORS AND FUNDING SOURCES vi

TABLE OF CONTENTS vii

LIST OF FIGURES x

LIST OF TABLES xxv

1. Introduction and Motivation 1

    1.1 Evidence for Dark Matter and its Particle Nature 3
        1.1.1 Luminous Mass in a Galaxy and the Motion of the Stars Around its Center 4
        1.1.2 Gravitational Lensing, Einstein Rings, and the Bullet Cluster 5
        1.1.3 Measurements of the Cosmic Microwave Background 8
    1.2 Dark Matter Properties 10
    1.3 Overview of the Dark Matter Detection Methods 10
    1.4 Detector Concept: Making Dark Matter Detectors from a Single-Crystal Semiconductor and Superconducting Sensors 12
    1.5 HVeV Detectors and Motivations 14
    1.6 The need for Understanding the Physics of HVeV Detectors, Advantages of Using Simulations and the Goals of this Thesis 15
    1.7 Overview of the HVeV Laser Calibration Experiment 15
    1.8 Overview and Outline of this Thesis 18

2. Physics of Single-Crystal Semiconductors and Lattice Response to Photon Interactions 20

    2.1 Conduction and Valence Band Structure 21
        2.1.1 Using Semiconductors for Particle Detection 23
    2.2 Charge Creation and Lattice Vibration (Phonons) in Single Particle Interactions 23
    2.3 Effects of Applying a Voltage Bias to the Crystal: Luke Phonon Creation 26
    2.4 Charge and Phonon Propagation in the Crystal 28
    2.5 Two Mechanisms that Effect the Total Collected Energy: Charge Trapping and Additional Charge Liberation (Impact Ionization) 32
    2.6 Summary: Photon Interaction with the Single-Crystal Semiconductors Under Voltage Bias 32

3. Physics of Superconducting Sensors and Readout 35

- 3.1 Overview of Superconductivity 35
- 3.2 Quasiparticle-assisted Electrothermal-feedback Transition Edge Sensors (QETs) 36
- 3.3 Transition Edge Sensor (TES) 38
- 3.4 Phonon Energy Readout of the TES 40

4. HVeV Detector and Readout Electronics Design 43

- 4.1 Detector Design Parameters 44
- 4.2 Readout Electronics and Data Acquisition 48
- 4.3 Events, Triggering and the Phonon Energy Reconstruction from the TES Readout 50

5. HVeV Laser Calibration Experiment and Results 55

- 5.1 NEXUS Facility, HVeV and Laser Experimental Setup, and Data Taking Period 55
- 5.2 Phonon Energy Calibration 57
- 5.3 Event Selection Criteria 58
- 5.4 Main Features of the HVeV Phonon Energy Spectrum, and a Simple Model 62

6. Simulation of the HVeV Laser Calibration Experiment 67

- 6.1 Overview and Goals of a Full Simulation 67
- 6.2 Simulating Photons from a Laser Source: SourceSim 69
- 6.3 Detector Response to Energy Deposits from Photons: CrystalSim 70
  - 6.3.1 Phonon and Charge Creation and Propagation Under Voltage Bias 70
  - 6.3.2 Impact Ionization and Charge Trapping 71
- 6.4 Phonon Readout Sensor Response: TESSim 72
- 6.5 Readout Electronics, Data Acquisition, and Noise: DAQSim and NoiseSim 73

7. Simulation Results for Single-Photon Interactions 74

- 7.1 Overview of the Simulation Configuration 74
- 7.2 Detector Response 77
  - 7.2.1 Total Collected Phonon Energy in the Crystal 77
  - 7.2.2 Pulse Simulation Results: TES, DAQ, and Noise Simulation 80
- 7.3 Results After Adding Charge Trapping and Impact Ionization Effects 84
- 7.4 Results After Adding Noise and Running the Simulated Data Through Reconstruction Software 86

8. Simulation Results for Multiple-Photon Interactions 87

- 8.1 Detector Response 87
  - 8.1.1 Total Collected Phonon Energy in the Crystal as a Function of the Number of Incident Photons 90
  - 8.1.2 Example Results for a Laser that Emits Photons According to a Poisson Distribution 91

8.2 Results After Adding Charge Trapping and Impact Ionization Effects 93
8.3 Results after Adding Noise and Running the Simulated Data Through Reconstruction Software 93
8.4 The Trigger Response as a Function of Energy 95
8.5 Contributions to the Energy Measurement Resolution 97

9. Comparison of the HVeV Laser Data to the Simulation 102

9.1 Overview of Simulation Parameters and Additional Tools Used for Reproducing the HVeV Laser Spectrum 102
9.2 First Comparison of Data and Simulation and Moving to a Custom Laser Model 105
9.3 Describing How we Determined the Final Parameter Values 108
    9.3.1 Weights for Combining Samples 108
    9.3.2 Trigger Threshold 108
    9.3.3 Charge Trapping and Impact Ionization Mean Free Path 110
    9.3.4 Energy Calibration 113
    9.3.5 Additional Energy Smearing 114
9.4 Final Data and Simulation Comparison 115
9.5 Summary 120

10. Conclusions 121

REFERENCES 123

APPENDIX A. DETECTOR RESPONSE AS A FUNCTION OF INTERACTION POSITION 131

A.1 Sample Descriptions and Detector Response 131
A.2 Determining the Detector Regions with Full Phonon Energy Measurement 135

APPENDIX B. DETECTOR RESPONSE OBSERVABLE 138

B.1 Asymmetry in XY Plane 138
B.2 Asymmetry in Z Direction 142
B.3 Conclusions 145

LIST OF FIGURES

FIGURE Page

1.1 A photo of the M33 galaxy superimposed with a plot of the orbital velocity of the stars in the galaxy as a function of the radial distance from the center, which shows evidence that there is a significant amount of dark matter in the galaxy. The observed orbital velocity of stars (yellow data points) is not consistent with the expected orbital velocity from the measured luminous mass distribution (yellow dashed line). The best fit prediction with a spherically symmetric halo is shown with the solid yellow line. This observation provides evidence that most of the mass in the galaxy, called dark matter, is non-luminous [1, 2]. 4

1.2 This figure illustrates how gravitational lensing works and shows an image of an Einstein ring, which provides evidence for dark matter. The left figure shows how a massive object bends space and causes the light coming from a distant galaxy to go around the massive object or a dense region. Gravitational lensing of light from one object directly behind another can cause the appearance of a ring-like image. The right figure shows a Horseshoe Einstein ring image captured by the Hubble telescope [3]. The angular width of the ring shows there is dark matter because if there were no dark matter the width would be smaller [3, 4]. 6

1.3 Two images showing different views of the aftermath of two colliding clusters of galaxies called the Bullet cluster (1E 0657-56) which provide evidence that dark matter exists and has a particle nature. The left figure shows an image of the galaxies behind the Bullet cluster where the amount of gravitational lensing of each allows us to measure the mass density of the Bullet cluster between us and them, shown with the green contour maps. The right image shows the same green contour map superimposed on an image of a heat map of x-ray interactions, showing where the atomic collisions are occurring. A comparison of the two plots reveals that most of the interactions between the two colliding galaxies happen in the yellow regions while most of the mass is in the center of the green curves and is not affected by the collision [5, 6]. 7

1.4 A pair of images of the measurements of the cosmic microwave background (CMB) from the Plank experiment [7], which provide evidence that dark matter has existed since the earliest moments after the big bang. The plot on the left shows a heat map of the temperature of the Universe from the CMB, after subtracting off the average and other known effects. The plot on the right shows the power spectrum of the angular difference between the locations where things are hotter and colder which is called the CMB power spectrum. The best fit of the data on the right (blue dots) to the standard model of cosmology (red curve) indicates that dark matter constituted 26% of the energy density of the Universe at recombination [7]. 9

1.5 A simplified Feynman diagram (left middle) that models dark matter interactions with normal matter surrounded by example figures of how those types of interactions might be observed in nature. Following the arrows, which indicate possible directions of time, suggests three different possible dark matter detection methods: 1) Direct Detection (right): In this method, the goal is to observe dark matter interactions with standard model particles using a detector. The SuperCDMS experiment is focused on this method [8]. 2) Indirect Detection (top): A pair of dark matter particles can interact with each other and produce standard model particles. Astronomical observations aim at discovering dark matter by identifying occurrences from this type of interaction in the dark matter halo [9]. 3) Production (bottom): A pair of standard model particles can interact with each other and produce dark matter. Collider experiments such as LHC aim at producing dark matter or other non-standard model particles that decay to dark matter in particle collisions [10]. 11

1.6 A drawing of the conceptual design for the SuperCDMS detectors and what happens when a dark matter particle interacts in it. Our detectors are built of semiconductor and superconducting materials. Incoming dark matter particles can interact with the single-crystal semiconductor and produce primary phonons and electron-hole pairs. Electrons travel along a diagonal trajectory because of the lattice structure of the crystal, while holes can propagate directly to the electrode. When a voltage bias is applied across the detector, electrons and holes get accelerated in opposite directions. As charged particles move through the crystal, they interact with the crystal and produce more phonons called Luke phonons. We can measure the energy of these phonons using superconducting sensors. 13

1.7 A diagram of the HVeV laser experiment configuration where a laser emitting 1.95 eV photons is placed above the detector. The detector is biased by 100 V to create many Luke phonons for every electron-hole pair produced by the photon. 16

1.8 Pictures of the HVeV laser calibration experiment that was operated in the NEXUS facility at Northwestern University. The left image shows the Adiabatic Demagnetization Refrigerator (ADR) and the data acquisition system. The right image shows the readout electronics, heat sinks, and detector box to be placed inside the fridge. 17

1.9 This figure shows the distribution of the collected phonon energy in the laser experiment where HVeV detector was bombarded with red photons. The spectrum shows distinct peaks which correspond to the number of photons that arrived simultaneously at the detector, each of which liberated an electron-hole pair that was fully amplified. The measurements with energy in between the peaks are caused by the existence of impurities in the crystal (discussed further in Chapters 2 and 5). 18

2.1 An illustration of the electron energy levels in various materials which helps us understand how the electrons move within them and how they are categorized. In different types of materials, the electrons can either be part of the material structure (valence band, shown in blue) or be free and able to propagate in the material (conduction band, shown in red). The bandgap is the energy required to send an electron from the valence band to the conduction band. The Fermi level is the maximum energy level that electrons can occupy at absolute zero temperature [11]. In conductors the energy levels overlap, so electrons in the valance band can easily move into the conduction band and travel freely. In insulators, significant additional energy is required for an electron to move from the valence band to the conduction band. Semiconductors have a small bandgap which means an incoming particle can deposit its energy in a semiconductor crystal and send an electron from the valence band to the conduction band. This phenomenon makes semiconductors an excellent target material for particle detection. 22

2.2 A drawing that shows the initial outcome of a single photon interaction with the detector crystal which is the creation of an electron-hole pair. In this case, the incoming particle has an energy above the bandgap energy, but below two times the electron-hole pair creation energy so only a single electron and hole are created. Note that we have shown the case where no primary phonons are created and all energy beyond what was needed to liberate the pair went into the kinetic energy of the charges. 24

2.3 This figure is the same as Figure 2.2 but shows a simplified and exaggerated model of what happens at later times as the electrons and holes propagate through a perfect crystal under a high voltage bias. The diagram shows three different ways an electron can travel, projected into two dimensions, as they move diagonally. The electrons travel in their minimum energy potential valleys (unless they are scattered into a different valley), while the holes can propagate directly in the opposite direction. As charges move through the electric field, they pick up energy which they can then import to the lattice and create Luke phonons. The superconducting sensor will collect all the phonons, and we can measure the collected phonon energy by reading the current of the superconducting sensor. 29

2.4 This figure shows the equal-energy surfaces for the conduction bands of silicon to explain the direction of propagation of electrons in the crystal shown in Figure 2.3. The ellipsoids are the direction of the minimum potential valleys [12]. Electrons will travel along these valleys depending on the direction of the electric potential unless they are scattered into a different valley [13]. Note that this figure is oriented at a 45 degree angle relative to that shown in Figure 2.3. 30

2.5 This drawing illustrates the charge trapping and impact ionization processes that are caused by the presence of defects/impurities in the crystal. There are three separate interactions, each shown with a star, and in all three cases, the interaction creates an electron and a hole, each of which is accelerated by the voltage. On the left, we see the case where both charges travel to the detector surfaces without any interaction with impurities/defects in the crystal. The end points are shown with a circle. In the middle, we see the case where one of the charges gets trapped in an impurity/defect so we do not get full amplification. This is called charge trapping. On the right, we see the case where one of the charges liberates an additional charge from an overcharged impurity region. This charge is accelerated, creating additional phonons. This is called impact ionization. Note that no attempt has been made to properly describe the propagation path other than to show that each charge can change direction multiple times as as it traverses the detector...................... 33

3.1 This drawing shows a simplified conceptual diagram of how a pair of superconductors can be placed on top of a semiconductor crystal to create a measuring device known as a quasiparticle-assisted electrothermal-feedback transition edge sensor (QET). The phonons generated from the interactions in the semiconductor crystal can hit the large superconductor breaking the Cooper pairs into quasiparticles. Because of the thermal contact between the two superconductors, the quasiparticles can travel to and raise the temperature of the second superconductor which works as a transition edge sensor (TES). The TES is kept at its critical temperature by a combination of a voltage bias as well as being in thermal contact with the semiconductor. As shown on the left of Figure 3.2, small changes in the temperature of a TES result in a big change in its resistance, which we can measure from the current [14]. We note that the coupling to the electronics that readout a current from the TES are not shown in the figure. 37

3.2 Two drawings that help us understand the functioning and output of a TES. The figure on the left shows the resistance as a function of temperature and the figure on the right shows the shape of the TES readout current as a function of time when there is an energy deposit. Since the TES is operated near its critical temperature (by applying a voltage bias), a small heat deposition in the TES causes a big change in the resistance which translates to a sudden drop in the current. For the effective operation of the TES, its temperature should quickly go back to the operating temperature so it can measure the next signal. This is achieved by placing the TES in thermal contact with the crystal so it can lose heat as part of its temperature regulation. This feedback mechanism is called electrothermal-feedback. Note that the TES current is flipped by convention. 39

3.3 This figure shows two schematics of the TES circuit components with differing levels of sophistication. The left figure shows the idealized circuit, and the right figure explicitly represents the noise sources (with circles) as well as more detail about how the various components are designed [15]. The TES resistance at the bias point is represented with R_{TES}. The current bias, I_b is provided by a voltage bias (V_b). The total inductance in the circuit is represented with L. The shunt resistor is represented with R_{sh} and $R_{sh} << R_{TES}$. The unwanted resistance from the inductor is called parasitic resistance and is represented by R_p. A more complete version of this diagram is found in Figure 4.4 41

4.1 This figure shows two images of the HVeV detector housing. The view from above is shown in the top photo, and the lateral view is shown in the bottom photo. The HVeV detector is in the center of the copper housing, surrounded by the black frame. A single TES channel veto detector is placed next to the HVeV detector to the right. When the detector is used in laser-calibration mode, the photons are fired from the laser such that they impinge on the top surface in the middle of the box. The phonons are collected by the QETs on the top surface of the detector[14]. 44

4.2 This figure shows images of the full QET mask with 1,044 QETs (top left) and a blowup with six QETs (top right) as well as drawings of the full QET pattern (bottom left) and a single QET (bottom right). As shown in the bottom left drawing, the detector has two channels: the inner channel (506 QETs) and the outer channel (538 QETs). The four squares on the left of the detector (near the border between the two channels) are the wire bonding contacts for the TES readouts. The bottom right drawing shows the design geometry of a single QET. The Al collection fins are shown in light blue, the Al/W quasiparticle traps are in dark blue, the W TES is in gray, and the vortex sinks are shown as white holes. Phonons are collected by the Al fins and produce quasiparticles. The Al/W quasiparticle traps have a lower gap than the Al. Thus, quasiparticles get trapped in that region and transfer their heat into the TES, which raises the temperature and causes a sudden jump in resistance and a current signal which is measured by a SQUID array. The vortex sinks are responsible for stopping the creation of magnetic vortices in the superconducting Al. [14] 46

4.3 This drawing shows a cross-section of the detector to illustrate how phonons are collected by the QETs that cover the top surface of the crystal. Following the general design in Figure 3.1, in our experiment QETs are made of superconducting Al pieces and tungsten (W) transition edge sensors (TES). The Al pieces are called Al phonon collection fins. The phonons generated from the interaction get absorbed by the Al, break Cooper pairs, and produce quasiparticles. These quasiparticles travel to the TES and transfer their heat to the TES, which is at the edge of superconductivity and turns the heat deposition into a measurable signal [14]. 47

4.4 This figure shows a schematic of the TES readout circuit for the HVeV detector. The portion of the circuit on the left was previously shown in Figure 3.3. The component of the SQUID chip is shown inside the dashed box in the middle. The top right of the figure represents the output current (I_{output}) which is sent to the DAQ, flux-locking amplifier, feedback resistor (R_{fb}) and feedback inductance (L_{fb}) [14]... 49

4.5 This figure shows an example TES pulse (left) and noise trace out of the data acquisition system (right). Note that a 2.7 ms region of time around the pulse peak is known as an event, which is shown with dashed lines. 50

4.6 This figure shows two of the inputs for our reconstruction algorithm. Since the noise and signal shape shown in Figure 4.5 are mostly determined by the TES and readout circuit we expect most events to have the same pulse shape. The pulse shape as a function of time, determined by averaging many events in the real data and normalizing it to have a peak value of 1.0, is shown on the left and the noise PSD as a function of frequency is shown on the right. As shown in the plots, the electronic noise in each time bin is correlated in time and is frequency-dependent. .. 51

4.7 This figure shows two simplified diagrams of trigger methods that could be used for identifying the presence of an interaction from the phonon energy measurement out of the DAQ. On the left is what comes directly out of the DAQ and could, in principle, be used for triggering by comparing the peak of the pulse to a threshold. The right, which we use, considers the amplitude output of the optimal filter for a series of time windows, each with the same event length, plotted as a function of time, which is better for triggering. Note that we have chosen to show only a small window of time around the pulse, and on the left we refer to that window of time as an event. Events with interactions within them are identified using the method on the right, when the amplitude of the pulse goes above a specified threshold. Also note that the y-axis units on the left are in ADC counts (the units of the DAQ pulses), and after applying the filter, the filtered pulse is in optimal filter output units (μA). 52

4.8 A flow chart of how an optimal filter measures the amplitude of an input pulse. The inputs of the optimal filter are the Measured Pulse (for example the left-hand side of Figure 4.5) which is compared to the expected Pulse Shape (called a template, and shown in the LHS of Figure 4.6) and the Noise Power Spectral Density (PSD, and shown in the RHS of 4.6). The filter itself uses the χ^2 method in Equation 4.1 to determine the best fit scaling of the template (both in time and amplitude), and reports the minimized χ^2 as a measure of goodness-of-fit. Diagram recreated from Ref. [16]. The output amplitude is both used in triggering and in an estimation of the energy. 53

5.1 This figure illustrates the last step of the calibration process for the HVeV laser experiment where the x-axis is the corrected A_{OF} in μA and the y-axis is the expected E_{Phonon} from Equation 2.6. The data points are drawn from the peaks in Figure 1.9, the black line shows the best fit using Equation 5.1 and the red straight line is there to illustrate the difference if we had assumed a linear fit [17, 18]. 58

5.2 This figure shows the calibrated phonon energy before (raw) and after the livetime and data quality selection criteria [18]. 61

5.3 A model of the expected probability density of the phonon energy (in the number of electron-hole pairs energy unit) for the detector response to a laser shooting photons at it. In this scenario, the model assumes that the detector has no defects/impurities (charge trapping, f_T, and impact ionization, f_I, are both set to zero), the number of fully amplified eh pairs at the same time follows a Poisson distribution with $\lambda = 1$, and the resolution of the energy measurement, σ, is 3% of the electron-hole pair energy. 63

5.4 The predictions for the same simplified model shown in Figure 5.3, except we have added the effects of only charge trapping (left) and only impact ionization (right). The charge trapping and impact ionization fractions, f_T and f_I, are defined as the fraction of the electron-hole pairs that go through those processes and the energy distribution of the resultant phonon energy is assumed to be flat between peaks. The figure on the left is for the case when $f_I = 0$ and we see that the number of expected events between each of the peaks changes as we change f_T. On the right, when $f_T = 0$ and we see that the number of expected events between peaks also changes. However, no value of f_T allows for the creation of events below the peak. For this reason, we will be able to estimate the value of each parameter separately. .. 64

5.5 This figure shows the probability density of the energies of the events as a function of the electron-hole pair energy for the HVeV laser data at 100 V and the laser model with nominal parameter values (after scaling). We note that the model has qualitative agreement with the data for the region halfway to the first peak and below the third electron-hole pair peak, but it diverges from the data for events above the third electron-hole pair peak. Also, the model does not take into account the effect of the trigger, and that is the reason behind the discrepancy between the model and the simulation at low energies (near zero). 65

6.1 This diagram shows the workflow of the real data taking (right) and simulation (left). In the real experiment, the data acquisition system reads out the TES current and writes the data into the standardized raw data format. After that the reconstruction processes the data as described in Section 4.3. The simulation uses the GEANT4 toolkit from CERN to simulate the particle interactions [19]. SourceSim is responsible for simulating the external particles that interact with the detector (e.g. photons from a laser or dark matter particles). DetectorSim consists of three packages, simulation of the semiconductor crystal (CrystalSim), the superconducting sensor (TESSim), and the data acquisition and noise (DAQSim and NoiseSim). The final output of DetectorSim is raw data which is processed through the same reconstruction algorithm as the real data. 68

7.1 This figure shows a scatter plot of the position of the photon interactions on the top surface of the detector for our laser simulation using SourceSim. The sample contains 1,000 electron recoil direct energy deposits, each with a single photon hitting the top surface with 1.95 eV of energy and a uniform distribution for R < 3 mm. The surface area of the detector chip is 5 mm× 5 mm and the blue square shows the boundary between the two channels. 75

7.2 The distribution of the photon interaction positions for the sample of events shown in Figure 7.1 as a function of the interaction location. Note that the number of photons drops as a function of the depth of penetration in the Z direction, and shows no events more than $\sim$ 0.05 mm from the top surface of the detector. 76

7.3 Two plots showing the distribution of E^{Ch1}_{Phonon} and E^{Ch2}_{Phonon} (left) and the relationship between them (right) for the sample of events shown in Figures 7.1 and 7.2. The figures show two groupings of energies for each channel. The high-energy peaks are all in the same events and are from the case the electron-hole pair gets full Luke amplification. The low-energy peaks are from the case where the electron-hole pair gets absorbed by the detector surfaces or recombines immediately. Note that most of the phonon energy is collected by Ch1 because the energy deposits near the center of the detector. On the other hand, there is almost the same amount of phonon energy collected in Ch2 because the phonons bounce many times before being collected. 77

7.4 Three plots showing the distributions of the sum of the collected phonon energy, E_{Phonon}, from the two channels for the same sample. The top plot shows the full range while the bottom plots are zoomed-in to the low-energy and the high-energy peaks. The results are consistent with the expectations of Equation 2.5 modulo some phonon energy loss and resolution effects of the detector. 79

7.5 This figure shows two versions of the detector response as a function of the Z position of the photon interaction for the sample of events shown in Figures 7.1-7.4. While $\sim 74\%$ of all events get full amplification, the top plot shows the Z distribution of the events (Z = 2.00 mm is the top of the detector), where the events that are fully amplified are shown in red and those which are not are shown in blue. The bottom plot shows the efficiency of getting full amplification as a function of the distance from the top surface, Z. Most of the electron-hole pairs that are created very close to the top surface of the detector get absorbed and have a small probability of getting full Luke amplification. 80

7.6 These plots show the simulated TES current (out of TESSim) for an example event as a function of time for Ch1 (top left), Ch2 (top right), and a zoomed-in version for both channels superimposed (bottom) for comparison. 81

7.7 These plots show the same pulses as shown in Figure 7.6, but after the pulse has been processed by the DAQ simulation (DAQSim) which is responsible for the digitization of the pulses and conversion to Analog to Digital Converter (ADC) units. The digitization effect of DAQSim is most visible around Time=10100 μs in the bottom plot. 82

7.8 These plots show the same pulses as shown in Figure 7.7 but include the noise simulation (NoiseSim) which is added to the pulse before digitization. 83

7.9 These plots show comparisons between an example fully simulated TES pulse and the real data template (scaled to the TES pulse) in linear (left) and log (right) scales. We note that there is good agreement for most of the pulse, but they diverge at the largest times. 83

7.10 This figure shows the E_{Phonon} distribution out of the crystal simulation for samples of events with single-photon interactions in three different configurations: 1) charge trapping only (top left), 2) impact ionization only (top right), and 3) both (bottom). As described in Section 2.5 trapping will only create events with energies between the zeroth and first electron-hole pair peaks because the charge gets trapped and loses some of the Luke amplification. Impact ionization will only create events with energies higher than the first electron-hole pair peak because, in this case, an extra charge will be liberated and will produce extra Luke amplification. The charge trapping mean free path (CT MFP) is set to 260 mm and the impact ionization mean free path (II MFP) is set to 2700 mm. Note that these values are chosen based on the results for a Poisson laser that we will introduce in the next chapter. 85

7.11 This figure shows the E_{Phonon} distribution for the same sample as the bottom plot in Figure 7.10 after TESSim, DAQSim and NoiseSim as well as running the data through the reconstruction software (CRP), and adding calibration. Note that the width of the peak is larger because of the effects of the electronic noise. Another important point worth mentioning is that the low-energy events are removed because of the trigger effect which is part of the reconstruction software. 86

8.1 An illustration of the detector phonon energy readout for two simplified cases when a single photon interacts with the detector (shown as the box) at the point indicated with a yellow star. The top left shows the case where the electron-hole pair created by the photon immediately gets absorbed or recombined which means E_{Phonon} = 1.95 eV (the energy of the incident photon). The top right shows the case where the electron-hole pair goes through the full Luke amplification, in which case the detector will readout 1.95 eV from the incident photon energy plus the 100 eV from the Luke amplification. The bottom plot shows the expected E_{Phonon} distribution for the case where 50% of the photons are fully-amplified. 88

8.2 The same simplified scenario as in Figure 8.1, but with two incident photons at the same time at the points indicated with yellow stars. The top left shows the case where both electron-hole pairs created by the photon get recombined immediately, in which case the detector will readout 3.9 eV which is the combined energy of the incident photons. The top right shows the case where only one electron-hole pair goes through the full Luke amplification, in which case the detector will read out 3.9 eV from the incident photons plus the 100 eV from the Luke amplification. The bottom left shows the case where both electron-hole pairs go through the full Luke amplification, in which case the detector will read out 3.9 eV from the incident photons plus 200 eV from the Luke amplification. The bottom right plot shows the expected E_{Phonon} distribution for the case where 50% of the photons are fully-amplified. 89

8.3 A set of plots showing the E_{Phonon} distribution directly out of the full crystal simulation, for a different number of incident photons, labeled with N, each of which has an $\sim$75% chance of getting full amplification. As N increases, the number of possible outcomes increases as expected. 91

8.4 This figure shows the E_{Phonon} distribution for a set of photons emitted with a laser for which the number of emitted photons follows a Poisson distribution with $\lambda = 1$ (Poisson laser) (top) and zoomed-in histograms for individual peaks (bottom). The large peaks in the top plot are caused by the variation in the number of electron-hole pairs that went through the full amplification, M. The small peaks in the bottom four plots are caused by the variation in the number of incident photons, N. . 92

8.5 This figure shows the E_{Phonon} distribution using the Poisson laser model after adding charge trapping and impact ionization to the simulation. The charge trapping mean free path (CT MFP) is set to 260 mm and the impact ionization mean free path (II MFP) is set to 2700 mm for reasons described in the next chapter. 94

8.6 This figure shows the same results as Figure 8.5 but for the case where we have added the TESSim, DAQSim, and NoiseSim portions of the simulation and run the data through the reconstruction software, and calibration procedures. Note that the low-energy events do not contribute because the events with energy less than the threshold are not identified as events by the trigger. We also see that noise contributes to the width of the peaks (resolution).. 95

8.7 This figure shows the effect of the trigger threshold on the data. The plot on the left shows the calibrated E_{Phonon} distribution out of the reconstruction software with a low and high trigger threshold requirement on A_{OF}. The ratio of the two distributions illustrates which events are removed by the trigger, and is known as an efficiency curve. The removal of all events below a threshold follows the typical trigger turn-on curve shape [20]. 96

8.8 The E_{Phonon} distribution from CrystalSim for different simulation configurations to determine the various contributions to the width of the first electron-hole pair peak. The distribution in red shows the results for a sample of events where only a single photon interacts with the detector ($N = 1$). The distribution in blue is when the number of photons hitting the detectors follows a Poisson distribution with $\lambda = 1$. The distribution in green has the same simulation configuration as blue except charge trapping and impact ionization effects are turned on in the simulations. This shows that having a Poisson laser and impurities both contribute to the width of the peaks. 98

8.9 This figure shows the same results as Figure 8.8 but after running the simulated data through the reconstruction algorithm and after calibration, both without noise (left) and with noise (right) which shows that adding noise widens the width of the peaks. 98

8.10 Zoomed-in versions of Figures 8.8 and 8.9 which shows the E_{Phonon} distributions for different stages and configurations of the simulation along with the mean and RMS for the 1st electron-hole pair peak. Note that RMS is calculated for the data between 95 eV and 110 eV, indicated with the vertical dashed lines. We can calculate the RMS due to different effects using the width of the peak in the different configurations.. 99

9.1 The number of events in the HVeV laser experiment as a function of reconstructed energy as well as indicators that show which regions are used to measure a number of our simulation parameters. These include the trigger threshold region to determine the OF amplitude minimum value for the processing, the CT and CT+II region used to determine the CT MFP and II MFP parameter values, the energy calibration regions used to determine the calibration constants, and the additional energy smearing needed. Also shown are arrows to indicate the maximum number of events in each peak to determine the number of photons to simulate in our laser model.. 103

9.2 A comparison between the measured phonon energy spectrum from the real data and the full simulation using the final parameter simulations except for the use of the Poisson laser model with $\lambda = 1$ and CT MFP which is 260 mm here. This plot shows that a Poisson laser, originally shown in Figure 8.6, does not describe the data well at energies higher than about 300 eV. 105

9.3 This figure contains the E_{Phonon} distributions for the ten different simulation samples, each with a value of the number of photons per laser pulse from $N = 1$ to $N = 10$. We simulate a custom laser by combining these samples and applying weights to them. We note that there are different numbers of events for each sample. 107

9.4 This figure shows the data along with the results of the combined simulation samples created with the ten samples shown in Figure 9.3 after applying weights and the final parameter values of Table 9.1 except for the additional energy smearing. It shows good agreement except for the RMS of the peaks as expected. 108

9.5 Three versions of the energy distribution below the second peak for the data (shown in the black curve) and the simulation with three different trigger thresholds for use in determining the trigger threshold. Note that the simulation is done with the Poisson laser distribution for simplicity, but the final values of the CT MFP and II MFP are used and additional energy smearing is applied to the simulation data (described in Section 9.3.5). Comparing the results by eye, we chose $A_{OF}^{min} =$ 48 ADC because it produces the best match between data and simulation turn-on curves. 109

9.6 This figure shows how we estimate the mean free path value for charge trapping. The black curve shows the E_{Phonon} distribution for the data and the red shows the simulation. Also indicated with the vertical blue, green and magenta lines are the regions used to determine those values which are given in Table 9.2. The II MFP is set to infinity (impact ionization is turned off) while we have simulated four different values of the CT MFP (100 mm, 200 mm, 265 mm, and 300 mm) to determine which best describes the data below the first peak. This quantitative comparison is shown in Figure 9.7 and the final CT MFP value is 265 mm. 111

9.7 The plot of the ratio of the number of events in the regions below and in the first peak as described in Table 9.2 as a function of charge trapping mean free path (CT MFP) for the custom laser and the data shown in Figure 9.6. The solid black line shows the R1/2 for real data. We get the best match between data and simulation for CT MFP = 265 mm. 112

9.8 A comparison between the E_{Phonon} distribution from the real data and the simulation with the final CT MFP and II parameters (top) and two plots showing that the values of the chosen CT MFP and II MFP reproduce the ratio of events in the data for the regions below and above the first peak (bottom). We take 265 mm and 2700 mm as the final CT MFP and II MFP values, respectively. The observed number of events between the higher energy peaks, as shown in Figure 9.12 gives us confidence that the simulation is working as expected. 112

9.9 This figure shows the distributions of A_{OF} and E_{Phonon} using the full custom laser model and the final values of all the parameters except the additional energy smearing. Calibration is done using the same functional form from Equation 5.1 and yields value of $a = 601$ and $b = 0.115$. The comparison to data shows good agreement except for the RMSs of the peaks. 113

9.10 A comparison between the RMS of the first six electron-hole peaks for the data and simulation with all but the additional energy smearing as shown on the right-hand side of Figure 9.9. We add the additional energy smearing to take into account the fact that the width of the peaks is systematically smaller in the simulation. 114

9.11 The difference in quadrature between the RMS values in Figure 9.10 along with a linear fit to the results. We take *Additional Energy Smearing* = $(0.0016 \cdot E_{phonon} + 2.36)$.......... 115

9.12 The final comparison between E_{Phonon} distribution from the real data and the full simulation with all the final parameter values, including additional energy smearing. We see a good match between the two by eye. 116

9.13 This figure shows three comparisons between the E_{Phonon} distribution from the HVeV laser data and the simulation after all tunings. The top left shows the spectrum and ten custom ranges. The bottom left shows the number of events in each region. The plot on the right shows the difference between the simulation and the data for each range. 117

9.14 This figure shows the fitting results for the first of the electron-hole peaks in Figure 9.12 to a Gaussian function for the data (left) and the simulation (right). The calculated fit parameters (Amplitude, Mean, and RMS) along with the corresponding uncertainties are noted in the plots. 118

9.15 The calculated fit parameters (Amplitude, Mean, and RMS) for the simulation and the data as a function of the number of electron-hole pairs from Figure 9.12. There is a good match between the simulation and the data for amplitude and mean. The differences are shown in Figure 9.16. 118

9.16 Differences between the calculated fit parameters (Amplitude, Mean, and RMS) for simulation and data as a function of the number of electron-hole pairs. 119

A.1 This figure shows the position of the photon interactions for a sample of 30 k events using the same simulation configuration as Table 7.1, but extended to cover the full detector surface but restricted in the Z location to be at 1.9 mm, 0.1 mm below the top surface, so we do not get surface recombination effects as shown in Figure 7.5... 132

A.2 The distribution of the position of the photon interactions for the sample of events shown in Figure A.1 as a function of interaction location. The events cover the full top surface of the detector and are positioned at Z = 1.9 mm. 133

A.3 The E_{Phonon} distribution from the sample of events shown in Figures A.1 and A.2, which shows that most, but not all, of the photon interactions produce full Luke amplification (end up in the first electron-hole pair peak). 134

A.4 These two plots show the relationship of E^{Ch2}_{Phonon} vs. E^{Ch1}_{Phonon} for the same sample of events. The left plot is the full data and the right plot is after removing all events with $E_{Phonon} < 101$ eV, where we have a partial energy measurement. 134

A.5 This figure shows the position of the photon interactions that do not undergo full Luke amplification. The plot on the left shows the XY position of the photon interactions on the top surface of the detector for the events that did not get the full Luke amplification ($E_{Phonon} < 101$ eV). The plot on the right shows the distribution of the distances from the nearest wall for those events. All the events with a partial energy measurement are within 0.6 mm off of a sidewall. We note that requiring events to be further than 0.6 mm from a sidewall (which we can do in simulation but not in the real data) provides an effective way to select only fully-measured events. This is also known as applying a fiducial cut.................................. 135

A.6 This figure shows the two heat plots of the collected phonon energy of E^{Ch1}_{Phonon} and E^{Ch2}_{Phonon} before applying the fiducial cut. This is interesting because we see that when the event occurs in the center of the detector the majority of the event is deposited in Ch1 and the fraction in Ch1 drops as we move away from the center. The regions close to the sidewalls show significant energy loss. 136

A.7 This figure shows the two heat plots of the collected phonon energy of E^{Ch1}_{Phonon} and E^{Ch2}_{Phonon} after applying the fiducial cut (note the compressed heat map color representation), which confirms that the fiducial cut effectively removes the events with a partial energy measurement, which occurs when the energy deposit is close to a detector wall. 137

B.1 This figure shows two scatter plots of the Asymmetry value (marked with colors) as a function of the position of the photon interaction in the XY plane before and after applying the fiducial cut for the sample described in Appendix A. As shown in the plots, the square-shaped detector geometry and the interaction's distance from the center of the detector (X = Y = 0) both have an impact on the value of Asymmetry. 139

B.2 Two plots showing the Asymmetry as a function of the distance of the particle interaction from the center of the detector (R) before and after applying the fiducial cut for the same sample as Figure A.1. The Ch1 and Ch2 separation is visible at $\sim 3\,\mathrm{mm}$. As shown in the plots, applying the fiducial cut removes the events that deposited energy near the sidewalls. Note that our detector has a square shape, which determines the shape of the Asymmetry as a function of R. 140

B.3 Nine plots showing the Asymmetry as a function of angle (theta) for different ranges of R. These plots show that Asymmetry does not depend on theta for R < 2 mm and the corner effects emerge at R > 2 mm. 141

B.4 A scatter plot of the position of the particle interaction in cylindrical coordinates and corresponding Asymmetry range marked with colors. This plot shows that for R < 2 mm the Asymmetry only depends on R, while for R > 2 mm the Asymmetry depends on both R and theta because of the corner effects. The black solid line shows the detector edges and the blue line shows the channel border. 141

B.5 The distribution of the positions of the particle interaction for a sample of events as a function of interaction location simulated for studying the Asymmetry dependence on Z. The simulation configuration is the same as Table 7.1 except that 3 k events are simulated and the particle interactions are confined to R < 0.1 mm and cover the full depth of the detector -2 mm < Z < 2 mm. 143

B.6 This figure shows E^{Ch1}_{Phonon} and E^{Ch2}_{Phonon} values as function of the particle interaction position in the Z direction for the sample in Figure B.5. It shows that phonon energy measurement does not depend on Z except for the cases where Z is close to 2 mm, which is the top surface of the detector (where the QETs are placed). Near the top surface, the collected phonon energy in Ch1 is slightly larger because some Luke phonons get absorbed by the QET before making it to Ch2. 143

B.7 This figure shows scatter plots (top) and profile plots (bottom) of the Asymmetry as a function R (left) and Z (right) for the sample of events in Figure B.5. As shown in the left plots, since all particle interaction are very close to the center of the detector in the XY plane, there is no dependence on R, which means we can isolate the effect of the position in the Z direction. As shown in the right plots, the Asymmetry has a Z dependence only for Z > 1 mm because in that case, more of the Luke phonons that originate close to the sensors are directly absorbed. 144

LIST OF TABLES

TABLE Page

4.1 Summary of the HVeV detector design values for the NF-C (Northwestern Fermilab version C) QET layout mask shown in Figure 4.3 [14]. 45

5.1 A summary of the livetime selection criteria applied to the raw data which includes cuts based on the detector temperature and the stability of the TES readout along with the tolerance and the purpose of each cut. The data is separated into intervals of a given length (specified in the notes column), and those periods which are out of tolerance are excluded from the analysis. More details about the variables as well as the tolerances selected are described in Ref. [18, 21]. 59

5.2 A summary of the event-by-event data quality selection criteria applied to the raw data which includes cuts based on the output of the optimal filter, the time delay (t_0) and the goodness of the fit (χ^2_{min}), as well as the veto detector. The tolerances for the cuts, and the methods to determine them are highlighted in the text and described in more detail in Ref. [18, 21]. 61

7.1 A summary of the simulation configuration values used to make the two samples of events used in this chapter. The versions of GEANT4, SuperSim, and G4CMP packages used were 4-10-06-patch-02 [MT], V08-13-00, and V07-12-03, respectively. 76

8.1 This table shows the measured RMS of the phonon energy distributions for the set of events with 95 eV < E_{Phonon} < 110 eV after adding each effect to the simulation for three different simulation configurations including (i) $N = 1$, where only a single photon interacts with the detector, (ii) $\lambda = 1$, where the number of photons hitting the detector at the same time follows a Poisson distribution and (iii) same sample except charge trapping and impact ionization are turned on in the simulations. Each is repeated with the addition running through the reconstruction, with and without noise. If we assume that the resolution due to each effect adds in quadrature, then we can calculate the contribution of each effect. The results are listed in Table 8.2. 100

8.2 This table shows the contribution from each effect to the resolution. The values are calculated by taking the quadrature difference for different effects in Table 8.1. Noise has the biggest contribution to the resolution. The next two biggest contributions are from CT/II and multiple photons, respectively. 101

9.1 This table shows a summary of all tunable parameters along with the final values to produce the simulated phonon energy distribution shown in Figure 9.12. Note that the functions used for energy calibration and additional energy smearing are $E_{Phonon} = a{\cdot}A_{OF}{\cdot}(1{+}b{\cdot}A_{OF})$, and *Additional Energy Smearing* = $(a{\cdot}E_{phonon}{+}b)$, respectively. 104

9.2 This table summarizes the regions and ratios used to determine the crystal impurity parameters. The ratios R1/2 and R3/2 are used to determine the final CT MFP and II MFP parameter values. 111

1. Introduction and Motivation

The history of science has been a constant iteration between building models that describe our understanding of nature to better and better degrees of accuracy, then incorporating new observations from powerful new experiments. These observations give us clues about how to improve the latest model or construct a new one. This is one of the reasons that new technologies are so exciting. Perhaps more exciting is finding unexplained phenomena and trying to explain them. They provide opportunities for making yet more discoveries and pushing our understanding of the Universe forward. The motivation for the work in this thesis is based on trying to understand one of these unexplained phenomena, which is the existence of a kind of matter that does not emit light and yet fills the Universe. This substance is called dark matter, and we come back to it as well as the new simulation program designed to understand the next-generation detectors for discovering its particle nature after presenting a quick description of the Universe.

Understanding the "stuff" that fills our Universe and how the components interact on small and large scales has been a goal of scientists for millennia. Our best description of the Universe today is summarized by two main mathematical frameworks. The first one is the standard model (SM) of particle physics, which describes the known fundamental particles and how they interact at small distances ($10^{-18}\mathrm{m}$). According to the standard model, there are two types of fundamental particles, the particles of matter and the particles that provide the forces between them. The standard model describes the small-range interactions between the particles with three fundamental forces: the weak nuclear force, the strong nuclear force, and the electromagnetic force [22]. The second mathematical framework is the standard model of cosmology, which represents the most comprehensive description of the Universe at large scales from the earliest moments in time after creation until today [23]. For large distances, the governing force is gravity (the attraction between the objects with mass) and the effects of all other forces are negligible [24].

Although these two frameworks successfully explain most of what we observe in the Universe with remarkable precision, there are a large number of astronomical observations that suggest a major change in at least one of them that has defied confirmation [1, 6]. The data point to a new type of particle that provides most of the mass in the Universe today and has been around since some of the earliest moments of the Universe [2, 5, 7, 25]. For reasons that will be described shortly, it has been given the name dark matter and finding confirmatory evidence of it in an experiment has eluded scientists for decades.

The theoretical and experimental communities have joined forces to propose new models of the particle nature of dark matter and ever more sensitive detectors to observe it [26]. Different dark matter detection methods for the most favored models include observing dark matter interactions with normal matter, producing it in collider experiments, and looking for the outcome of the two dark matter particles interacting in astronomical observations [8, 9, 10]. None of the experiments that would have discovered it if it had a large mass, have observed it so far [26].

Some of the next-generation experiments have focused on combined semiconductor and superconducting detectors as an avenue for identifying $\mathcal{O}(1\ \mathrm{eV})$ interactions from dark matter that is hypothesized to fill the Milky Way [27]. The Super Cryogenic Dark Matter Search (SuperCDMS) experiment uses these technologies to build multiple complementary detectors for its dark matter search [8].

The main goal of this thesis is to incorporate simulations to help in the building and optimizing of the SuperCDMS experiment, so it can potentially detect dark matter. In particular, this work focuses on the understanding of small high voltage detectors known as the HVeV detectors. These detectors have already been able to search uncharted regions [17, 28], but the ability to extend their sensitivity further is limited by the lack of a full understanding of how those devices respond to very low-energy interactions. The method of this thesis is to use the simulation of the HVeV detectors to enhance our understanding. To achieve this goal, we will compare sophisticated new modeling of the HVeV detectors with well-understood photon interactions from laser data to both understand the physics of the detectors, and validate and improve the simulation of the experiment and the devices. With well-vetted tools, we can use the simulation to obtain otherwise inaccessible information about the experiment, which can suggest new ways to improve the detectors and/or analyze the data we get from them.

In this chapter, we present an overview of the motivations and methods of dark matter searches in general and the goals of this thesis in particular. We also describe our detector technology, its use in the HVeV laser calibration experiment, and its results. In Section 1.1, we describe some of the most compelling evidence that indicates the existence of dark matter and its particle nature. In Section 1.2, we describe the best guesses of the dark matter properties. In Section 1.3, we give an overview of the dark matter detection methods. In Section 1.4, we describe the conceptual design for building ultra-sensitive dark matter detectors using a single-crystal semiconductor connected to superconducting sensors. In Section 1.5, we describe the advantages of detectors operated with a high voltage in general, and some small, early-version detectors known as HVeV detectors. In Section 1.6, we focus on describing the role of simulations in dark matter searches and detector studies. In Section 1.7, we present an overview of the HVeV laser experiment and its main results. Finally, we finish this chapter by summarizing the goals and the outline of the rest of this thesis in Section 1.8.

1.1 Evidence for Dark Matter and its Particle Nature

In this section, we describe some of the most compelling evidence for the existence of dark matter and its particle nature. The advancement of observational astronomy has enabled scientists to study the Universe at both galactic and cosmic sizes. In particular, it has been possible to use different methods based on gravity to determine the amount of mass that governs the motions of particles and large bodies through space. If only the particles of the standard model are assumed, there is no consistent way to explain the large amounts of mass, but the results are readily understood if most of the mass in the Universe is composed of large numbers of dark matter particles.

While numerous observations point to the existence of dark matter, here we will only focus on three: 1) the luminous mass in a galaxy and the motion of the stars around its center [1, 2], 2) gravitational lensing, Einstein rings, and the Bullet cluster [5, 6, 25], and 3) measurements of the cosmic microwave background [7].

1.1.1 Luminous Mass in a Galaxy and the Motion of the Stars Around its Center

Comparing the measured mass and location of the stars in the galaxy, and the measurement of the required mass to explain the motions of the stars, provides strong evidence for the existence of unseen mass in the galaxies [1, 2], as shown in Figure 1.1. We describe two methods for determining the mass of the M33 galaxy and discuss the results.

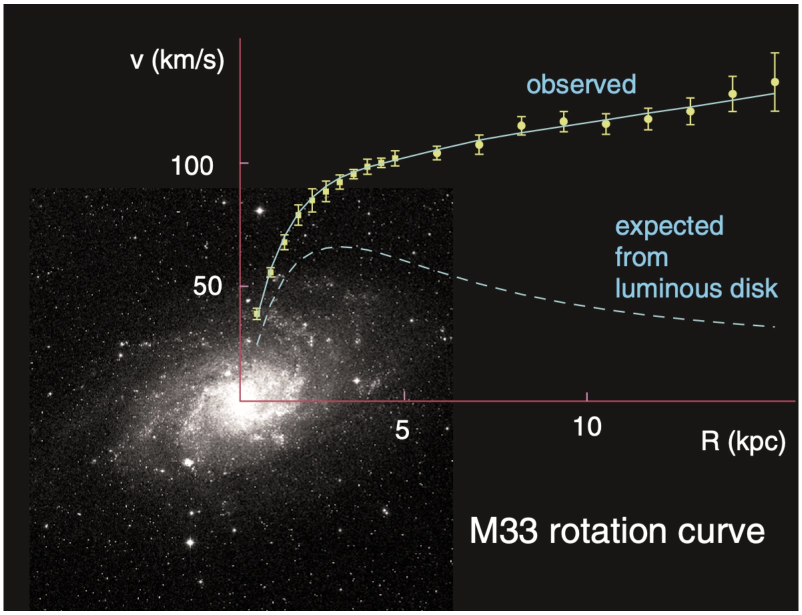

Figure 1.1: A photo of the M33 galaxy superimposed with a plot of the orbital velocity of the stars in the galaxy as a function of the radial distance from the center, which shows evidence that there is a significant amount of dark matter in the galaxy. The observed orbital velocity of stars (yellow data points) is not consistent with the expected orbital velocity from the measured luminous mass distribution (yellow dashed line). The best fit prediction with a spherically symmetric halo is shown with the solid yellow line. This observation provides evidence that most of the mass in the galaxy, called dark matter, is non-luminous [1, 2].

The first method uses the mass-luminosity relation, which is based on the observation that the amount of emitted light from a star is proportional to its mass [29]. This provides a first estimation of the total mass and its distribution [30]. Assuming that the mass of non-luminous objects in a galaxy is negligible compared to luminous objects, this provides a prediction for the speed of stars in the galaxy as a function of their distance from the center as shown in the figure.

The second method is deducting the effective mass distribution of the galaxy from its gravitational effects on the motions of the stars within it [31]. In particular, we can use the virial theorem to calculate the mass distribution based on the orbital velocity and the distance from the galaxy's center [32]. If we assume that galaxies are radially symmetric, the orbital velocity (v) of the objects in a galaxy depends on the amount of mass in the volume (M), the distance from the center (r), and the gravitational constant (G). Thus the mass of the objects in a galaxy can be estimated from the observed orbital velocity as a function of the distance from the center via:

$$v = \sqrt{\frac{GM(r)}{r}}. \tag{1.1}$$

Comparing the estimated mass of the M33 galaxy using these two methods provides strong evidence for the presence of a large amount of mass that is non-luminous. Figure 1.1 shows the observed orbital velocity as a function of the distance from the center for the M33 galaxy as well as the expected curve based on the mass-luminosity relation. As shown in the figure, the estimated mass from the mass-luminosity relation is much less than the predicted mass from the virial theorem [1, 2]. More detailed studies of the velocity distribution suggest that dark matter is the overwhelming majority of the mass and surrounds the visible matter in a sphere, known as a halo, just as it would do if it were essentially a gas of particles constrained by gravity [2].

1.1.2 Gravitational Lensing, Einstein Rings, and the Bullet Cluster

An independent measurement of the density of mass in a large region of space, based on general relativity, provides both evidence for dark matter and that it is a particle. We start by describing a technique to measure the amount of mass in a galaxy, or cluster of galaxies, from the bending of light that passes through or around it. We then show evidence for dark matter based on measurements done with this technique. Finally, we describe the observation from two colliding clusters of galaxies that provides strong evidence for the particle nature of dark matter.

We first explain how the path of the light that comes from a distant object can be used to determine the density of mass between the light source and us, and what it tells us about dark

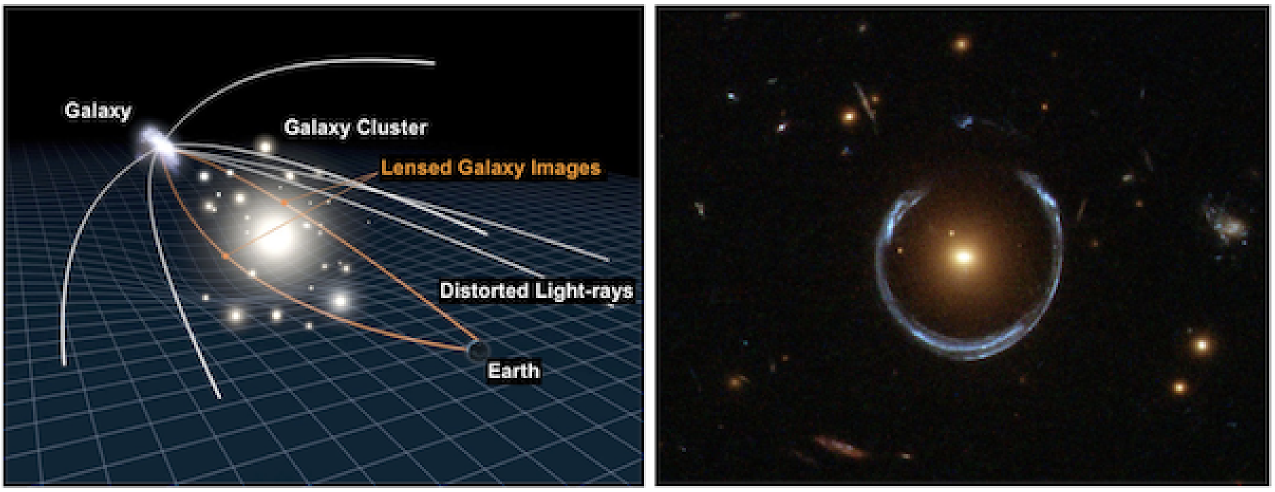

Figure 1.2: This figure illustrates how gravitational lensing works and shows an image of an Einstein ring, which provides evidence for dark matter. The left figure shows how a massive object bends space and causes the light coming from a distant galaxy to go around the massive object or a dense region. Gravitational lensing of light from one object directly behind another can cause the appearance of a ring-like image. The right figure shows a Horseshoe Einstein ring image captured by the Hubble telescope [3]. The angular width of the ring shows there is dark matter because if there were no dark matter the width would be smaller [3, 4].

matter. According to Einstein's theory of general relativity, massive objects bend the space through which objects travel, so consequently the path of some of the light is bent around them [25]. This phenomenon is called gravitational lensing and is illustrated on the left-hand side of Figure 1.2. A special case is when we have two galaxies, one directly behind the other relative to an observer. In this case, some of the light from the "far" galaxy is redirected (lensed) around the "near" galaxy towards the observer creating a circle of light around the object in the middle that provided the lensing. This is known as an Einstein ring [3] and an example of its observation in nature is shown on the right-hand side of Figure 1.2. The angular width of the ring allows for the measurement of the total mass of the near galaxy which can be compared to the estimate from the luminous matter from the amount of observed light from the center. The lensing observations are inconsistent with the predictions from the measurements of the luminous matter alone. However, they are consistent with other observations that suggest most of the mass in a galaxy is non-luminous [33].

Combining the images of the luminous and non-luminous regions of a colliding cluster of

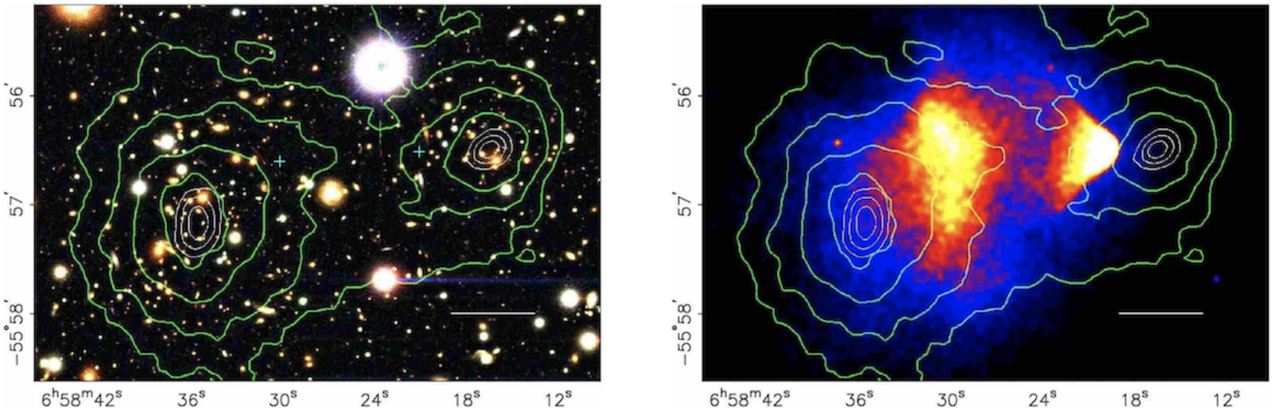

Figure 1.3: Two images showing different views of the aftermath of two colliding clusters of galaxies called the Bullet cluster (1E 0657-56) which provide evidence that dark matter exists and has a particle nature. The left figure shows an image of the galaxies behind the Bullet cluster where the amount of gravitational lensing of each allows us to measure the mass density of the Bullet cluster between us and them, shown with the green contour maps. The right image shows the same green contour map superimposed on an image of a heat map of x-ray interactions, showing where the atomic collisions are occurring. A comparison of the two plots reveals that most of the interactions between the two colliding galaxies happen in the yellow regions while most of the mass is in the center of the green curves and is not affected by the collision [5, 6].

galaxies, known as the Bullet cluster, provides an excellent opportunity for learning more about the nature of dark matter [5]. Figure 1.3 shows two images of the Bullet cluster overlaid with the gravitational lensing map. The figure on the left shows an image of the galaxies used to map out the density of the mass of the aftermath of the collision, which is shown with the green contour. The figure on the right shows the heat map from an x-ray image displaying the region where the atomic interactions are occurring, which gives a measure of the density of the atomic matter after the collision. A comparison indicates that most of the interactions between the colliding galaxies happen in the yellow regions while most of the mass is concentrated in the center of the gravitational lensing map and is unaffected by the collision. The fact that the locations of the atomic matter and dark matter are so distinct after the collision suggests that the majority of the mass, or what is known as dark matter, does not interact with or produce light. It also shows that the bulk of the dark matter in the two clusters passed through each other essentially unaffected, further suggesting that dark matter is made of minimally interacting particles that do not emit light

[6].

1.1.3 Measurements of the Cosmic Microwave Background

The low-energy photons that fill the Universe, known as the cosmic microwave background, add independent data for our understanding of dark matter. Measurements of the energies are consistent with those of a blackbody with a specific temperature [34] and the distribution of the temperatures in different directions not only provides solid evidence that dark matter has existed for much of the lifetime of the Universe, but also enables us to estimate its relative abundance in the Universe using the standard model of cosmology [7]. To understand how the cosmic microwave background observations are used in measuring the dark matter abundance shortly after the big bang, we need to review the history of the Universe.

Our best understanding is that the Universe started with a big explosion known as the Big Bang [35]. Shortly after the bang, the Universe was composed of fundamental particles including quarks, electrons, photons, and other things. At about $\sim$ 360,000 years after the bang, the Universe became cool enough for atoms to stop getting broken apart by photons [36, 37]. This era in the history of the Universe is referred to as recombination. During recombination, as electrons and atom nuclei started binding, the amount of the free charges (atomic nuclei and free electrons) dropped and consequently, the remaining photons in the Universe stopped scattering and started streaming freely [38]. These photons can be observed as the cosmic microwave background today and since they were in thermal equilibrium we can measure their temperature after the expansion of the Universe. The temperature measurement in different directions allows for an understanding of the dynamics of the early Universe [7].

Prior to recombination dark matter, if it existed, would affect the distribution of temperatures because it would have coupled to radiation and normal matter via gravity. The gravity would have generated inward pressure while the radiation generated outward pressure. This would have caused oscillations in the density of the mass throughout the Universe. However, after recombination, as the photon decoupling happened, this density oscillation would stop and the density of matter and dark matter would stabilize. The regions with low-density and high-density mass prior to

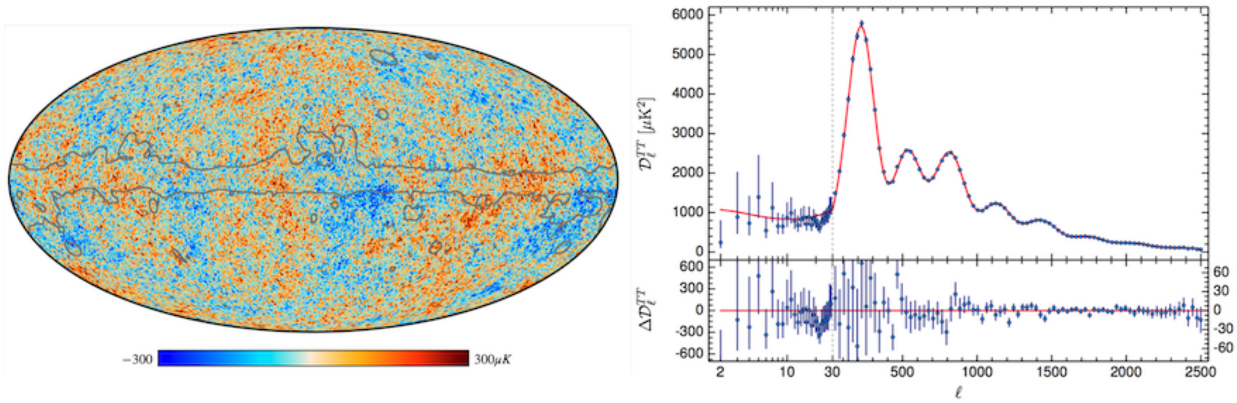

Figure 1.4: A pair of images of the measurements of the cosmic microwave background (CMB) from the Plank experiment [7], which provide evidence that dark matter has existed since the earliest moments after the big bang. The plot on the left shows a heat map of the temperature of the Universe from the CMB, after subtracting off the average and other known effects. The plot on the right shows the power spectrum of the angular difference between the locations where things are hotter and colder which is called the CMB power spectrum. The best fit of the data on the right (blue dots) to the standard model of cosmology (red curve) indicates that dark matter constituted 26% of the energy density of the Universe at recombination [7].

recombination would retain their temperatures in the photons which can be measured in the cosmic background radiation. This is why the relative abundance of dark matter can be calculated by studying the cosmic microwave background temperature map.

The left-hand side of Figure 1.4 shows the temperature map of the cosmic microwave background as measured by the Planck experiment after subtracting off the average and other known effects [7]. The angular distance between the temperature fluctuation can be translated to a power spectrum which is shown on the right-hand side of Figure 1.4. This spectrum provides a measure of the amount of pressure at the time of recombination which provides a measure of the relative abundance of dark matter at recombination. The best fit of the data to the standard model of cosmology is inconsistent with the absence of dark matter and estimates the relative abundance of dark matter, dark energy, and normal matter to be $\sim 26\%$, $\sim 69\%$, and $\sim 5\%$, respectively [7].

Although dark matter has not been discovered yet, there is overwhelming evidence it exists and that it moves through space like a particle would. In the next section, we summarize our best guesses about its properties, taking into account the above and other data.

1.2 Dark Matter Properties

After our description of the evidence that dark matter both exists and is a particle, in this section we summarize our best guesses about its properties. To summarize, dark matter is postulated to be neutral and minimally interacting, not made of protons and neutrons (non-baryonic), non-relativistic and stable:

- Dark matter is neutral and minimally interacting: If dark matter was charged, it would have produced light that can be seen or scattered light in a way that would have been noticed. Also if it interacted much, its path would have been slowed down significantly in the Bullet cluster interaction.

- Dark matter is non-baryonic: The evidence from the Bullet cluster observations and measurements from the cosmic microwave background suggests that if dark matter was baryonic (atomic in nature), its interactions should have been observed either in the x-ray image in Figure 1.3 or temperature map shown in Figure 1.4.

- Dark matter is non-relativistic: Studying both the large-scale structure of the Universe and the density distribution of the Milky Way suggests dark matter is non-relativistic which means it moves with a speed that is significantly slower than the speed of light [39].

- Dark matter is stable (or has a very long lifetime): Observations of evidence for dark matter both today (in galaxies) and in the early times in the Universe (in the cosmic background radiation from recombination) suggest that dark matter is either stable or has a very long lifetime [7].

1.3 Overview of the Dark Matter Detection Methods

Since there are many competing theoretical models to explain the nature of dark matter [26], scientists have come up with complementary experimental methods to see which, if any, are cor-

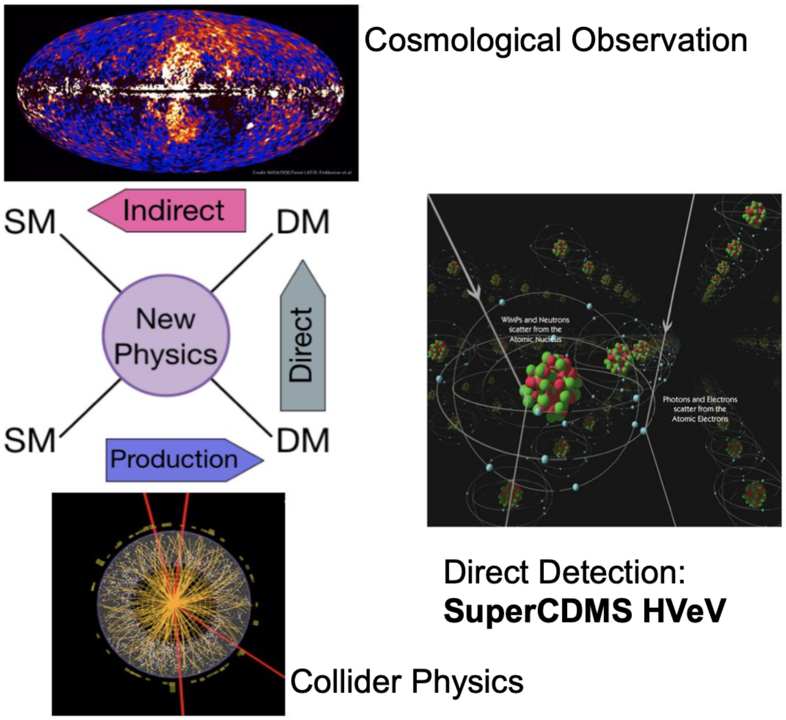
Cosmological Observation
SM
Indirect
DM
New Physics
Direct
SM
Production
DM
WIMPs and Neutrons scatter from the Atomic Nucleus
Photons and Electrons scatter from the Atomic Electrons
Direct Detection:
SuperCDMS HVeV
Collider Physics

Figure 1.5: A simplified Feynman diagram (left middle) that models dark matter interactions with normal matter surrounded by example figures of how those types of interactions might be observed in nature. Following the arrows, which indicate possible directions of time, suggests three different possible dark matter detection methods: 1) Direct Detection (right): In this method, the goal is to observe dark matter interactions with standard model particles using a detector. The SuperCDMS experiment is focused on this method [8]. 2) Indirect Detection (top): A pair of dark matter particles can interact with each other and produce standard model particles. Astronomical observations aim at discovering dark matter by identifying occurrences from this type of interaction in the dark matter halo [9]. 3) Production (bottom): A pair of standard model particles can interact with each other and produce dark matter. Collider experiments such as LHC aim at producing dark matter or other non-standard model particles that decay to dark matter in particle collisions [10].

rect. Figure 1.5 shows three different dark matter search methods predicated on the hope that they interact with normal matter:

- Direct Detection: Since the Milky Way is expected to be filled with dark matter, if one of those particles interacts with a nucleus or an electron in a detector here on Earth, we should be able to observe the recoil of the SM particle [27]. Our experiment, SuperCDMS, uses this detection method [8].

- Indirect Detection: Since dark matter must be neutral, there is a chance it is its own antiparticle. In that case, the possibility of dark matter self-annihilation exists. This provides an avenue for dark matter detection through its self-annihilation in the galactic halo center where the density is expected to be highest and it can produce normal matter that can be studied in astronomical observations [9]. Example experiments include the Alpha Magnetic Spectrometer (AMS-02) [40] and the Fermi Large Area Telescope (LAT) [41].

- Production: Another way of detecting dark matter is producing it, or other non-SM particles that decay to dark matter, in high-energy collisions of SM particles surrounded by a detector in a collider experiment [10]. Examples include the ATLAS [42] and CMS experiments [43] at the Large Hadron Collider (LHC).

1.4 Detector Concept: Making Dark Matter Detectors from a Single-Crystal Semiconductor and Superconducting Sensors

In this section we focus on our chosen direct measurement experiment, SuperCDMS, and describe how semiconductors and superconducting sensors can be used for building dark matter detectors for direct detection experiments in general. Since models of the dark matter in the Milky Way suggest that each particle has a small momentum, any recoil of an atom (or part of an atom) that might interact with it is likely to only receive a small amount of energy [26]. We start by describing the main requirements for effective direct dark matter detection. We then explain how semiconductors and superconducting sensors provide excellent methods for building a dark matter detector. Finally, we describe the conceptual design of the SuperCDMS detectors.

An effective dark matter detector should satisfy three main requirements. First, it should have a large target mass so there are a large number of particles that an incoming dark matter particle can interact with. Second, it should utilize an amplification scheme to make the impact of a dark matter interaction large enough that it can be measured by a sensor. Third, it should have minimal noise, so that evidence of an interaction can be readily identified within an electronic signal. One avenue in designing such ultra-sensitive detectors is building upon the existing semiconductor and superconducting technologies which have made immense advancements in recent decades [44, 45].

Semiconductor crystals are excellent target materials for dark matter detection for a number of reasons. Compared to other conventional detection targets like gaseous materials [46], the density of atoms in semiconductor crystals can be $\sim$ 1,000 times larger so the chances of capturing a dark matter interaction in a semiconductor can be large even with a small detector volume [47]. An additional benefit is that semiconductors have a specific band structure that can be used for amplifying the impact of an incoming particle with small energy (described in more detail in Chapter 2) [48]. Finally, superconducting sensors are very powerful in measuring small energy deposits with low noise from particle interactions in semiconductors.

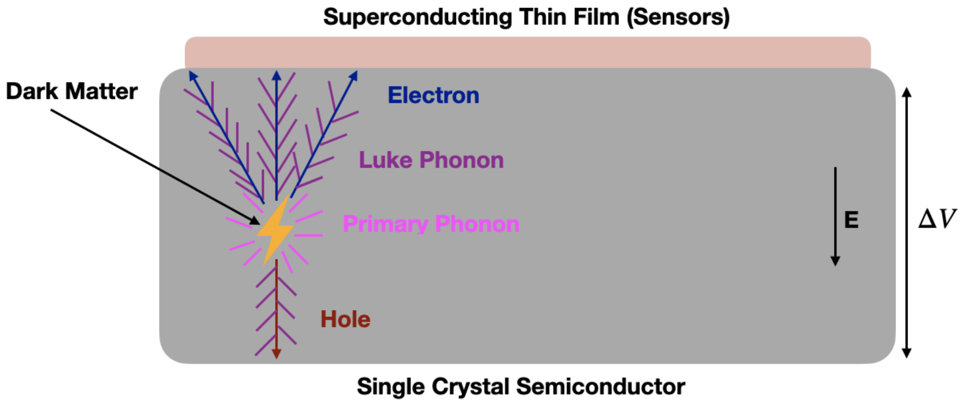
Superconducting Thin Film (Sensors)
Dark Matter
Electron
Luke Phonon
Primary Phonon
E
ΔV
Hole
Single Crystal Semiconductor

Figure 1.6: A drawing of the conceptual design for the SuperCDMS detectors and what happens when a dark matter particle interacts in it. Our detectors are built of semiconductor and superconducting materials. Incoming dark matter particles can interact with the single-crystal semiconductor and produce primary phonons and electron-hole pairs. Electrons travel along a diagonal trajectory because of the lattice structure of the crystal, while holes can propagate directly to the electrode. When a voltage bias is applied across the detector, electrons and holes get accelerated in opposite directions. As charged particles move through the crystal, they interact with the crystal and produce more phonons called Luke phonons. We can measure the energy of these phonons using superconducting sensors.

While we describe the details more in Chapters 2 and 3, we note that the SuperCDMS experiment uses a single-crystal semiconductor patterned with a thin-film superconducting sensor [8].

The conceptual design of our detectors is shown in Figure 1.6. An incoming dark matter particle can interact with the atoms in the crystal lattice of a semiconductor, and generate lattice vibrations (called primary phonons) and/or ionize an electron from an atom (and create what is known as a "hole" in the crystal lattice). The lattice vibrations, which propagate microscopically, impact other lattice sites and the energy propagates macroscopically through the lattice as a wave, like sound moving through air. By applying a voltage bias across the crystal, the electrons and holes traveling in the electric field will pick up more energy and interact with the lattice, creating enough additional phonons (called Luke phonons) to produce an observable signal [48]. This phenomenon is called Luke amplification and it has been used for many years to convert a small incident energy into a much larger phonon energy [48]. Not only can this signal be identified by the superconducting sensors on top of the crystal, known as a quasiparticle-assisted electrothermal-feedback transition edge sensors (QETs), measurements from these devices can be used to estimate the original recoil energy [14].

1.5 HVeV Detectors and Motivations

In this work, we focus on studying a new type of detector that operates with a large voltage and provides interaction energy measurements with a resolution of a few eV. For these reasons, the detectors are known as High Voltage electron Volt detectors, or HVeV detectors for short. There are two main motivations behind the HVeV program. First, to run the detectors as prototypes in preparation for the SuperCDMS SNOLAB [49] experiment, which is the next-generation of the SuperCDMS experiment. Second, to use them for searching for lower-mass dark matter.

Since the data to search for dark matter has been used to set some of the world's best limits for low-mass dark matter [17], our focus is on the portion of the HVeV program which serves as a prototype experiment in preparation for the SuperCDMS SNOLAB [49] experiment. It offers a great opportunity to enhance our understanding of the detectors and noise, practice the calibration of the detectors and ultimately identify technical issues that may arise and address them before commissioning of the main experiment. Compared to other detectors [8, 50], HVeV detectors are smaller and operate under a much higher voltage bias. As mentioned in Section 1.4, the amount of Luke phonons generated depends on the magnitude of the voltage bias. With a higher voltage bias, we can produce more Luke phonons and consequently get a bigger signal which means HVeV detectors can effectively probe for low-mass dark matter. Perhaps with a better understanding of the details of how the detectors respond to the small energy interactions the previous dark matter search data could be re-analyzed.

1.6 The need for Understanding the Physics of HVeV Detectors, Advantages of Using Simulations and the Goals of this Thesis

Using simulations to understand the fine detail of the physics of the experiment can play a significant role in enhancing our understating of the sensitivity of the HVeV detectors, as well as larger versions of them. While it is hard to quantify, a fully-validated simulation can be instrumental in suggesting ways to facilitate a discovery. If the models to describe their response are trustworthy, it allows us to use otherwise inaccessible information about the experiment to optimize the data analysis. For example, simulations allowed for unexpected improvements that led to the discoveries of the Higgs boson in 2012 [51] and the top quark in 1995 [52]. This suggests there is good reason to believe that simulation may play a crucial role in dark matter detection as well.

Since there has been very little use of sophisticated simulations in analyzing the SuperCDMS experiment, this thesis aims to validate the SuperCDMS simulation in the use of studying the interactions of photons with a known energy with the HVeV detectors. Dedicated runs of the experiment with a laser shining directly on the detector are useful for studying its response, especially for calibrating the energy measurements. Unlike dark matter interactions, photon interactions with the detector are well-understood so studying these interactions provides an excellent opportunity to enhance our understanding of the devices as well as validate the simulation for later use. We provide an overview of the HVeV laser calibration experiment in the next section.

1.7 Overview of the HVeV Laser Calibration Experiment

In this section, we present an overview of the HVeV laser calibration experiment. A central focus of this thesis is to reproduce the results of this experiment with simulations. We first introduce the goals of the HVeV laser experiment and its conceptual configuration, then we summarize the experimental setup, and finally discuss its results.

The goal of this experiment was to understand and calibrate the HVeV detector using red photons with a known energy. A diagram of the experiment is shown in Figure 1.7. The detector is a $10 \times 10 \times 4\ \mathrm{mm}^3$ silicon chip with 0.93 gr mass, is patterned with a superconducting sensor on the top surface [14], and is biased at 100 V. The superconducting sensor operates at cryogenic temperatures so the detector is cooled down to 50 mK. A laser source is placed on top of the HVeV detector and emits 1.95 eV red photons that visually cover the top surface of the detector with an R = 3 mm circle. Each photon is expected to ionize a single electron so the amount of phonon energy collected is expected to be quantized. On the other hand, impurities in the detector can cause mismeasurements.

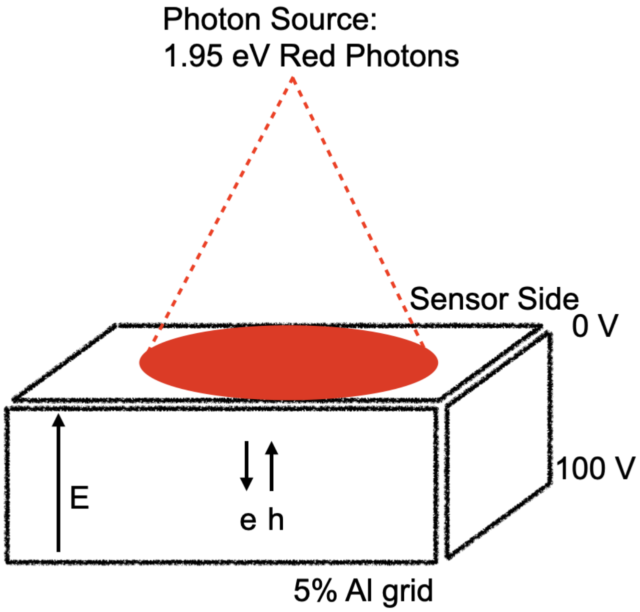

Figure 1.7: A diagram of the HVeV laser experiment configuration where a laser emitting 1.95 eV photons is placed above the detector. The detector is biased by 100 V to create many Luke phonons for every electron-hole pair produced by the photon.

This experiment took place at the NEXUS lab at Northwestern University, Evanston, Illinois in 2019 [17]. The left-hand side of Figure 1.8 shows an image of the NEXUS lab setup with the fridge and the data acquisition system. The right-hand side of the figure shows an image of the detector components that are placed inside the fridge. The readout electronics are outside of the detector box. The detector is placed inside a cooper housing that is inside a niobium can to shield it from background interactions and the magnetic field of the fridge [53].

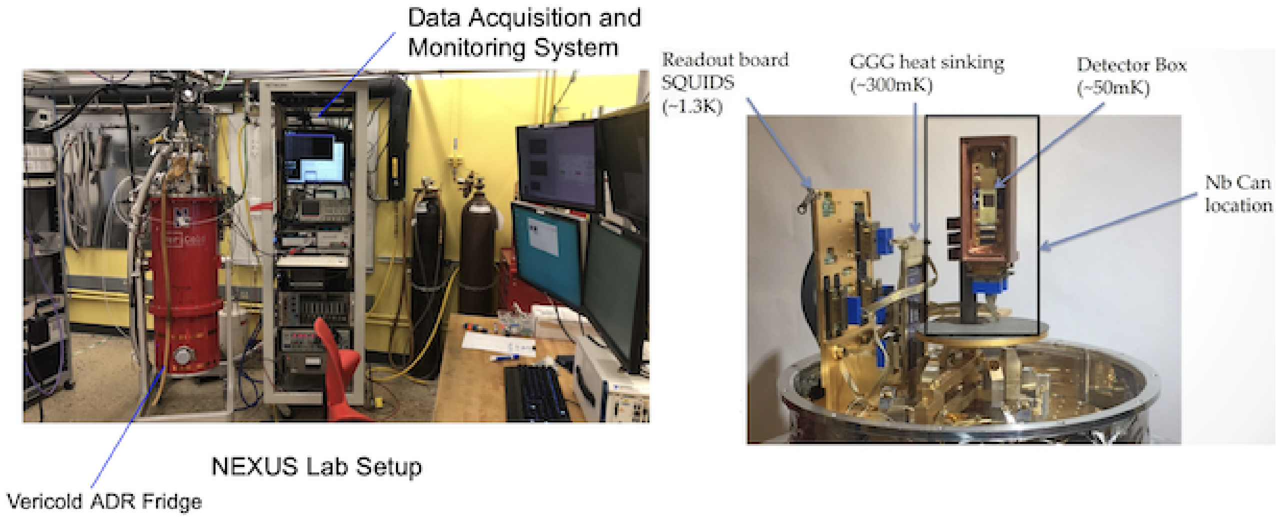
Data Acquisition and Monitoring System
Readout board SQUIDS (~1.3K)
GGG heat sinking (~300mK)
Detector Box (~50mK)
Nb Can location
NEXUS Lab Setup
Vericold ADR Fridge

Figure 1.8: Pictures of the HVeV laser calibration experiment that was operated in the NEXUS facility at Northwestern University. The left image shows the Adiabatic Demagnetization Refrigerator (ADR) and the data acquisition system. The right image shows the readout electronics, heat sinks, and detector box to be placed inside the fridge.

The main result of this experiment can be seen in Figure 1.9, which shows the distribution of the total collected phonon energy [17]. Since a red photon has enough energy for liberating only one electron-hole pair in the silicon, the detector will record a specific energy which includes the photon energy plus the additional energy from the Luke phonons. Similarly, if two photons from the laser reach the crystal at the same time, they can liberate two electron-hole pairs so we get double that energy. Three photons give three times, and so on. The peaks in the figure correspond to the number of electron-hole pairs that went through the full Luke amplification. On the other hand, because of the impurities in the crystal, we can periodically get more or less energy which

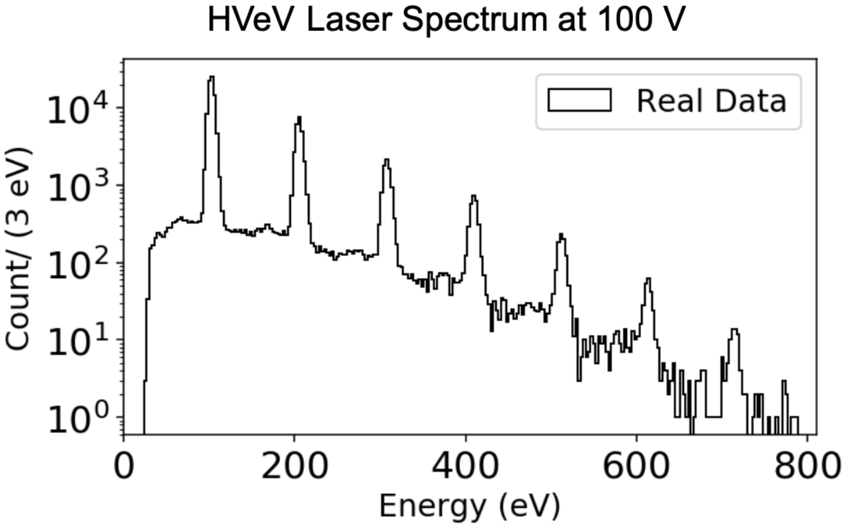

Figure 1.9: This figure shows the distribution of the collected phonon energy in the laser experiment where HVeV detector was bombarded with red photons. The spectrum shows distinct peaks which correspond to the number of photons that arrived simultaneously at the detector, each of which liberated an electron-hole pair that was fully amplified. The measurements with energy in between the peaks are caused by the existence of impurities in the crystal (discussed further in Chapters 2 and 5).

causes the background between the peaks. We will explain this in more detail in Chapters 2 and 5.

1.8 Overview and Outline of this Thesis

Understanding the nature of dark matter is one of the most critical unanswered questions in all of science and its discovery would have a big impact on particle physics, astronomy, and cosmology. Detectors built with semiconductor and superconducting technologies can provide an opportunity for discovering dark matter. Since it is likely to be unfruitful to just reanalyze the old data to look for evidence of dark matter, we focus on the HVeV laser data as it is well-suited for making advancements in our understanding of the detectors as part of a larger, long-term strategy. The goal of this thesis is to compare the simulation of the HVeV detectors with the well-understood photon interactions from the laser data to:

- Understand the physics of the detectors using simulation.

- Validate and improve the simulation.

- Use the simulation to obtain otherwise inaccessible information about the experiment which can suggest new ways to improve the detectors and/or analyze the data we get from them.

In Chapter 1, we gave an overview of the motivation behind dark matter searches, dark matter evidence, properties, and detection methods. We also introduced the SuperCDMS HVeV laser calibration program and explained the key role that simulations can play in making a discovery. In Chapters 2 and 3, we focus on the physics of the semiconductor crystal and the superconducting sensors. In Chapter 4, we provide more details about the design of the HVeV detectors and how we can calculate the incident particle energy from the energy readout of the sensors. In Chapter 5, we focus on the experimental setup of the HVeV laser calibration and use a simplified model to provide a qualitative understanding of the data. In Chapter 6, we switch gears to the simulation infrastructure and explain how different pieces of the simulation work. In Chapters 7 and 8, we present the simulation results for single-photon interactions as well as the case when multiple photons from the laser impinge on the detector at the same time. In Chapter 9, we compare the simulation results with the real data and tune the simulation parameters to get the best match between the simulation and the data. Finally, we conclude in Chapter 10.

2. Physics of Single-Crystal Semiconductors and Lattice Response to Photon Interactions

In the next two chapters, we discuss the physics of particle interactions in our detectors which consist of a single-crystal semiconductor and a superconducting sensor. In this chapter, we focus on the first stage, the interaction between a particle and the semiconductor crystal. In the next chapter, we focus on the second stage where the superconducting sensor produces a signal from the crystal response.

We start with an overview of the full process in a simple case. When an incoming particle, like a photon, hits the semiconductor in our experiment, it will ionize electrons from the lattice. Since there is a voltage across the semiconductor the electrons will be accelerated, interact with the lattice and cause vibrations, known as phonons, within it. Those phonons will eventually reach, and get absorbed by, the superconducting sensor which in turn produces an electronic signal that can be read out. Note that in this chapter, we will only highlight the most important outcomes of the particle interaction with the crystal. More details about the solid-state physics of particle detectors can be found in Ref. [54, 55].

Before getting to the interactions, we start this chapter by describing how electrons move in a crystal, with an emphasis on what are known as the conduction and valence band structures of semiconductors. This will help us explain why they are great target material for particle detection in Section 2.1. Then in Section 2.2, we discuss both electron and hole creation in a semiconductor crystal and the lattice vibration phonons when a particle, such as a dark matter particle or a photon, interacts with it. In Section 2.3, we discuss the consequences of applying a voltage bias to the crystal, which accelerates both types of charges and leads to the creation of additional phonons called Luke phonons. In Section 2.4, we describe more about the phonon and charge motion in the crystal. In Section 2.5, we explain the effect of impurities in the crystal, and we end this chapter with a summary in Section 2.6.

2.1 Conduction and Valence Band Structure

In this section, we discuss the properties that make semiconductors excellent target materials for particle detection. We start from the microscopic understanding of how electrons are attached to atoms within a solid, in our case a crystal, and move to a macroscopic understanding of how they move within a crystal as shown in Figure 2.1. In particular, we focus on the motion of charges through the crystal using the concepts of the valence band, the conduction band, the bandgap energy and electron-hole pair creation, which we will soon describe and define. We will also learn that the electrical conductivity of the different types of materials depends on the configuration of the valence and conduction bands. Finally, we demonstrate how we can utilize the intrinsic properties of semiconductors for our dark matter search.

How electrons move in a material, known as their electrical conductivity, is determined by how the electrons are attached to their atoms, and how much energy is required to liberate them when they are in a lattice structure as shown in Figure 2.1. One can think of the electrons, macroscopically, as being in one of two states: essentially stationary (part of the atom) or able to move freely within a material. The electrons in each of these states can have a range of energies, known as a band, and the two different states as being the band structure. The two bands are known as the valence band and the conduction band, respectively.

The band structure helps us categorize materials and understand their properties. In crystals, the valence band specifies the energy range of the electrons that occupy the outermost orbital of an atom. These electrons are bound to the nuclei of the atom but can absorb specific ranges of energy, get liberated from the atom, and move to the conduction band where they can travel freely within the crystal. The energy needed to send an electron from the valence band to the conduction band is called the bandgap.

Figure 2.1 also shows the categorization of materials into three types based on the ease at which electrons can flow through them. When there is an overlap between the valence band and conduction band, electrons can move freely between the two, which leads to electrical conductivity; thus materials with such properties are called conductors and have a small resistance. In the case

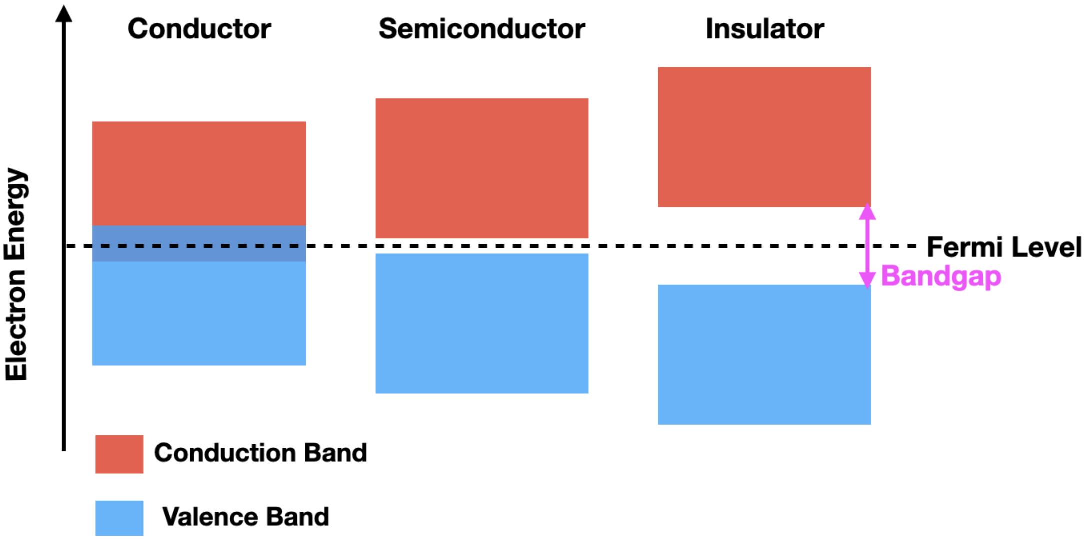

Figure 2.1: An illustration of the electron energy levels in various materials which helps us understand how the electrons move within them and how they are categorized. In different types of materials, the electrons can either be part of the material structure (valence band, shown in blue) or be free and able to propagate in the material (conduction band, shown in red). The bandgap is the energy required to send an electron from the valence band to the conduction band. The Fermi level is the maximum energy level that electrons can occupy at absolute zero temperature [11]. In conductors the energy levels overlap, so electrons in the valance band can easily move into the conduction band and travel freely. In insulators, significant additional energy is required for an electron to move from the valence band to the conduction band. Semiconductors have a small bandgap which means an incoming particle can deposit its energy in a semiconductor crystal and send an electron from the valence band to the conduction band. This phenomenon makes semiconductors an excellent target material for particle detection.

that a sizable energy is required to send an electron from the valence band to the conduction band (the bandgap is large), electricity does not flow easily, and these materials are known as insulators. On the other hand, semiconductors are in between and have a small bandgap energy (0.6 – 1.5 eV), so electrons can absorb a specific amount of energy and move from the valence band to the conduction band.

For a neutral semiconductor when an electron is ionized and moves from the valence band to the conduction band, the unoccupied valence state in an atom is called a hole and we call this process electron-hole pair creation. For the case where enough energy is deposited that multiple electrons can be liberated, the number is determined by what we call the average electron-hole pair creation energy.

2.1.1 Using Semiconductors for Particle Detection

Neutral semiconductor crystals can be effectively used for particle detection when they are near absolute zero temperature. At this temperature, all the electrons are typically in the valance band [56]. When a particle interacts with the crystal, even one with an energy of a few eV, electrons can be liberated into the conduction band creating one or more electron-hole pairs. The energy needed for this depends on the bandgap, which is an intrinsic property of the semiconductor material.

Since we know how much energy is required to send an electron into the conduction band, we can deduce how many electrons will be liberated if we know the energy deposited in the interaction. Inversely, we can approximate the amount of energy of the interaction from the number of charges sent to the conduction band and collected from a device. It is worth mentioning that microscopically, a high-energy incoming particle interacts with many atoms, each liberating a single electron (or two) over a short distance. Macroscopically, we think of this as a single interaction that produces many electrons. In the next section, we will explain the physics of electron-hole pair creation and phonon creation in more detail.

2.2 Charge Creation and Lattice Vibration (Phonons) in Single Particle Interactions

In this section, we explain how an incoming particle interacts with the semiconductor crystal to liberate electron-hole pairs and produce lattice vibration phonons. Of particular interest is the number and energy of the charges and phonons that are generated. This includes the energy split for the case of our experiment, where photons hit our detector, which is made from a single-crystal of silicon.

When a particle interacts with a semiconductor crystal, it can deposit its energy in the crystal by liberating charges and creating lattice vibrations. For the case described in the previous section, where an incident particle directly interacts with the electrons in the lattice through ionization, creating one or more electron-hole pairs in the lattice, we will refer to that as an electron recoil interaction. In this case, most of the energy will go into creating electron-hole pairs and the re-

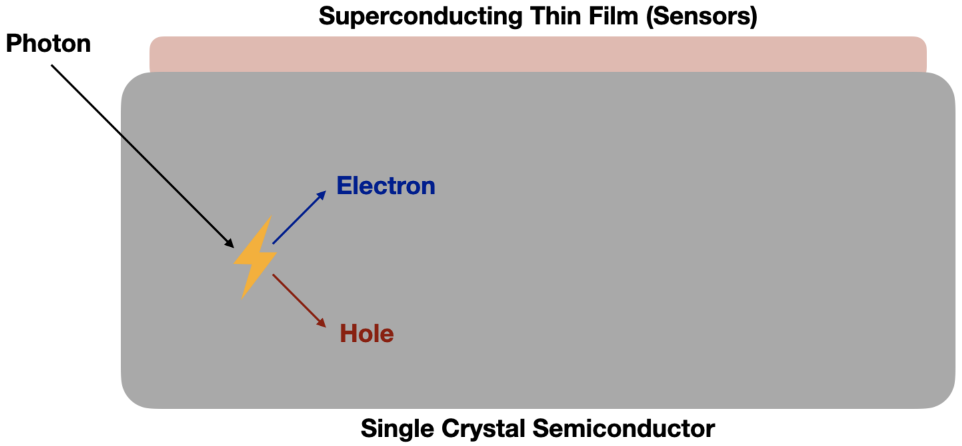
Superconducting Thin Film (Sensors)
Photon
Electron
Hole
Single Crystal Semiconductor

Figure 2.2: A drawing that shows the initial outcome of a single photon interaction with the detector crystal which is the creation of an electron-hole pair. In this case, the incoming particle has an energy above the bandgap energy, but below two times the electron-hole pair creation energy so only a single electron and hole are created. Note that we have shown the case where no primary phonons are created and all energy beyond what was needed to liberate the pair went into the kinetic energy of the charges.

maining energy goes directly into lattice vibrations, known as primary phonons, or into kinetic energy of the electrons, which can lose their energy as they interact with the lattice as phonons; for simplicity we can sometimes think of these as being primary phonons. Either way, it is just a matter of time before we are left with just the electron-hole pairs and some amount of phonon energy. When the incident particle interacts with a nucleus, referred to as a nuclear recoil, the situation is more complicated. Unless it is a very high energy interaction the location of the nucleus is constrained by the lattice structure so the energy effectively is converted into vibrations of the nucleus which creates primary phonons but can also ionize electrons, creating electron-hole pairs as it moves energetically in place. Quantitatively, in either case, when an incoming particle is fully absorbed, its energy (E_p) can be thought of as being converted into two forms of energy, the charge creation energy (E_Q) and the primary phonon energy ($E_{Ph,primary}$):

$$E_p = E_Q + E_{Ph,primary}. \tag{2.1}$$

The number of electron-hole pairs and the fraction of the energy that goes into primary phonons depends on the energy of the incident particle as well as its type. For an interaction between the incident particle and the electrons in the lattice, the number of electron-hole pairs created depends on the energy of the particle (E_p), the bandgap energy (E_{bg}), and the average electron-hole pair creation energy (ϵ_{eh}) of the semiconductor material. In the case that the particle has an energy less than the bandgap energy of the semiconductor, it cannot create any electron-hole pairs. Thus, all of the particle energy will be deposited in the crystal in the form of primary phonons. In the case that the particle has an energy higher than the bandgap energy of the semiconductor but lower than the average electron-hole pair creation energy, only one electron-hole pair will be generated, and the rest is typically shared between the motion of charges and a small amount of phonon energy. For energies above the average electron-hole pair creation energy, a decent approximation is that a total of $< n_{eh} >= E_p/\epsilon_{eh}$, electron-hole pairs will be liberated, and the remaining energy will go into the kinetic energy of the charges and primary phonons. To summarize, the number of electron-hole pairs can be calculated via:

$$< n_{eh} >= \begin{cases} 0 & E_p < E_{bg} \\ 1 & E_{bg} < E_p < \epsilon_{eh} \\ \lfloor E_p/\epsilon_{eh} \rfloor & E_p > \epsilon_{eh}, \end{cases} \tag{2.2}$$

where the "$\lfloor\ \rfloor$" symbol means rounding down to the nearest integer.

For simplicity, we will not do an accounting of the number of phonons at the moment but rather account for the total amount of energy deposited in the crystal by phonons, both at the interaction time as well as from charges that move through the lattice. While we have already mentioned primary phonons, we also get phonons when the electron and hole each recombine with the lattice structure with a phonon energy equal to E_Q. These phonons are called recombination phonons. We will come back to a full accounting when we finish describing the full set of effects. For the sake of completeness, we note that the number of primary phonons can be estimated via:

$$n_{Ph,primary} = \lfloor E_{Ph,primary}/E_{Debye} \rfloor + 1, \tag{2.3}$$

where E_{Debye} is the maximum allowed phonon energy based on the Debye model[57].

We can now turn our focus to the specific case for our experiment. Figure 2.2 shows what initially happens when a photon from the laser interacts with the crystal. As mentioned in Chapter 1, the semiconductor crystal is made of silicon, and the incoming particles are red photons with 1.95 eV energy. The bandgap and the average electron-hole pair creation energy of silicon are 1.12 eV and 3.6 eV, respectively [58]. Based on Equations 2.1 and 2.2, each photon that is fully absorbed can only create one electron-hole pair. The remaining energy goes into the kinetic energy of the charges and a few primary phonons. The fact that a red photon can at most liberate one electron-hole pair in the silicon crystal makes the laser a powerful tool for studying the HVeV detector response.

2.3 Effects of Applying a Voltage Bias to the Crystal: Luke Phonon Creation

In this section, we explain how applying a voltage bias across the detector crystal leads to the generation of additional phonons, which provides amplification of the detector signal so it provides a better measurement of the interaction energy. We start by showing how to determine the energy of these additional phonons in general, and conclude the section by calculating the energy of the additional phonons for the case of our experiment where the detector is bombarded by photons, and a 100 V bias is applied to the crystal. We explain the details of the motion of the electrons, holes, and phonons in the crystal in the next section.

When a voltage is applied across the crystal, any free charges (electrons and holes) pick up energy in the crystal because of the force applied to them by the electric field which, in turn, create additional lattice vibration phonons [59, 60]. These phonons are called Luke phonons to distinguish between them and the primary phonons which are created from the incident particle energy. Under a high voltage bias, a single particle interaction with the semiconductor lattice can instigate the creation of many phonons (thus amplifying the detector signal), which later can be measured by the superconducting sensor described in Chapter 3. This amplification process was first proposed by three scientists and is called Neganov-Trofimov-Luke gain (NTL or Luke gain) [48].

The total energy of the Luke phonons ($E_{Ph,NTL}$) depends on the number of electron-hole pairs (n_{eh}), the electric charge of an electron (e), and the voltage bias (V_{bias}) and it can be calculated via:

$$E_{Ph,NTL} = n_{eh} \cdot e \cdot V_{bias}. \tag{2.4}$$

Since the electron and hole will be re-absorbed by the lattice, that will also produce phonons of energy equal to the liberation energy. That phonon energy, combined with any primary phonon energy, or phonons produced from the kinetic energy of the electron and hole, will give us back the original interaction energy so the total phonon energy is given via:

$$E_{Phonon} = E_p + E_{Ph,NTL} = E_{ph,primary} + E_Q + n_{eh} \cdot e \cdot V_{bias}, \tag{2.5}$$

where E_{Phonon} is the total phonon energy [17].

Now we can discuss the case for our experiment where a 1.95 eV photon interacts with electrons in the crystal and creates one electron-hole pair. If we apply 100 V across the crystal, the electron-hole pair can generate 100 eV of Luke phonons. So, after all said is done, the total phonon energy is 101.95 eV. This is how the amplification mechanism allows for high-quality measurement of the low-energy particles with solid-state detectors. Going backward, for a voltage of 100 V if we observe 101.95 eV of phonon energy, we know the photon had 1.95 eV energy.

It is also worth noting that in our experiment multiple photons from the laser can interact with the detector at the same time, as shown in Figure 1.9. To a good degree of approximation they can all be considered independent and we can understand the peaks and their energies. While we will revise this later, for now we estimate the total phonon energy via:

$$E_{Phonon} \approx N \times 101.95 \text{ eV}, \tag{2.6}$$

where N is the number of incident photons.

2.4 Charge and Phonon Propagation in the Crystal

In this section, we go beyond the simple processes that describe how charges and phonons move to include lattice constraints, crystal impurities and other types of interactions. The details are important because, in the case of absorption by the detector surfaces or encountering an impurity region, the measured phonon energy will be affected. While the movement of the charges is affected by the electric potential from the voltage bias, they are also constrained by the crystal lattice. The charges can also get absorbed by the detector surfaces or impurity regions in the crystal or ionize an electron. The phonons, on the other hand, can decay, scatter off the impurities in the crystal, or get absorbed by the detector surfaces or other materials like the superconducting sensor. We first describe the particle propagation in this section and then return to the effects of impurities in the next section.

Figure 2.3 shows the different ways electrons and holes propagate in a perfect detector under a voltage bias. As shown in an exaggerated way in the figure, each electron will travel diagonally due to lattice constraints, and the holes, which aren't constrained to the lattice, travel directly to the bottom. The motion of the electrons can be understood using the solid-state physics of the crystal in Figure 2.4, which shows the equal energy surface for electrons in silicon [12]. Said differently, they provide the path of least resistance. It is worth noting that if they have enough energy, electrons can jump from one valley to the next and for this reason, create a narrower cone. Any phonons emitted by the charges are mostly emitted along the direction of the charge, with only a small opening angle between them as seen in the figure. It is equally important to note that a charge can also be absorbed by a sidewall if it gets close enough or hits it directly. More information about the interactions of charges with the sidewalls can be found in Appendices A and

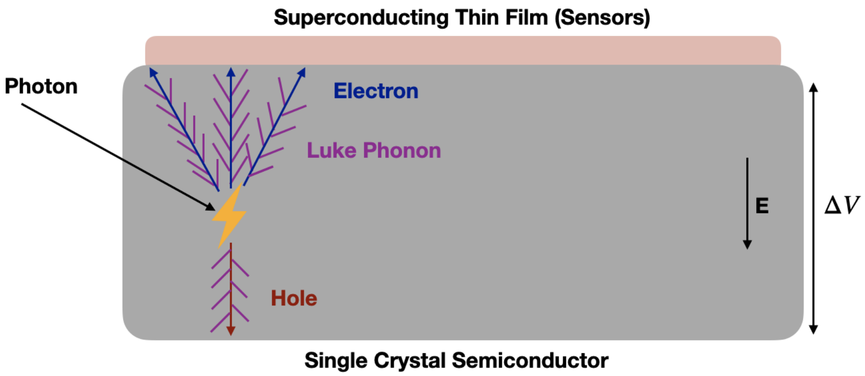
Superconducting Thin Film (Sensors)
Photon
Electron
Luke Phonon
E
ΔV
Hole
Single Crystal Semiconductor

Figure 2.3: This figure is the same as Figure 2.2 but shows a simplified and exaggerated model of what happens at later times as the electrons and holes propagate through a perfect crystal under a high voltage bias. The diagram shows three different ways an electron can travel, projected into two dimensions, as they move diagonally. The electrons travel in their minimum energy potential valleys (unless they are scattered into a different valley), while the holes can propagate directly in the opposite direction. As charges move through the electric field, they pick up energy which they can then import to the lattice and create Luke phonons. The superconducting sensor will collect all the phonons, and we can measure the collected phonon energy by reading the current of the superconducting sensor.

B.

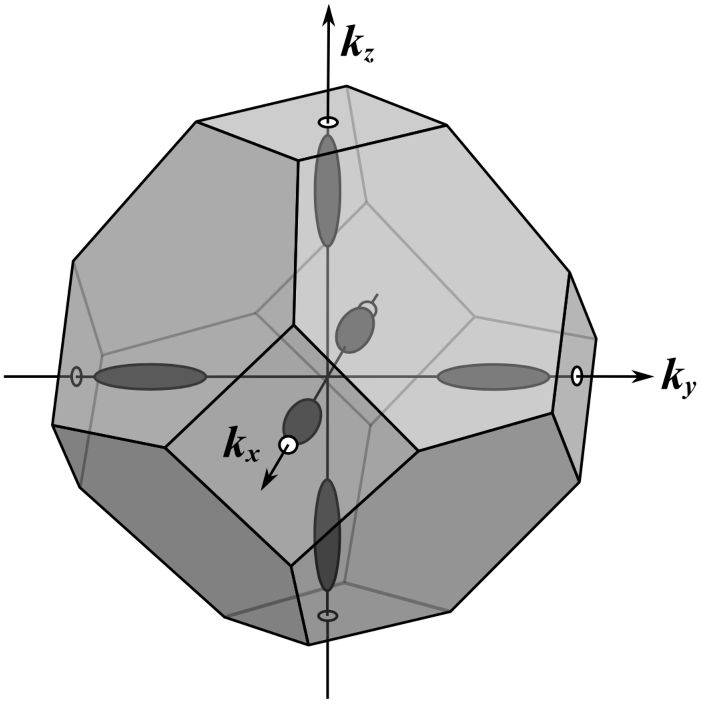

Figure 2.4: This figure shows the equal-energy surfaces for the conduction bands of silicon to explain the direction of propagation of electrons in the crystal shown in Figure 2.3. The ellipsoids are the direction of the minimum potential valleys [12]. Electrons will travel along these valleys depending on the direction of the electric potential unless they are scattered into a different valley [13]. Note that this figure is oriented at a 45 degree angle relative to that shown in Figure 2.3.

Next, we focus on the propagation of the phonons in the detector crystal and their interactions with the impurities and surfaces. Since only the energy of the phonons that are absorbed by a sensor is recorded, a full understanding of these processes is necessary for a proper energy measurement by the detector to take into account any energy lost. We start with an overview and then describe three mechanisms that affect the motion of phonons: (i) anharmonic decay, (ii) isotope scattering, and (iii) surface interaction (absorption and reflection).

The motion of the phonons within the crystal can be described by their energy and the direction of the oscillation with regard to their propagation direction, known as the phonon's mode [16]. How far a phonon travels before it converts to two lower energy phonons (called down-converting) is energy-dependent and described by its mean free path. High-energy phonons have a very small mean free path in the crystal and thus quickly down-covert. These phonons can also down-convert when they encounter impurity regions in the crystal. On the other hand, lower-energy phonons have a large mean free path, often larger than the size of our detector, so one can think of them as almost moving freely (sometimes called ballistically) [61]. In this case, their motion is unimpeded until they hit a boundary like a bare surface or a superconducting sensor. When a phonon hits a bare surface (sidewalls) it can lose some energy but most of the time elastically reflects back to the detector volume, while when a phonon hits the superconducting sensor, it can completely get absorbed or travel back into the crystal (sometimes after having interacted in the sensor). We note that phonons will bounce off the sidewalls many times and by the time they hit the superconducting sensor at the end, they are uniformly spread out through the crystal. This will be important when we get to Chapters 4 and 7.

We now say more about the three mechanisms that affect the motion of phonons:

- Anharmonic Decay: Phonons can spontaneously down-convert to two lower energy phonons through a mechanism called anharmonic decay [62]. This mechanism is important in particular because it determines the final number of phonons, and their energies. The rate at which phonons undergo anharmonic decay is energy-dependent with higher energy phonons being more likely to decay than lower energy phonons.

- Isotope Scattering: Phonons can also down-convert when they encounter crystal impurities through a mechanism called isotope scattering [63]. The probability of isotope scattering depends on the energy of the phonon and the density of the impurities. Higher energy phonons are more likely to go through isotope scattering [64].

- Surface Interactions: Phonons also interact with the detector surfaces. They can get absorbed by the sensors, called surface absorption, or reflect back to the crystal when they interact with either a bare surface or the sensor, called surface reflection. For well-polished surfaces, like those in our detector, the phonon energy typically stays the same after reflection (elastic collision). We note that after absorption by a sensor, processes in the sensor, can emit phonons back into the crystal at a later time.

It is worth noting that both anharmonic decay and isotope scattering change the mode of the phonons. Another important fact worth mentioning is that anharmonic decay is the most prevalent mechanism for higher energy phonons, while isotope scattering is the most prevalent mechanism for lower energy phonons [63].

2.5 Two Mechanisms that Effect the Total Collected Energy: Charge Trapping and Additional Charge Liberation (Impact Ionization)

In reality, the number of propagating charges in the crystal may not remain constant after the creation of the electron-hole pairs which, in turn, can affect the total phonon energy. This is because charge carriers can be absorbed by the crystal as they propagate, or ionize another electron or hole if they have enough energy, as shown in Figure 2.5. This happens in presence of defects/impurities in the crystal. Note that it is impossible to grow perfectly pure crystals, so defects/impurities are inevitable and their impacts on our measurements should be studied.

We consider two types of defects/impurities in the crystal: atoms with a number of electrons that makes them one-fewer-than-neutral, and atoms with a number of electrons that makes them one-more-than-neutral. In the case of one-fewer-than-neutral, a moving charge can get trapped in the unoccupied valence band, and in the case of one-more-than-neutral, a moving charge can easily excite the electron into the conduction band [65]. These effects are known as charge trapping and impact ionization, respectively [66].

Figure 2.5 shows an illustration of these two effects. It is worth noting that, in the case of charge trapping, we will not get the full Luke amplification, and the total phonon energy will be less than predicted in Equation 2.5. Similarly, in the case of impact ionization, we will have additional Luke phonons which will provide more than the predicted amount of energy.

2.6 Summary: Photon Interaction with the Single-Crystal Semiconductors Under Voltage Bias

With an understanding of how a particle interacting with a single-crystal semiconductor can produce a phonon signal, we move to the possible outcomes of a photon interaction from a laser

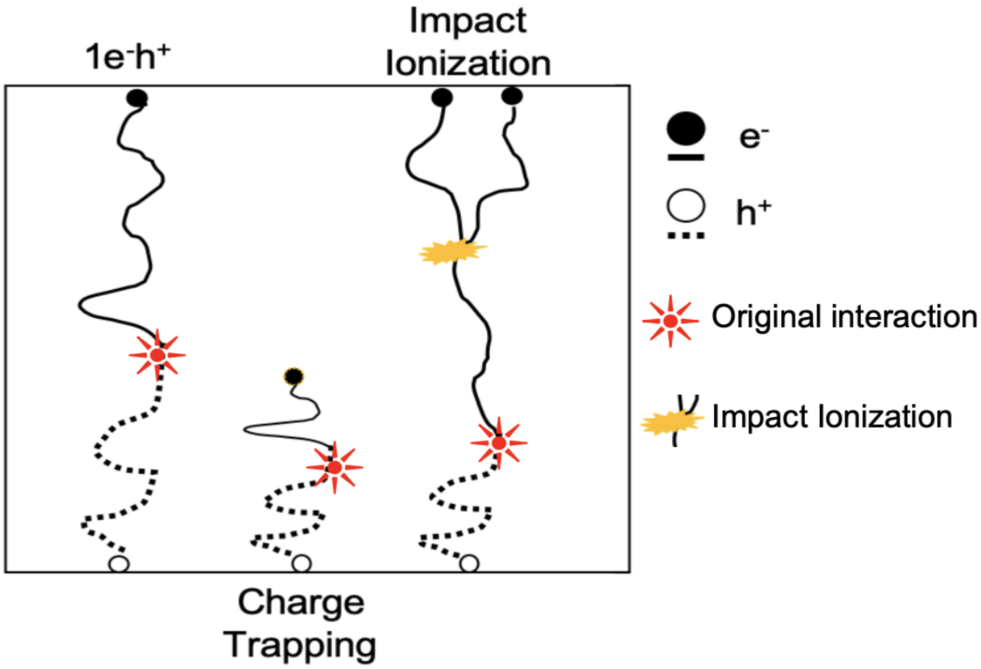

Figure 2.5: This drawing illustrates the charge trapping and impact ionization processes that are caused by the presence of defects/impurities in the crystal. There are three separate interactions, each shown with a star, and in all three cases, the interaction creates an electron and a hole, each of which is accelerated by the voltage. On the left, we see the case where both charges travel to the detector surfaces without any interaction with impurities/defects in the crystal. The end points are shown with a circle. In the middle, we see the case where one of the charges gets trapped in an impurity/defect so we do not get full amplification. This is called charge trapping. On the right, we see the case where one of the charges liberates an additional charge from an overcharged impurity region. This charge is accelerated, creating additional phonons. This is called impact ionization. Note that no attempt has been made to properly describe the propagation path other than to show that each charge can change direction multiple times as as it traverses the detector.

with the HVeV detector. As described in Chapter 1, the detector is bombarded with 1.95 eV red photons. The semiconductor is made of silicon which has a 1.12 eV bandgap and a 100 V voltage bias is applied to the crystal. Each photon can make one electron-hole pair because the energy of the photon is higher than the bandgap energy but less than the average electron-hole creation energy. The rest of the energy goes into primary photons or the kinetic energy of the charges which also quickly become phonons. Either way, the electron-hole pair can get recombined immediately to produce phonons or go through the Luke amplification. In the case that they don't immediately recombine, as each charge traverses the crystal it can go directly to the electrode or be trapped or ionize another charge. For the final phonon energy readout, there are four possible outcomes:

- The electron-hole pair gets recombined immediately or absorbed by a detector surface. In this case, the total phonon energy will be 1.95 eV.
- Regardless of the interaction position in the crystal, the combination of the path length for the electron and hole traverse the full voltage and thus produces a full amplification. In this case, we get 100 eV of Luke phonons plus 1.95 eV as described above. Consequently, the total phonon energy will be 101.95 eV. We note there are some caveats that apply here, as described in Appendices A and B, but they are not relevant for our experiment.
- The electron or hole (or both) will go through partial amplification before getting trapped in an impurity. In this case, the total phonon energy will be between 1.95 eV and 101.95 eV depending on where the charge trapping occurs.
- Either the electron or hole (or both) liberates another charge from an impurity, which produces additional amplification. In this case, the total phonon energy will be more than 101.95 eV.

3. Physics of Superconducting Sensors and Readout

With an understanding of how single-crystal semiconductors can be used to produce an amplified phonon signal from a small energy interaction, we turn to the physics of the superconducting sensor to record the signal. The superconducting sensor is responsible for converting the phonon energy into an electronic signal which can be used in later analysis. To summarize, the surface of our detectors is patterned with a large number of superconducting components made from two different materials. One is responsible for absorbing the phonon energies, and the other one is responsible for turning them into a measurable signal. Together they make a large number of small sensors which are combined for the full phonon energy measurements.

We start this chapter with a quick review of superconductivity in Section 3.1. We then introduce the smallest unit of our superconducting sensor known as a quasiparticle-assisted electrothermal-feedback transition edge sensor (QET) in Section 3.2. In Section 3.3, we discuss the dynamics of the transition edge sensor (TES) portion of the QET and how it completes the conversion of the phonon energy into an electronic signal, which can be used to measure the phonon energies. Finally, we describe the TES readout electronic circuit in Section 3.4.

3.1 Overview of Superconductivity

In this section, we present a quick review of superconductivity which plays a central role in the operation of our sensors. We also define some important concepts that we use later in this chapter including Cooper pairs, the superconducting bandgap, and quasiparticles.

The existence of free electrons in a conductor allows electric current to flow when a voltage is applied. At room temperature, electrons will bounce into other charges which impede their flow and consequently provide a small resistance. However, at very low temperatures, superconducting materials conduct electricity without any resistance. This happens because of the quantum mechanical effects which lead to the creation of coupled pairs of electrons, known as Cooper pairs [67]. At cryogenic temperatures, Cooper pairs can effectively move through the crystal in tandem with each other, essentially unimpeded and without any resistance.

A second point worth noting is that a Cooper pair can be broken apart with enough energy, for example from a phonon. The energy required is known as the superconducting bandgap energy and depends on the material properties of the superconductor. Since these electrons behave differently at low temperatures in the conductor, we refer to the electrons from a broken pair as quasiparticles [68]. Because these quasiparticles are merely charges, they continue to be a part of the current flow.

3.2 Quasiparticle-assisted Electrothermal-feedback Transition Edge Sensors (QETs)

In this section, we describe the conceptual design of QETs which are ultra-sensitive devices that are operated at cryogenic temperatures and measure the energy of the phonons [69, 70]. In particular, we discuss how QETs use a pair of superconductors to effectively collect the phonon energy and turn it into a measurable signal.

The QETs are made of a pair of coupled superconductors which can be thought of as each performing different tasks, as shown in Figure 3.1. The first one is designed such that it effectively collects the phonon energy, which breaks Cooper pairs producing quasiparticles. These quasiparticles often travel to the second superconductor, which responds to the quasiparticles in a way that generates an electronic signal. The pair is designed such that one can think of the heat from the phonons as being effectively transferred from the crystal to change the temperature of the TES with the assistance of quasiparticles.

The critical design feature of a QET is the different sizes and bandgaps of the two different superconductors. As shown in Figure 3.1, the phonons are collected by the first superconductor, which is significantly larger and has a large superconducting bandgap energy. The absorbed phonons break the Cooper pairs into quasiparticles. This can be thought of as heat, which effectively flows to the interface between the two superconductors. Where the two superconductors touch, the heat effectively raises the temperature of the second superconductor which both has a smaller volume and a smaller bandgap energy. The smaller superconductor is connected to electronics which can both regulate the temperature as well as provide a measurable signal by being a transition edge sensor (TES) [71]. This design is effective for our purposes because the material with the lower superconducting bandgap can be used in a much smaller volume, and consequently, we can avoid the buildup of excessive heat in the TES.

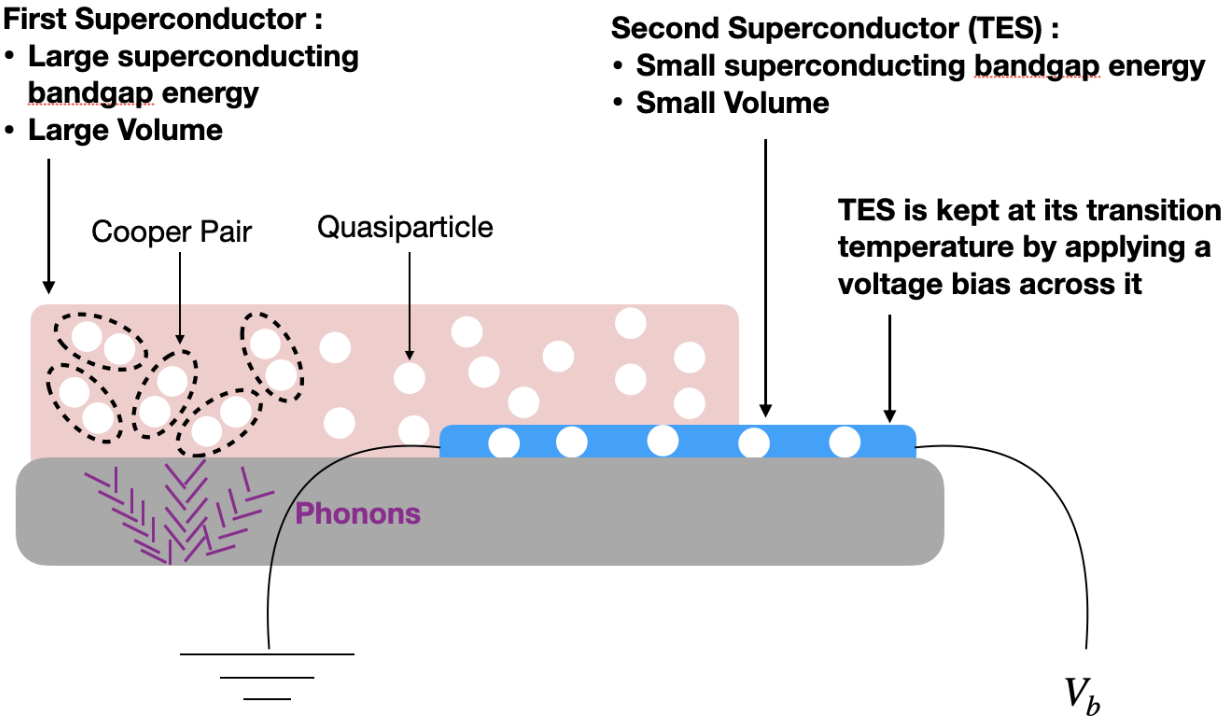
First Superconductor :
• Large superconducting bandgap energy
• Large Volume
Second Superconductor (TES) :
• Small superconducting bandgap energy
• Small Volume
Cooper Pair
Quasiparticle
TES is kept at its transition temperature by applying a voltage bias across it
Phonons
V_b

Figure 3.1: This drawing shows a simplified conceptual diagram of how a pair of superconductors can be placed on top of a semiconductor crystal to create a measuring device known as a quasiparticle-assisted electrothermal-feedback transition edge sensor (QET). The phonons generated from the interactions in the semiconductor crystal can hit the large superconductor breaking the Cooper pairs into quasiparticles. Because of the thermal contact between the two superconductors, the quasiparticles can travel to and raise the temperature of the second superconductor which works as a transition edge sensor (TES). The TES is kept at its critical temperature by a combination of a voltage bias as well as being in thermal contact with the semiconductor. As shown on the left of Figure 3.2, small changes in the temperature of a TES result in a big change in its resistance, which we can measure from the current [14]. We note that the coupling to the electronics that readout a current from the TES are not shown in the figure.

3.3 Transition Edge Sensor (TES)

In this section we focus on how a special property of superconductors, the big difference in resistance just above and below a critical temperature, makes them useful in particle detectors. We start with describing the big picture of how the smaller superconductor works as a TES which provides a measurement of the phonon energy and then show a nominal TES output pulse. We then explain the TES pulse shape which is determined by how we operate the TES. Finally, we show how to calculate the phonon energy from the TES pulse.

The TES is designed to measure very small energy deposits (heat) using the relationship between the resistance and temperature [69, 70], as shown in the left-hand side of Figure 3.2. By design the superconducting material in the TES is kept at the edge of the superconductivity, so its resistance has a sharp dependence on the temperature, which means a small amount of heat changes the resistance significantly [67]. When quasiparticles travel from the large superconductor to the TES (the small superconductor), they deposit their energy into it in the form of heat which increases the temperature by a small amount. The slight change in the temperature leads to a significant change in the resistance which instigates a sudden drop in the measurable current passing through the circuit. The right-hand side of Figure 3.2 shows the TES current as a function of time for an interaction that produced many phonons. Note that for consistency with the literature we have shown the TES pulse in an inverted way while in reality the current drops.

To understand the shape of the TES pulse as a function of time, and how we can measure the phonon energy from it, we need to explain the two sources of heat that change the temperature of the TES. By design, the TES needs to be kept at a temperature near its transition, and it also needs to be able to lose heat when it gains energy from the first superconductor. To do so, the TES is placed so that it is in thermal contact with the detector substrate so it can lose heat to it as shown in Figure 3.1. On the other hand, since the substrate is at a temperature lower than the critical temperature, a current flow must be provided to heat the TES so that it remains at its critical temperature, as also shown in Figure 3.1.

With all the sources of heat described, we can understand the pulse shape. When the heat

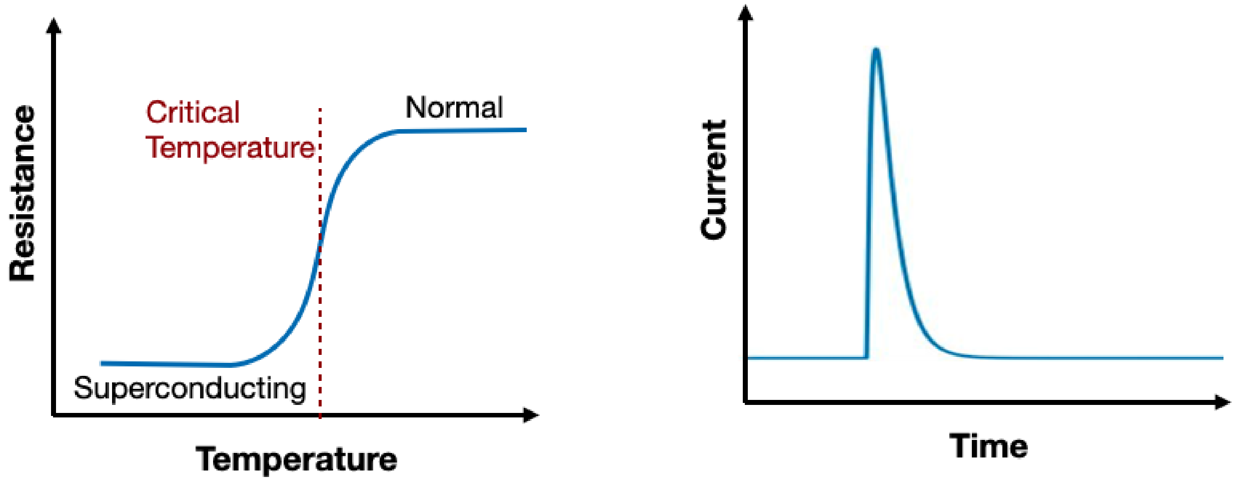

Figure 3.2: Two drawings that help us understand the functioning and output of a TES. The figure on the left shows the resistance as a function of temperature and the figure on the right shows the shape of the TES readout current as a function of time when there is an energy deposit. Since the TES is operated near its critical temperature (by applying a voltage bias), a small heat deposition in the TES causes a big change in the resistance which translates to a sudden drop in the current. For the effective operation of the TES, its temperature should quickly go back to the operating temperature so it can measure the next signal. This is achieved by placing the TES in thermal contact with the crystal so it can lose heat as part of its temperature regulation. This feedback mechanism is called electrothermal-feedback. Note that the TES current is flipped by convention.

deposition from the quasiparticles increases its temperature to above the critical temperature, we get a quick rise in the resistance which causes a quick drop in the current. After all the phonons have deposited their energy, this heat source stops. While the TES is always losing heat to the substrate, the additional temperature difference causes heat to flow more quickly, so the temperature of the TES quickly, but not quite as quickly, returns to its critical temperature and the amount of current flow rises over time giving us the shape on the right-hand side of Figure 3.2 (again shown in inversion) [70, 21].

The mechanism of both measuring the current flow and keeping the quiescent state of the TES at the critical temperature is called electrothermal-feedback [70]. To summarize, the total amount of heat loss to the detector substrate is equal to the amount of Joule heating provided by the circuit. To quantify this we note that the rate of power loss (P) depends on the thermal conductivity between the detector substrate and the TES (K), which is a function of both the critical temperature of the TES (T_c), and the temperature of the detector substrate (T_b) [20]. On the other hand, the rate of Joule heating is determined by the applied voltage bias (V_b) across the TES and its resistance (R_{TES}). In equation form, we can write both as:

$$P = K(T_c^5 - T_b^5) \tag{3.1}$$

$$P_{Joule} = V_b^2/R_{TES}. \tag{3.2}$$

For a perfect device, a measurement of the current as a function of time and knowledge of the resistance vs. temperature curve and the parameters of the circuit allows for an estimate of the total quasiparticle energy deposited [70]. Quantitatively, the total deposited energy (E_{Phonon}) is given by the change in Joule heating power (ΔP_{Joule}). For a nominal TES bias (V_b) and a measured change in current over time (ΔI), we find:

$$E_{Phonon} = \int \Delta P_{Joule} dt = V_b \int \Delta I dt. \tag{3.3}$$

Thus, by having a readout device that determines the amount of current at any time, and integrating it over the duration of the pulse, we have a direct estimate of the energy. We describe the readout circuit in the next section.

3.4 Phonon Energy Readout of the TES

With the discussion of how a QET can turn phonon energies into a measurable current in a TES in mind, we now turn to describe the TES readout circuit design that both allows for a current measurement as well as keeps the TES at the critical temperature. We describe the essential circuit elements, as shown in Figure 3.3, after we first discuss the three main requirements:

- The TES temperature needs to be kept close to its critical temperature via Joule heating.

- The current through the TES should not fluctuate by significant amounts. This is archived by adding a resistor in parallel to the TES, which is known as a shunt resistor, which has a resistance that is significantly smaller than the resistance of the TES [72].

- We need to employ an efficient measurement technique for measuring the current that goes through the TES. A typical solution is adding an inductor in series to the TES and then measuring the changes in the magnetic flux of the inductor, which directly depends on the TES current. This is done with an array of very sensitive magnetometers called superconducting quantum interference devices (SQUIDs), which can measure small changes in the magnetic flux [72].

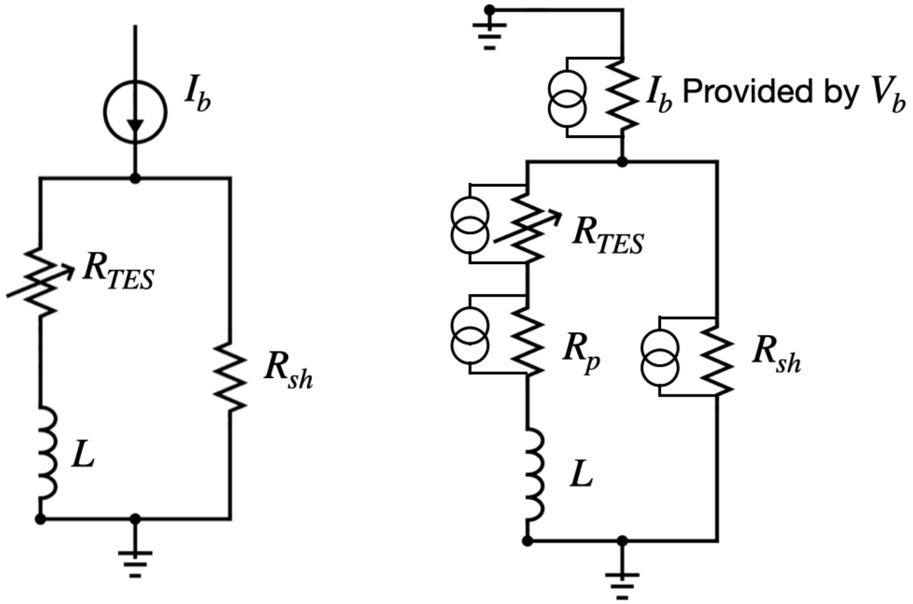

Figure 3.3: This figure shows two schematics of the TES circuit components with differing levels of sophistication. The left figure shows the idealized circuit, and the right figure explicitly represents the noise sources (with circles) as well as more detail about how the various components are designed [15]. The TES resistance at the bias point is represented with R_{TES}. The current bias, I_b is provided by a voltage bias (V_b). The total inductance in the circuit is represented with L. The shunt resistor is represented with R_{sh} and $R_{sh} << R_{TES}$. The unwanted resistance from the inductor is called parasitic resistance and is represented by R_p. A more complete version of this diagram is found in Figure 4.4

With these requirements and the solutions in mind, we can describe the TES readout circuit design in Figure 3.3 which shows the idealized circuit on the left and the more realistic circuit that better describes the noise in the system on the right. At the top, we see the circuit as being driven by a regulated current source on the left, and in more detail on the right. The TES can be thought of as a resistance which is in series with an inductor coil (L) and in parallel to a shunt resistor (R_{sh}), where ($R_{sh} << R_{TES}$). In reality, the current bias (I_b) is provided by a voltage bias (V_b), and the inductor generates some unwanted resistance, which is called the parasitic resistance (R_p).

When quasiparticles deposit their energy in the TES, the resistance of the TES increases sharply, and the current in the inductor coil drops. The changes in the current are measured indirectly by an array of SQUIDs (which are not shown in Figure 3.3 but included in the more complete diagram in Figure 4.4 later) that are in parallel to the inductor coil [72]. The measurement of the current happens very quickly, and the electrothermal-feedback kicks in almost immediately to return the temperature of the TES to its critical temperature. When the TES temperature is back to its critical temperature, the TES current is also back to the normal value and hence the TES is ready to measure new signals. More details about the design of the TES readout circuit used in the HVeV laser experiment are discussed in Chapter 4.

4. HVeV Detector and Readout Electronics Design

In this chapter, we describe the specific design of the detector used in the HVeV laser calibration experiment, the readout circuit, and the techniques used for the phonon energy measurement. To summarize, the HVeV detector is manufactured from a tiny silicon chip that is patterned with 1,044 QETs on the top surface as shown in Figure 4.1. The combined QETs are read out into two channels using the data acquisition system (DAQ) with custom readout electronics. The readout signal is processed through an energy reconstruction algorithm to provide the best estimate of the phonon energy.

When red photons bombard the top surface of the detector, they interact with the crystal semiconductor and effectively deposit their energy into the crystal by liberating electron-hole pairs. Since a high voltage bias is applied across the crystal, the charges are accelerated which in turn create more phonons while traveling through the crystal under the force of the electric field. The QET absorbs the phonons and re-directs their energy into the TES portion, which turns the heat into a measurable signal by the electronics. The signal is digitized and readout by the data acquisition system. Finally, we use a reconstruction algorithm to estimate the total collected phonon energy. While we present a quick overview of the detector design, readout circuit, and energy reconstruction, further detail can be found in Refs. [14, 71, 72].

We start this chapter by describing the detector design parameters in Section 4.1 and then describe the detector readout electronic circuit and accompanying noise in the system in Section 4.2. In Section 4.3, we explain how to reconstruct the total collected phonon energy from the TES current measurement. This includes two related concepts: windows of time in the readout that contain energy from an interaction, known as an event, and the identification of those times, known as the trigger. Both use an algorithm known as an optimal filter that makes use of the known signal shape from the TES as well as the expected noise from the electronics [73].

4.1 Detector Design Parameters

In this section we describe the HVeV detector design parameters. We start with the overall design of the detector and a description of how multiple QETs are arranged on the top surface of the detector. Next, we focus on the design of a single QET starting with an overview of the energy flow and the material choices, then describe the design in more detail. Finally, we discuss the material properties of the components of a QET. While we provide an overview in this section, Table 4.1 lists the HVeV design parameters, which are described in more detail in Refs. [14, 72].

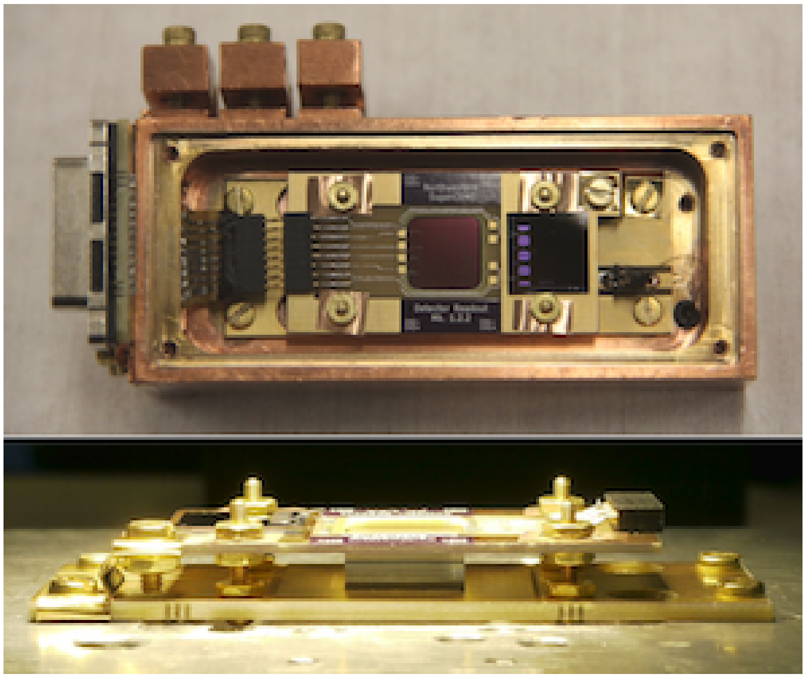

Figure 4.1: This figure shows two images of the HVeV detector housing. The view from above is shown in the top photo, and the lateral view is shown in the bottom photo. The HVeV detector is in the center of the copper housing, surrounded by the black frame. A single TES channel veto detector is placed next to the HVeV detector to the right. When the detector is used in laser-calibration mode, the photons are fired from the laser such that they impinge on the top surface in the middle of the box. The phonons are collected by the QETs on the top surface of the detector[14].

We begin by describing the overall design of the detector. Figure 4.1 shows the top and the lateral view of the copper detector housing. The HVeV detector is in the middle of the frame, and

Parameter	**Description**	**Value**
A_{det}	Detector Area	1 cm^2
η	Detector Thickness	4 mm
m_{det}	Detector Mass	0.93 g
N_{QET}	Number of QETs per Channel	$504/536$ (inner/outer)
l_{TES}	TES Length	$150\ \mu$m
l_{Al}	Aluminum Fin Length	$60\ \mu$m
T_b	Bath Temperature (Silicon)	50 mK
T_c	TES Critical Temperature	$\sim 65\ \mu$m
V_{bias}	Voltage Bias Across Detector	100V
R_{sh}	Shunt Resistance	~ 50 mΩ
R_b	Bias Resistance	8 kΩ

Table 4.1: Summary of the HVeV detector design values for the NF-C (Northwestern Fermilab version C) QET layout mask shown in Figure 4.3 [14].

the electronic wire connectors can be seen on the right of the detector chip. Also on the right is a single TES channel detector (black square) which identifies regions of time where there might be a coincident interaction by a cosmic ray. This is known as a veto detector. The top surface of the HVeV detector is patterned with an array of parallel QETs. The bottom surface is covered with an aluminum grid that is used for applying the voltage bias across the detector, while all other surfaces are always grounded.

The HVeV detector is made of a single crystal of $10 \times 10 \times 4 \text{ mm}^3$ of pure silicon that weighs 0.93 gr with a set of QETs placed on the top in a pattern known as a mask, as shown in the left-hand side of Figure 4.2. The QET mask consists of 1,044 individual QETs which have their results combined into two readout channels (inner and outer, or Ch1 and Ch2) with approximately equal coverage of the surface of the detector to provide a large enough signal to be measured. The inner channel has 506 QETs, while the outer channel has 538 QETs. Having two channels is advantageous because it gives us information about the interaction position of the initial particle (in our case, a photon) in the detector and helps us distinguish the poorly-measured interactions caused by an incident particle interaction near the detector edges. More on this issue is described in Appendices A and B.

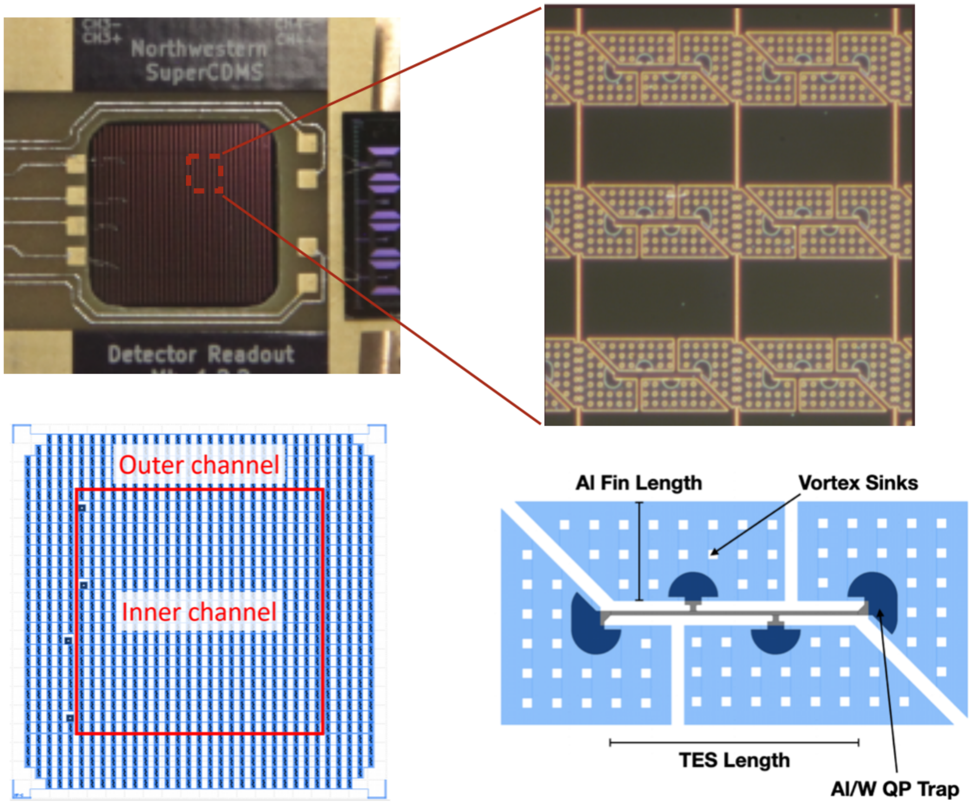

Figure 4.2: This figure shows images of the full QET mask with 1,044 QETs (top left) and a blowup with six QETs (top right) as well as drawings of the full QET pattern (bottom left) and a single QET (bottom right). As shown in the bottom left drawing, the detector has two channels: the inner channel (506 QETs) and the outer channel (538 QETs). The four squares on the left of the detector (near the border between the two channels) are the wire bonding contacts for the TES readouts. The bottom right drawing shows the design geometry of a single QET. The Al collection fins are shown in light blue, the Al/W quasiparticle traps are in dark blue, the W TES is in gray, and the vortex sinks are shown as white holes. Phonons are collected by the Al fins and produce quasiparticles. The Al/W quasiparticle traps have a lower gap than the Al. Thus, quasiparticles get trapped in that region and transfer their heat into the TES, which raises the temperature and causes a sudden jump in resistance and a current signal which is measured by a SQUID array. The vortex sinks are responsible for stopping the creation of magnetic vortices in the superconducting Al. [14]

In our experiment, each QET is made of superconducting aluminum (Al) pieces and a tungsten (W) transition edge sensor [14]. Figure 4.3 shows a cross-section of the detector, which includes the silicon crystal substrate and the QET on top of it. The Al piece, labeled as an Al Fin, is responsible for collecting the phonons from the semiconductor crystal and converting them to quasiparticles. The tungsten transition edge sensor, labeled as W TES, and its readout circuit (not shown here) provide the final stage of converting phonon energy into a measurable signal.

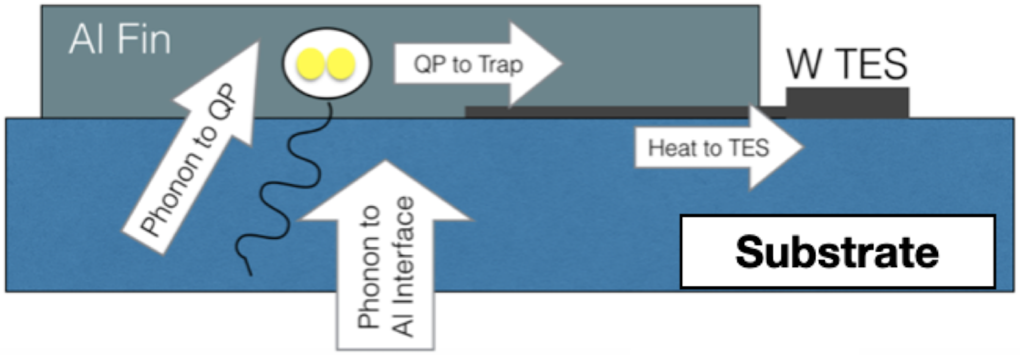

Figure 4.3: This drawing shows a cross-section of the detector to illustrate how phonons are collected by the QETs that cover the top surface of the crystal. Following the general design in Figure 3.1, in our experiment QETs are made of superconducting Al pieces and tungsten (W) transition edge sensors (TES). The Al pieces are called Al phonon collection fins. The phonons generated from the interaction get absorbed by the Al, break Cooper pairs, and produce quasiparticles. These quasiparticles travel to the TES and transfer their heat to the TES, which is at the edge of superconductivity and turns the heat deposition into a measurable signal [14].

.

An image of six QETs and a drawing with more detail about the design of a single QET are shown on the right-hand side of Figure 4.2. A single QET is made of four large Al collection fins, four Al/W trapping regions, and a long thin W TES shown in gray. A set of square-shaped holes, called vortex sinks, are carved in the Al to prevent magnetic vortices from forming in the superconductor [21].

With the design of the QETs in mind, we can review the material properties of Al and W to gain a better understanding of our QETs design. The critical temperatures of Al and W are 1.2 K and 65 mK , respectively. At the detector operating temperature (50 - 52 mK), the Al is superconducting and consequently has Cooper pairs while the W is heated via a voltage bias to keep its temperature at the edge of superconductivity, as shown in Figure 3.2 [14]. One of the primary advantages of the Al is that its superconducting gap energy is $\sim 350\ \mu\mathrm{eV}$. This means that only primary and

Luke phonons contribute to the phonon energy measurement because thermal phonons (intrinsic vibration of the crystal) only have $\sim 1\ \mu\mathrm{eV}$ energy, which is not enough to break the Cooper pairs in the Al [14].

4.2 Readout Electronics and Data Acquisition

In Section 3.4 we touched on the operating principles of the TES readout circuits. Here we focus on the combination of the TES readout circuit design and the data acquisition system for the HVeV laser calibration experiment. We end this section by showing an example TES pulse and noise trace out of the data acquisition system and discuss the main features of the electronics noise in our readout circuit.

We start by describing the specific TES readout circuit design used in our experiment shown in Figure 4.4. The circuit shown on the leftmost portion of the figure is the cold electronics that were previously shown in Figure 3.3. The TES is heated to its critical temperature using the Joule heating provided by the voltage bias that is applied to it through the resistor (R_b). There is a shunt resistor with high resistance ($R_{sh} = 50\ m\Omega$) in parallel to the TES, which guarantees that the current of the TES does not fluctuate significantly. The inductor coil (L_{in}) is in parallel to the TES and has the same current as of the TES, so we can measure the current through the inductor instead of the TES so as not to disturb the TES. An array of SQUIDs is used for measuring the magnetic flux in the inductor coil, which can be converted to the current. For more details see Refs. [14, 72]

The readout portion of the circuit, including the SQUID array, is shown in the rightmost portion of Figure 4.4. More details about SQUIDs can be found in Ref. [74]. For our purposes, we note that the inductor in series with the TES induces a magnetic flux in the SQUIDs. When this magnetic flux is larger than a critical value, a voltage appears across the SQUID. This voltage has a periodic dependence on the magnetic flux; however, for the stable operation of the TES measurement, the value of the flux should be kept constant. This is achieved by using flux-locking amplifiers and a feedback loop that applies negative feedback to the SQUIDs to ensure that the value of the flux remains constant. The flux-locking amplifier also amplifies the signal and suppresses the noise [21]. The current output which goes to the DAQ is shown in the top right of the figure.

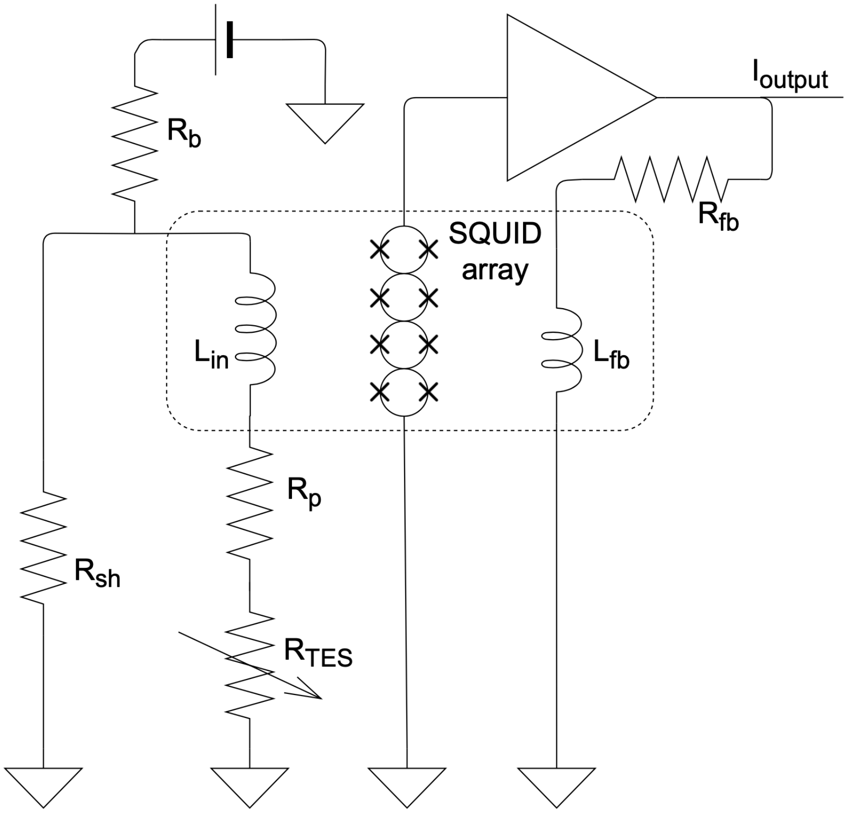

Figure 4.4: This figure shows a schematic of the TES readout circuit for the HVeV detector. The portion of the circuit on the left was previously shown in Figure 3.3. The component of the SQUID chip is shown inside the dashed box in the middle. The top right of the figure represents the output current (I_{output}) which is sent to the DAQ, flux-locking amplifier, feedback resistor (R_{fb}) and feedback inductance (L_{fb}) [14].

We now turn to describe the data acquisition system. The measured current for the inner and the outer QET channels is recorded continuously using a NI PCIe-6374 Analog to Digital Converter (ADC) card with a sampling rate of 1.515 MHz, or once every $\sim 0.6\,\mu$s [17]. Each data series consists of one hour of data-taking and is divided into 3600 files (each 1 second) [18].

With a description of the TES readout circuit and DAQ in mind, we can now look at what a nominal TES pulse and its accompanying noise look like. Figure 4.5 shows a time window around an example TES pulse from an interaction, which we will refer to as a signal, and an example trace when there is no interaction; this provides a good measurement of the noise of the system. While it is not obvious visually, our electronic noise is correlated in time and is also frequency-dependent.

Since the pulse shape is mostly dependent on the TES and readout circuit parameters all pulses are expected to be similar. Figure 4.6 shows the average of many well-measured pulses in the time domain (known as the pulse shape or an optimal filter template) on the left and the power of the noise as a function of frequency (known as the noise power spectral density) on the right. The data processing algorithm takes the pulse shape and the noise power spectral density (PSD) as inputs. We will discuss the details of the data selection and data processing in the next section.

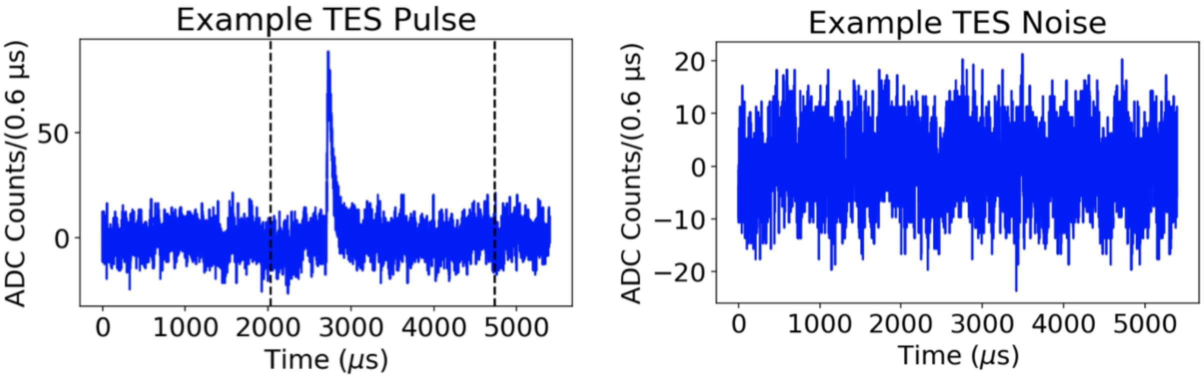

Figure 4.5: This figure shows an example TES pulse (left) and noise trace out of the data acquisition system (right). Note that a 2.7 ms region of time around the pulse peak is known as an event, which is shown with dashed lines.

4.3 Events, Triggering and the Phonon Energy Reconstruction from the TES Readout

Measuring a dark particle interaction is challenging because typically a small amount of energy is expected to be deposited which can easily be lost in the noise. On the other hand, we can use the fact that the noise levels in our experiment are correlated in time to improve our sensitivity. For these reasons, we use a number of sophisticated algorithms to analyze the data. In this section, we discuss splitting the data into regions of time known as events, the methods used to identify events, known as triggering, and the methods to estimate the collected energy.

Since interactions occur rarely in the detector and we readout the current at all times, most of the recorded data in our experiment consists of pure noise necessitating an algorithm to pre-select

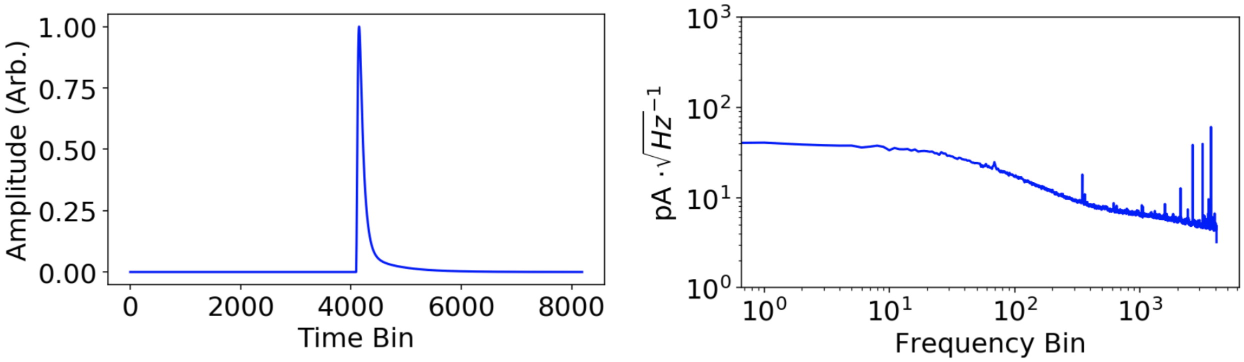

Figure 4.6: This figure shows two of the inputs for our reconstruction algorithm. Since the noise and signal shape shown in Figure 4.5 are mostly determined by the TES and readout circuit we expect most events to have the same pulse shape. The pulse shape as a function of time, determined by averaging many events in the real data and normalizing it to have a peak value of 1.0, is shown on the left and the noise PSD as a function of frequency is shown on the right. As shown in the plots, the electronic noise in each time bin is correlated in time and is frequency-dependent.

regions of time, which is what we call an event, within the readout where there is an interaction. The left plot of Figure 4.5 shows such an example. The selection of these events when the size of the pulse is small is non-trivial and is referred to as triggering. The left plot in Figure 4.7 shows a sketch of an example pulse from a low-energy interaction with its accompanying electronic noise. One can see by eye the clear presence of a signal, but the peak amplitude is not large compared to the highest points in the trace due to noise. For example, at no point does the peak go above a reasonable threshold for identifying it as an event.

We begin by first describing the time window for doing the energy measurement. In our experiment, we choose a time window that is 2.7 ms long (4096 time-bin samples) and is designed to fully contain the TES output for a single interaction. Each event is defined around the time when the current reaches its peak. This time is called the trigger point. The times before and after the trigger point are referred to as the pre-trigger and the post-trigger regions. The pre-trigger region is configured to be 675 μs long while the post-trigger region is 2034 μs long [20, 18]. An example of a time window with a pulse was shown on the left-hand side of Figure 4.5.

To understand our triggering algorithm we start with a simple model and later incorporate how the optimal filter is incorporated. A simple triggering algorithm starts with selecting a time window that corresponds to the length of an event and looks for evidence of a pulse, for example if during any period of the time window the number of ADC counts is above some threshold. In this case, then the trigger registers the data as an event and identifies the time when the largest number of ADC counts is registered as the trigger point. The example shown on the left-hand side of Figure 4.7 would not have triggered to identify the event.

To have the ability to better distinguish small signals from the noise for both triggering and estimating the phonon energy, we process the data using a more sophisticated algorithm called an optimal filter [20]. The right plot in Figure 4.7 shows an example of the optimal filter values for the times around the readout pulse. We now describe the details of the optimal filter and come back to how it is used in triggering later.

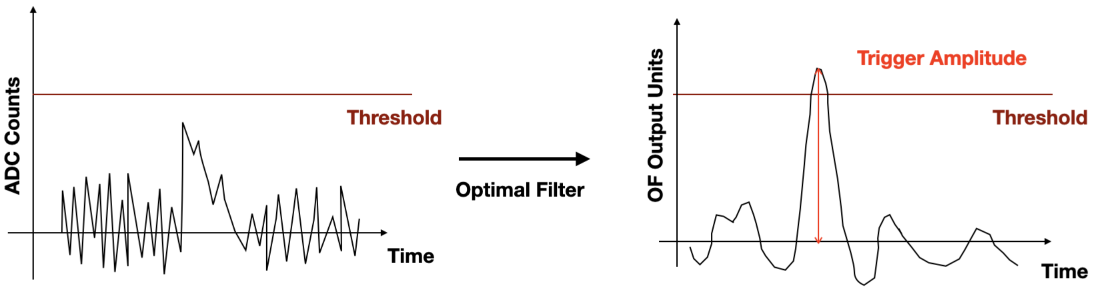

Figure 4.7: This figure shows two simplified diagrams of trigger methods that could be used for identifying the presence of an interaction from the phonon energy measurement out of the DAQ. On the left is what comes directly out of the DAQ and could, in principle, be used for triggering by comparing the peak of the pulse to a threshold. The right, which we use, considers the amplitude output of the optimal filter for a series of time windows, each with the same event length, plotted as a function of time, which is better for triggering. Note that we have chosen to show only a small window of time around the pulse, and on the left we refer to that window of time as an event. Events with interactions within them are identified using the method on the right, when the amplitude of the pulse goes above a specified threshold. Also note that the y-axis units on the left are in ADC counts (the units of the DAQ pulses), and after applying the filter, the filtered pulse is in optimal filter output units (μA).

For our case, where the shape of the signal pulse is well known from the QET design and the noise is correlated in time, there is an optimal solution to identify a signal and measure its

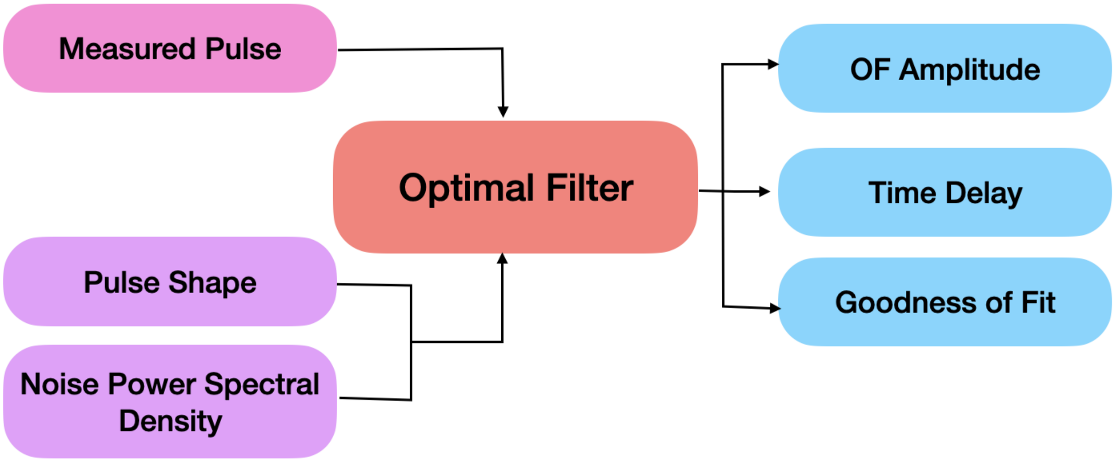

Figure 4.8: A flow chart of how an optimal filter measures the amplitude of an input pulse. The inputs of the optimal filter are the Measured Pulse (for example the left-hand side of Figure 4.5) which is compared to the expected Pulse Shape (called a template, and shown in the LHS of Figure 4.6) and the Noise Power Spectral Density (PSD, and shown in the RHS of 4.6). The filter itself uses the χ^2 method in Equation 4.1 to determine the best fit scaling of the template (both in time and amplitude), and reports the minimized χ^2 as a measure of goodness-of-fit. Diagram recreated from Ref. [16]. The output amplitude is both used in triggering and in an estimation of the energy.

amplitude for an event. This solution, known as an optimal filter, is done in frequency space and is used both for triggering and measuring the energy [16]. A flow chart that shows how the TES pulse (for example the one shown in Figure 4.5) is converted into an energy measurement using an optimal filter is shown in Figure 4.8. As shown in the flowchart, the optimal filter uses the expected pulse shape and the noise PSD as a function of frequency (both shown in Figure 4.6), then performs a χ^2 minimization to find:

$$\chi^2_{min}(A_{OF}, t_0) = \int_{-\infty}^{\infty} \frac{|v(f) - A_{OF} \cdot e^{-i2\pi f t_0} \cdot s(f)|^2}{J(f)} df, \tag{4.1}$$

where A_{OF} is the optimal filter amplitude which is proportional to the energy, $e^{-i2\pi f t_0}$ is the time delay in the frequency domain, $v(f)$ is the measured pulse in the frequency domain, $s(f)$ is the expected pulse shape in the frequency domain (template), and $J(s)$ is the power spectral density of noise. Note that after minimization both free parameters, the pulse amplitude (A_{OF}), and time delay with respect to the expected pulse shape (t_0 in s units), as well as the goodness-of-fit (χ^2_{min}), are reported as the output of the optimal filter and used in the final event selection. We also note that a constant factor is used to converted A_{OF} to μA units, and that this value is proportional to E_{Phonon} as described later.

With the optimal filter now described, we can finalize our description of the trigger as well as move forward with the analysis of the data. The triggering is done by selecting a time window with the same size as an event and running it through the optimal filter which reports an amplitude. By repeating this process as we shift the time window by a single time bin of the TES readout, we map out the amplitude as a function of time as shown on the right-hand side of Figure 4.7. One can think of this as being a time window which is considered by the trigger. In the case where that amplitude goes above a set threshold, we say that we have identified an event. In that case, the trigger considers the optimal filter amplitude for multiple time windows and identifies the highest value, and the time bin with that value is set as the trigger point for the event. One can think of the reconstruction of the data as running the optimal filter separately on the set of events that pass the trigger and it reports the values of optimal filter amplitude (A_{OF}), time delay (t_0), and goodness-of-fit (χ^2_{min}) for all such events, which are considered for later analysis. Note that in the HVeV program, the triggering and the energy measurements are done together using a program called Continuous Readout Processing (CRP) with triggering performed based on the sum of the two channels and the optimal filter results from each channel reported separately [14, 18].

5. HVeV Laser Calibration Experiment and Results

Having reviewed the physics of the solid-state detectors, the specific design of the HVeV detector and the phonon energy measuring methodologies, in this chapter we describe the HVeV laser calibration experiment and its results. To summarize, the HVeV detector is housed in a light-tight copper box, and a laser source emitting red photons is mounted on top of the detector. The detector is biased at 100 V and cooled to cryogenic temperatures ($\sim$ 50 mK). Data taking occurred in 2019 and the data triggering and processing are done after recording the data. The processed data, including the measured optimal filter amplitude for every event, is then calibrated and multiple selection criteria are applied to the data to reject the events that were recorded in sub-optimal conditions or show evidence of poor measurement. The final spectrum shown in Figure 1.9 has multiple quantized peaks corresponding to the number of electron-hole pairs that are fully-amplified but with a number of events between the peaks, which are caused by the presence of impurities/defects in the crystal as described in Section 2.5.

We start with an overview of the experimental setup and data sets in Section 5.1. In Section 5.2, we describe the corrections and calibrations applied to the data. Then in Section 5.3, we describe the criteria used to select the final set of data. In Section 5.4, we discuss the main features of the phonon energy spectrum and introduce a simplified model to describe the data. After describing the experiment and its results in this chapter, in the following chapters of this thesis we turn to discuss the simulation of the experiment, show the simulated data and compare it with the real data.

5.1 NEXUS Facility, HVeV and Laser Experimental Setup, and Data Taking Period

In this section, we first discuss the facility and the setup of the laser and the HVeV detector. Then, we describe the operation of the experiment. We finish by discussing the data-taking periods used in this analysis.

The experiment to calibrate the HVeV detector with a laser was operated at the Northwestern

EXperimental Underground Site (NEXUS) in 2019 [75]. The NEXUS facility is a surface laboratory with $\sim$ 300 m.w.e (meter water equivalent) overburden to reduce cosmic ray backgrounds. Figure 1.8 shows two images of the experimental setup in the lab. The left image shows the VeriCold Adiabatic Demagnetization Refrigerator (ADR) and data acquisition system. The right image shows the items that are placed inside the fridge. We note that the SQUID board is kept at $\sim$ 1.3 K, the heat sinks at $\sim$ 200 mK, and the air-tight copper detector box at $\sim$ 50 mK along with the Niobium packaging used for shielding the detector from the magnetic fields of the ADR [53]. The detector is mounted between two printed circuit boards (PCB) for thermal and electrical connection with the fridge and the electronic readout circuit [17].

The top surface of the HVeV detector is bombarded with photons from a 635 nm laser diode which corresponds to a photon energy of 1.95 eV [17]. The laser diode is connected to a vacuum feed-through at room temperature. The other end of the vacuum feed-through is connected to two pieces of KG-3 glass at 1.5 K, which are connected to a single-mode optical fiber which ensures that only red photons reach the detector. The single-mode fiber is connected to a plastic optical fiber which is fixed at the top surface of the detector using an Ecosorb epoxy [53]. To identify the events that are due to a laser pulse and only use them in the analysis, a transistor-transistor logic (TTL) signal is provided simultaneously with each laser shot [18, 20].

The HVeV detector was operated for 18 days at three different voltage bias values (0 V, 60 V, and 100 V) for dark matter searches as well as with laser calibration or a cobalt source nearby. Although multiple data sets with different configurations were recorded in the experiment, in this work, we only use the 100 V data with the laser turned on which was collected in the first 8 days. The coincident data with the TTL signal was processed using the algorithms described in the previous chapter, where the optimal filter amplitude (A_{OF}), the time delay (t_0), and the goodness-of-fit (χ^2_{min}) were determined.

It is worth mentioning that although a comprehensive study of the sources of the background interactions with the HVeV detectors in the NEXUS facility does not exist, preliminary evidence suggests that the background interactions are small enough to ignore them in the analysis of the laser calibration data. More information about the sources of the background interactions in underground facilities can be found in Ref. [16]. The latest background study of the HVeV detectors in the NEXUS facility can be found in Ref. [76].

5.2 Phonon Energy Calibration

Since the operating conditions of the experiment change over time, the relationship between the deposited phonon energy (E_{Phonon}) and the amplitude reported directly out of the optimal filter (A_{OF}^{Raw}) can vary, necessitating a correction of the measurement values to nominal operating conditions which we will refer to as A_{OF}. The main corrections applied to the data are for the temperature and the voltage variations. After correcting for the fluctuations in the temperature and the voltage, the last step is correcting for non-linearities due to the non-linear TES response (see Figure 3.2) and calibrating the results. While we present a quick overview of the most important calibration steps, a more comprehensive description of all calibration steps can be found in Ref. [21].

We begin by describing the initial event selection and correction for voltage and temperature variations. The readout collected by the DAQ is run through the reconstruction algorithm, which selects events and determines the value of A_{OF}^{Raw} for each. Those events which are coincident with the TTL signal from the laser are considered for analysis. Next comes the corrections to A_{OF}^{Raw} for the temperature and the voltage variations to create a consistent measurement of amplitude to nominal operating conditions. Based on Equations 3.1 and 3.2, the resistance of the TES is highly dependent on the detector temperature, so any temperature fluctuations during the operation require a correction. The temperature of the fridge was measured by a thermostat thermally connected to the detector [17] and the temperature fluctuations were corrected for each day separately. Similarly, since the amount of Luke amplification is mostly linearly dependent on the voltage of the crystal, a simple linear correction was applied using the measured voltage of the circuit [17]. The corrections can be thought of as: $A_{OF} = F(A_{OF}^{Raw})$, where F is a function of the temperature and voltage, and includes a conversion to μA.

The final calibration takes into account the non-linear relationship between the corrected A_{OF}

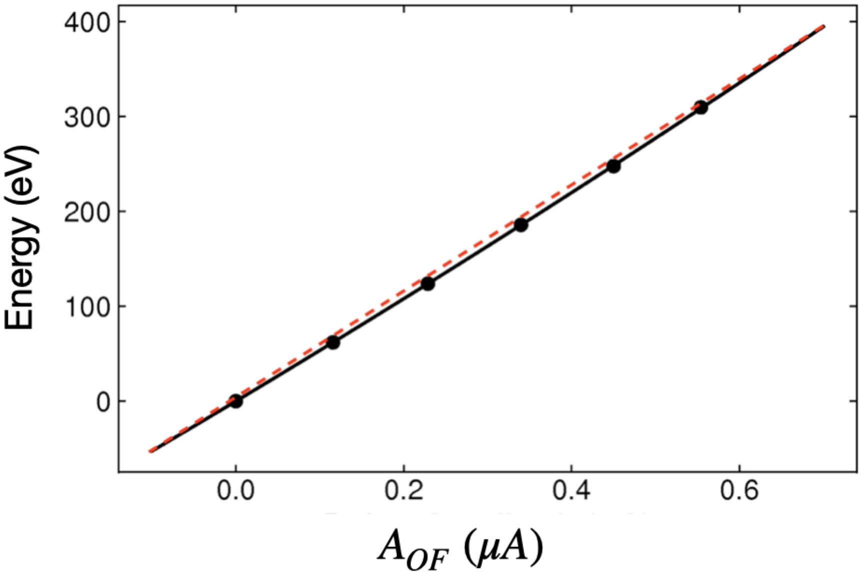

Figure 5.1: This figure illustrates the last step of the calibration process for the HVeV laser experiment where the x-axis is the corrected A_{OF} in μA and the y-axis is the expected E_{Phonon} from Equation 2.6. The data points are drawn from the peaks in Figure 1.9, the black line shows the best fit using Equation 5.1 and the red straight line is there to illustrate the difference if we had assumed a linear fit [17, 18].

values and E_{Phonon}, which comes from the non-linear shape of the resistance vs. temperature curve shown in Figure 3.2. The calibration procedure was done for each day separately and is depicted in Figure 5.1 for our data. Note that the data points are taken from the peak values in the A_{OF} distribution, and the expected E_{Phonon} value is calculated from Equation 2.6. The fitting is done using the following function:

$$E_{Phonon} = a \cdot A_{OF} \cdot (1 + b \cdot A_{OF}), \tag{5.1}$$

where a and b are the calibration constants [17, 18].

5.3 Event Selection Criteria

In this section we describe the two sets of criteria used to select the final events for data analysis as listed in Tables 5.1 and 5.2. The first set of requirements selects the time periods during which the detector was operated stably in optimal conditions, and the second set of requirements selects the well-measured events. The first set is called livetime selection criteria, and the second set is called data quality selection criteria. While we provide a quick summary of the different selection criteria in this section, more detail about the procedure of each step can be found in Ref. [18, 21].

We begin with describing the livetime selection criteria (cuts) to choose the time periods where the detector was performing optimally and stably. These are implemented using data cuts based on two quantities as described in Table 5.1, which include the temperature of the fridge and the stability of the TES measurements. To summarize, the processed data is divided into intervals with a specific length and all events in that interval are studied. The average temperature for the interval is determined, as well as the average number of ADC counts for all the pre-pulse regions; this later quantity is called the Mean Base. The periods of time where either the temperature or the mean base are away from the average by an amount more than the tolerance, are discarded from the analysis. The mean and RMS values for the thresholds are described in Refs. [18, 21].

Selection Criteria	**Tolerance**	**Notes**
Temperature	$< 3\,\sigma$	- Selects the periods of time when the detector temperature is within an acceptable range. - Done in two stages with rough and fine data binning: (i) applied to 30s long intervals and then (ii) applied again to 1s long intervals.
Mean Base	$< 2.5\,\sigma$	- Selects the periods of time when the TES is reading out as expected when there are no interactions. - The Mean Base variable is determined as the average current from all the pre-pulse regions for the 1s intervals after the temperature cut. It is required to be within $2.5\,\sigma$ of the observed value for events in the peak to indicate that the detector was operating in stable condition.

Table 5.1: A summary of the livetime selection criteria applied to the raw data which includes cuts based on the detector temperature and the stability of the TES readout along with the tolerance and the purpose of each cut. The data is separated into intervals of a given length (specified in the notes column), and those periods which are out of tolerance are excluded from the analysis. More details about the variables as well as the tolerances selected are described in Ref. [18, 21].

After selecting the data periods with stable detector conditions, the next step is to apply the data quality cuts which are done on an event-by-event basis for all events that are coincident with a TTL pulse, as described in Table 5.2. The first two cuts are based on the outputs of the optimal filter algorithm described in Section 4.3 and given in Equation 4.1, the time delay (t_0) and the goodness-of-fit (χ^2_{min}). The last cut is based on the results of the veto detector. We next describe how each helps identify well-measured events:

- Time Delay (t_0) Cut: This cut is designed to remove events that have multiple large peaks or are otherwise noisy. In the case where there are multiple large peaks close to each other in time (known as pileup events), the largest peak will register as the trigger point but the optimal filter algorithm (Equation 4.1) might select another peak in the fitting. This will show up as a large value of t_0. This cut also helps identify cases where a fluctuation of a noise trace might erroneously produce a trigger and be identified as an event. The criteria for the threshold is determined from the real data; events that have a t_0 value that is more than $3\ \sigma$ away from the average were discarded [18, 20].

- Goodness-of-Fit (χ^2_{min}) Cut: This cut effectively removes the events with an irregular pulse shape as well as pileups. The criteria for the threshold are again determined from the real data but are done as a function of energy based on the results from the peaks. Thus the mean and RMS of each peak are calculated separately, and the events with a χ^2_{min} more than $3\ \sigma$ away from the expected value are removed [18, 20].

- Veto Detector Cut: The events that happen at the same time in the HVeV detector and the adjacent veto detector are also discarded because it is very likely that those are caused by electronic noise or a cosmogenic background [18, 20].

Figure 5.2 depicts the calibrated phonon energy before and after applying the livetime and the data quality cuts and is the same as Figure 1.9.

Selection Criteria	**Tolerance**	**Notes**
Time Delay (t_0)	$< 3\ \sigma$	Designed to remove events with either large peaks (pileup events) or where the noise fluctuated to pass the trigger.
Goodness-of-Fit (χ^2_{min})	$< 3\ \sigma$	Designed to remove events with shape that is not consistent with the template, for example pileup events.
Veto Detector	Veto hit exists	Removes events that occurred simultaneously in the HVeV and the veto detector, as these events are most likely caused by electronic noise or cosmogenic background.

Table 5.2: A summary of the event-by-event data quality selection criteria applied to the raw data which includes cuts based on the output of the optimal filter, the time delay (t_0) and the goodness of the fit (χ^2_{min}), as well as the veto detector. The tolerances for the cuts, and the methods to determine them are highlighted in the text and described in more detail in Ref. [18, 21].

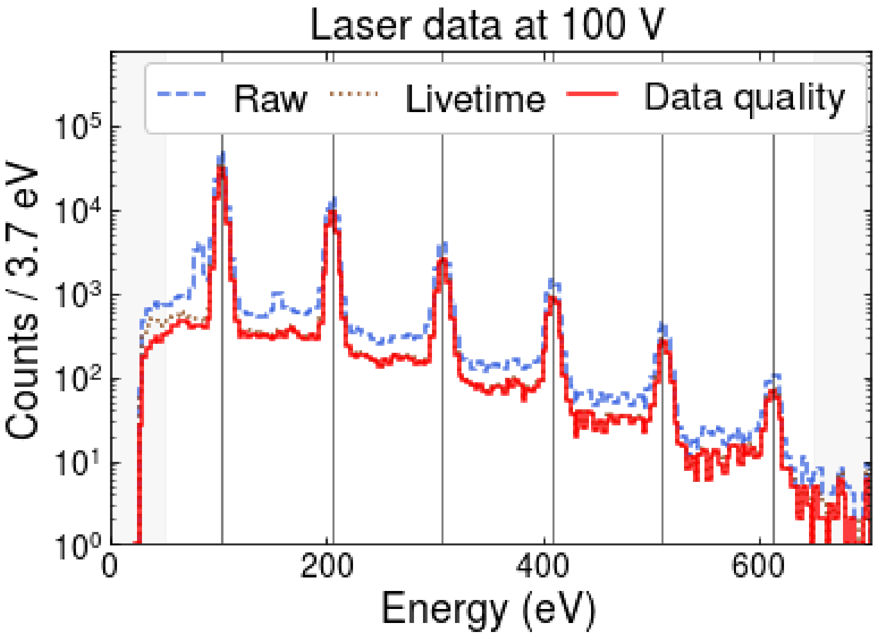

Figure 5.2: This figure shows the calibrated phonon energy before (raw) and after the livetime and data quality selection criteria [18].

5.4 Main Features of the HVeV Phonon Energy Spectrum, and a Simple Model

In this section, we take a closer look at the HVeV laser phonon energy spectrum and describe its main features after energy calibrations and the data selection requirements. With that in mind, we describe a simple model of the expected phonon energy measurement and compare it to the data.

The E_{Phonon} spectrum shown in Figure 1.9 (or the red curve in Figure 5.2) depicts the number of events as a function of the total collected phonon energy. The dominant features are:

- The spectrum has seven distinctive peaks that correspond to the number of electron-hole pairs that went through the full Luke amplification since the laser emits multiple photons per pulse. In principle, the location of each peak can be determined from Equation. 2.6.
- The background between the peaks is caused by the presence of impurities in the silicon crystal, which leads to charge trapping and impact ionization as described in Section 2.5.
- The RMS of the peaks is expected to be due to a combination of the detector resolution and noise.
- Note that the zeroth electron-hole pair peak is not seen in the data because low-energy events are not selected by the trigger.

To illustrate our understanding we compare the data to a simplified model. We build up this model by starting with the case where the crystal has no defects/impurities, then we add the charge trapping and impact ionization. Finally, we compare our model with the real data using some nominal parameter values. Note that we only focus on the assumptions and results of the model. Information about the mathematical expressions used for building this model can be found in Ref. [65].

The simplest version of the model assumes that the number of photons hitting the detector and getting full amplification at the same time follows a Poisson distribution, the width of the peaks is determined by the resolution of the detector and that the detector crystal is perfectly pure. The

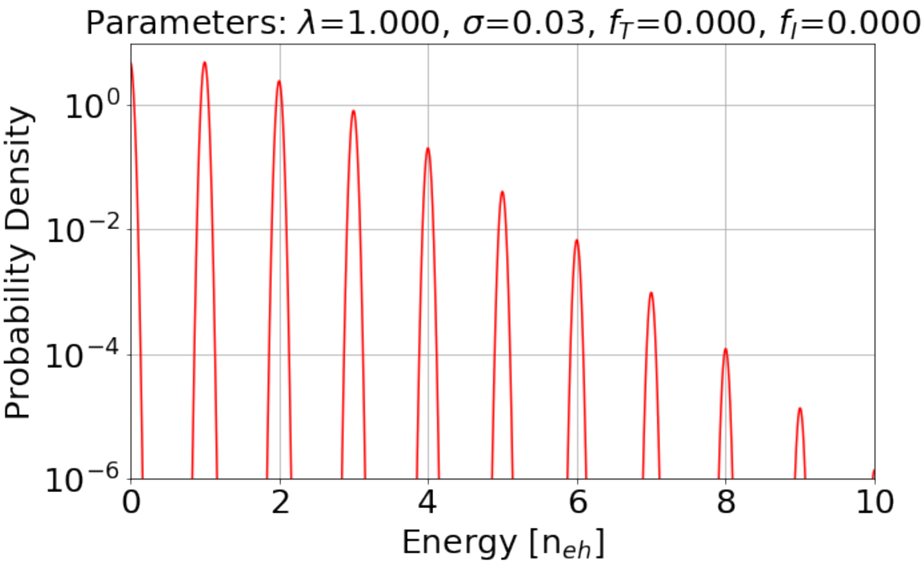

Figure 5.3: A model of the expected probability density of the phonon energy (in the number of electron-hole pairs energy unit) for the detector response to a laser shooting photons at it. In this scenario, the model assumes that the detector has no defects/impurities (charge trapping, f_T, and impact ionization, f_I, are both set to zero), the number of fully amplified eh pairs at the same time follows a Poisson distribution with $\lambda = 1$, and the resolution of the energy measurement, σ, is 3% of the electron-hole pair energy.

predictions for the model with $\lambda = 1$ and an energy measurement resolution of 3% of the electron-hole pair energy are shown in Figure 5.3. Note that the expected phonon energy probability density is plotted as a function of the number of electron-hole pairs' energy.

The next step is adding the effects of the defects/impurities in the crystal to our model separately which allows us to estimate the values for each. As mentioned in Chapter 2, the defects/impurities in the crystal can cause charge trapping and impact ionization. Figure 5.4 depicts the predictions for the same basic model as Figure 5.4 but with the addition of only charge trapping (left) and only impact ionization (right), where we assume a flat rate of events between the peaks from each contribution. The fraction of electron-hole pairs that go through charge trapping and impact ionization processes are characterized by the charge trapping and impact ionization fractions, f_T and f_I respectively. In the left plot, f_I is set to zero, whereas f_T has three distinct values as given in the legend. Charge trapping has an impact on the background between all peaks. In the

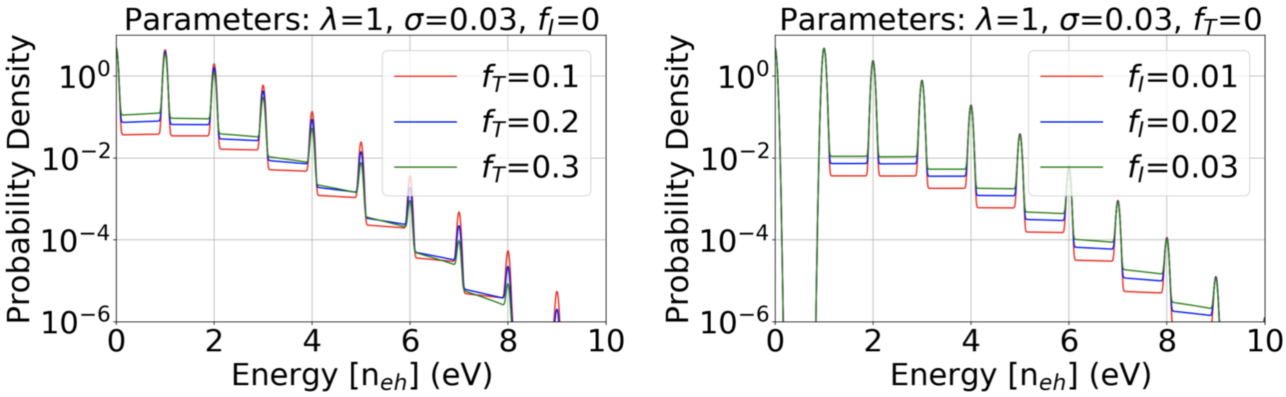

Figure 5.4: The predictions for the same simplified model shown in Figure 5.3, except we have added the effects of only charge trapping (left) and only impact ionization (right). The charge trapping and impact ionization fractions, f_T and f_I, are defined as the fraction of the electron-hole pairs that go through those processes and the energy distribution of the resultant phonon energy is assumed to be flat between peaks. The figure on the left is for the case when $f_I = 0$ and we see that the number of expected events between each of the peaks changes as we change f_T. On the right, when $f_T = 0$ and we see that the number of expected events between peaks also changes. However, no value of f_T allows for the creation of events below the peak. For this reason, we will be able to estimate the value of each parameter separately.

right plot, f_T is set to zero, whereas f_I has three different values, as shown in the legend. Impact ionization, unlike charge trapping, has no effect on the background between the zeroth and first electron-hole pair peaks. After the first electron-hole pair peak, it merely impacts the background between the peaks. As a result, we can independently estimate the amount of each parameter.

Figure 5.5 compares the data and the model with a reasonable set of parameter values. Note that the energy for the data has been scaled to the number of electron-hole pairs and the number of events has been converted to a probability density. To get a qualitative agreement, the parameter values are set to $\lambda = 1.00$, $\sigma = 3\%$, $f_T = 0.13$ and $f_I = 0.01$. As shown in the plot there are regions with good and bad qualitative agreement. There are significant disagreements at low energies, near zero because the model does not account for the effect of the trigger, which discards the events with low energy; this also accounts for the overall scaling differences. In the region, starting midway between the zeroth and first peak, and through about the third peak there is good qualitative agreement. Above the third peak the model diverges from the data, suggesting that the

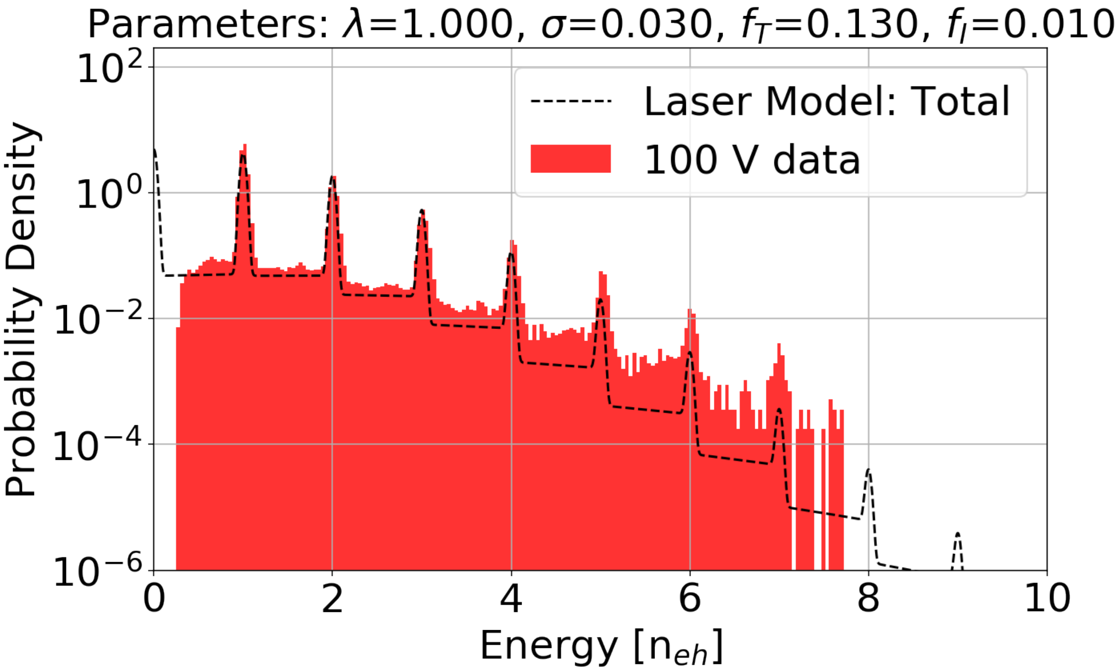

Figure 5.5: This figure shows the probability density of the energies of the events as a function of the electron-hole pair energy for the HVeV laser data at 100 V and the laser model with nominal parameter values (after scaling). We note that the model has qualitative agreement with the data for the region halfway to the first peak and below the third electron-hole pair peak, but it diverges from the data for events above the third electron-hole pair peak. Also, the model does not take into account the effect of the trigger, and that is the reason behind the discrepancy between the model and the simulation at low energies (near zero).

distribution of photons from the laser is not well described by a Poisson distribution. It is not clear why this is.

Although this model provides a good first-order approximation of the HVeV laser spectrum, the comparison between the data and the model shows that more sophisticated methods are required for a deeper understanding of the physics of the devices. For example, we would like to know which effects contribute to the detector's resolution and how much is the contribution from each. Do we need to revise the Poissonian laser assumption? How can we add the effects of the trigger to our model? The full SuperCDMS Simulation infrastructure can help us answer these questions. We describe the SuperCDMS Simulation in the next chapter, show the simulation results, and compare them to the data in the following chapters.

6. Simulation of the HVeV Laser Calibration Experiment

In this chapter, we shift gears from the description of the HVeV laser calibration experiment to its simulation. First, we provide an overview of how the simulation infrastructure mimics the data-taking as a whole, then we describe the different simulation components along with their names and how they all operate together as shown in Figure 6.1. To summarize, the simulation is done in two main stages: (i) the simulation of the external particles that interact with the detector (SourceSim) and (ii) the simulation of the detector, which includes the semiconductor crystal, the sensors, the readout electronics and noise (DetectorSim). The outputs of DetectorSim are then processed using the same reconstruction algorithm as the real data. While we present a summary of the simulation infrastructure, more comprehensive information can be found at Refs. [16, 63, 64, 77].

In Section 6.1, we present the full simulation infrastructure and our goals in this work. In Section 6.2, we focus on the simulation of the photons that are emitted from the laser and interact with the detector using SourceSim. In Section 6.3, we review the detector response to the photon hits using DetectorSim. In particular, we describe the simulation of the propagation of the phonons and charges under high voltage bias in Section 6.3.1 and the charge trapping and impact ionization modeling in Section 6.3.2. These parts of the simulation are done by a package called CrystalSim. In Section 6.4, we focus on the simulation of the TES superconducting sensors, which is done by TESSim. Finally, in Section 6.5, we describe the simulation of the readout electronics, data acquisition system, and noise, called DAQSim and NoiseSim, respectively.

6.1 Overview and Goals of a Full Simulation

In this section, we first present an overview of the full simulation infrastructure and how the different components operate together. Then we outline our goals in simulating the HVeV laser calibration experiment.

The simulation infrastructure is designed to closely resemble the actual data flow in the real experiment as shown in Figure 6.1. The right-hand side shows the data flow in the real experiment

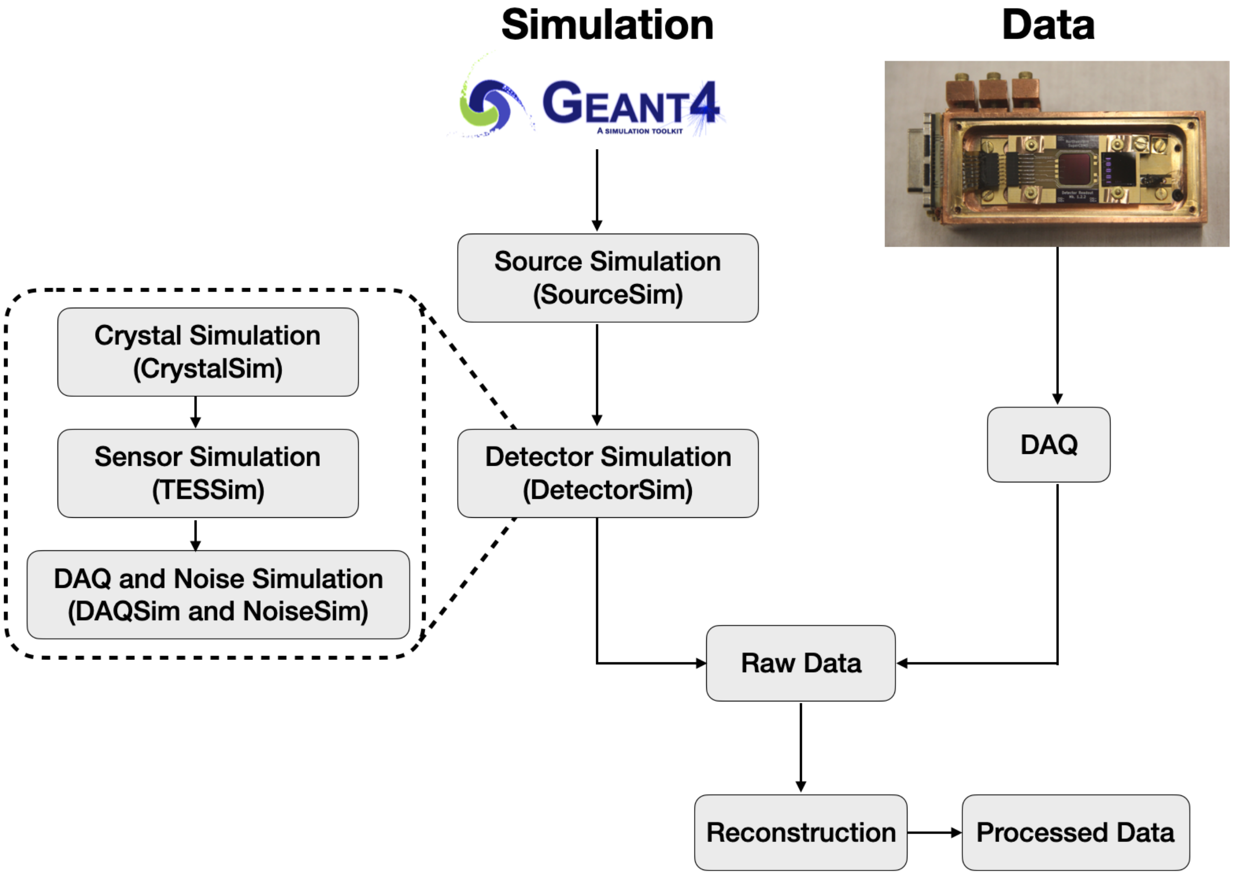
Simulation
Data
GEANT4
A SIMULATION TOOLKIT
Source Simulation (SourceSim)
Crystal Simulation (CrystalSim)
Sensor Simulation (TESSim)
DAQ and Noise Simulation (DAQSim and NoiseSim)
Detector Simulation (DetectorSim)
DAQ
Raw Data
Reconstruction
Processed Data

Figure 6.1: This diagram shows the workflow of the real data taking (right) and simulation (left). In the real experiment, the data acquisition system reads out the TES current and writes the data into the standardized raw data format. After that the reconstruction processes the data as described in Section 4.3. The simulation uses the GEANT4 toolkit from CERN to simulate the particle interactions [19]. SourceSim is responsible for simulating the external particles that interact with the detector (e.g. photons from a laser or dark matter particles). DetectorSim consists of three packages, simulation of the semiconductor crystal (CrystalSim), the superconducting sensor (TESSim), and the data acquisition and noise (DAQSim and NoiseSim). The final output of DetectorSim is raw data which is processed through the same reconstruction algorithm as the real data.

and the left-hand side shows the data flow in the simulation. In the real experiment, the data acquisition system records the output of the TES into a format known as the raw data, and it is subsequently processed by the reconstruction algorithm described in Section 4.3 [73]. The particle interactions are simulated using the GEANT4 toolkit from CERN [19]. The first step of the simulation is simulating the interactions of the external particles with the detector (e.g. photons from a laser or dark matter particles) which is done by SourceSim. The next step is simulating the detector which consists of three packages: (i) CrystalSim, (ii) TESSim, and (iii) DAQSim (which includes NoiseSim). The final output of DetectorSim is stored in the same raw data format as the real data and processed using the same reconstruction algorithm.

Since the goal of this thesis is to understand the workings of the HVeV detector, we describe the sophisticated models of the standard CDMS simulation in more detail, and compare its predictions to the data from the periods when the laser was shining on the detector. To foreshadow its use, we describe the simulation infrastructure and its components in this chapter. In Chapter 7, we run all of the stages of the simulation for the simple case of the single-photon interactions with the detector. Then we proceed with multiple-photon interactions with the detector in Chapter 8. Finally, in Chapter 9, we tune a number of simulation parameters and present our final simulation results and compare them to the real data.

6.2 Simulating Photons from a Laser Source: SourceSim

The simulation procedure starts with SourceSim, which is responsible for stimulating the incoming particle including any interactions before they reach the detector as well as the initial interaction in the detector. In principle, it can include particles from the background sources like cosmic rays, radioactive particles close to the detector, particles from a laser source, or dark matter particles. After defining the geometry of the experimental apparatus, the interactions between the incident particles and the particles in the detector are simulated using the GEANT4 toolkit [16, 19].

The output of SourceSim includes the location and energy of the electrons and nuclei that had a recoil during the interaction. For the purposes of the crystal response simulation, CrystalSim, there are only two types of external interactions, and both are described by the response of the particles in the detector. Interactions with the electrons are known as electron recoil events. In this case, either the full energy of the incident particle is absorbed, giving the full energy to the recoil, or the particle scatters giving only part of its energy to the recoil electron. The scattered particle can either interact again with the crystal, or leave forever. Similarly, the incident particle can interact with a nucleus, in what is called a nuclear recoil. SourceSim ends by producing the set of locations and energies of all the electron recoil and nuclear recoil interactions.

For the simulation of the HVeV laser calibration experiment, we would ideally want to simulate the laser source emitting photons and interacting with the atoms in the lattice using SourceSim. However, since the simulation of the photon interactions at these low energies was not ready at the time of this work, we used an alternative method for simulating the laser source where the photon interactions are simulated by an electron recoil event with the photon energy. The location is chosen based on the expected position distribution of the photons from the laser source. For the silicon crystal, the penetration depth of 1.95 eV photons is expected to be $\sim$ 0.05 mm [78]; the interaction probability is modeled as falling off exponentially in the Z direction from the top surface.

6.3 Detector Response to Energy Deposits from Photons: CrystalSim

We next describe the simulation of the detector crystal response to the photon energy depositions using CrystalSim. In Section 6.3.1, we go over the simulation of phonon and charge creation and propagation in the crystal under a voltage bias. Then in Section 6.3.2, we describe the simulation of charge trapping and impact ionization.

6.3.1 Phonon and Charge Creation and Propagation Under Voltage Bias

The output of SourceSim, with the location and energy of all the electron and nuclear recoils, is taken as the input to CrytalSim [16]. This information is used to create both primary phonons and electron-hole pairs as described in Section 2.2. For our case, since the photons only interact with electrons in the lattice, only electron recoil events are created. The number of the generated charges and their energies are then calculated based on Equation 2.2. For simplicity, the simulation only models electron recoil interactions as creating electrons and holes and giving them the appropriate amount of kinetic energy to conserve energy.

The next step is simulating how the electrons and holes propagate through the detector crystal and interact with the lattice to create Luke phonons as described in Sections 2.3 and 2.4. The motion through the lattice is simulated by solving the equations of motion for the charges under a high voltage bias taking the lattice constraints into account, as well as the fact that they can jump between valleys [63, 79] and create Luke phonons. The electrons and holes will keep moving through the crystal until they are absorbed by the electrodes or the detector sidewalls, or trapped in one of the impurities. In both cases, at this point they are eliminated from the simulation.

After each phonon is created its propagation is simulated by using the known anharmonic decay, isotope scattering, and surface interaction (absorption and reflection) probabilities as described in Chapter 2 [62, 63]. In each, phonons can change modes, be created or decay away. Ultimately, the simulation continues to propagate the phonons until they decayed away or been absorbed by the sensors or other detector surfaces. In the case of sensor absorption, their energy will be deposited into a QET, and in the case of bare surface absorption, they will be removed from the simulation.

The last stage of CrystalSim is the process of converting the phonons into quasiparticles in the QETs. Since this process is complicated in aluminum, we make a number of simplifying assumptions. We start by mentioning that instead of simulating the exact geometry of the aluminum placement on top of the detector, we consider the probability of phonon absorption by the full rectangular footprint of an individual QET as shown in Figure 4.2 [64]. As described in Ref. [80], one can think of the internal modeling of the superconductors as taking in phonons on the one hand and partially re-emitting phonons that reenter the crystal and partially creating and passing along quasiparticles to the TES on the other. We note that any phonons emitted from the aluminum will also be propagated using the same simulation rules. Eventually, the simulation stops when all phonons have been absorbed. The output of this portion of the simulation is the set of quasiparticle arrival times, energies, and locations grouped into the two QET channels.

6.3.2 Impact Ionization and Charge Trapping

Another key mechanism that needs to be taken into account in the simulations is the effects of impurities/defects in the crystal as the charges propagate in the lattice. As discussed in Section 2.5, impurities/defects can result in the loss of phonon energy or the generation of additional phonon energy via two mechanisms: charge trapping and impact ionization. In the case of charge trapping, a moving charge can get trapped in an impurity region and is removed from the simulation. This means that we will not get the full Luke amplification. In the case of impact ionization, a moving charge can encounter an overcharged impurity region and send another charge out of its valence band. This additional charge is added to the simulation and will accelerate under the voltage bias and generate additional Luke phonons.

In the simulations, the rate of charge trapping and impact ionization is controlled with a pair of mean free path parameters which are defined as the probabilistic distance that charges can travel before encountering an impurity region that can cause charge trapping or impact ionization. Consequently, a short mean free path translates to a high rate of charge trapping or impact ionization.

6.4 Phonon Readout Sensor Response: TESSim

After the charge and phonon propagation phase in CrystalSim, the set of quasiparticles that are considered to have entered the TES is converted to a signal by the TES using TESSim. The simulation takes the time of arrival of the quasiparticles, and their energies, grouped into one of the two channels as shown in Figure 4.2, and calculates the expected TES current. TESSim calculates the current in each TES cell by applying the Kirchoff laws [81] to the circuit shown in Figure 4.4 as well as the heat flow.

Modeling the TES response ultimately boils down to two ordinary differential equations (ODE), which can be solved using ODE solvers. The differential equations take in the quasiparticle energy as a function of time as well as the cooling by the thermal bath of the silicon. The parameters of the ODEs include the conversion of quasiparticle energy into temperature change in the tungsten, and the cooling rate is determined by the temperature difference between the tungsten and the silicon as described in Equation 3.1. We then assume the temperature determines the resistance which determines the amount of current that flows using the relationship shown in Figure 3.2. The output of TESSim is the current as a function of time and put into the same time intervals as used by the DAQ. More details about the mathematical procedure used for solving the ordinary differential equations can be found in Ref. [82].

6.5 Readout Electronics, Data Acquisition, and Noise: DAQSim and NoiseSim

After simulating the TES pulses the next step is simulating the effects of the readout electronics and their noise in the data acquisition system. We note at the outset that the simulation of electronic noise effects can be turned on and off so we can study its impact on the phonon energy measurements. We first describe the full procedure of how the TESSim outputs are converted to the raw data format and then describe how the noise contributions are simulated.

The simulated TES current distributions out of TESSim are given to DAQSim as input. The TESSim pulses are in the units of μA while our DAQ reports the pulses in Analog to Digital Converter (ADC) units. The DAQSim package takes care of four key tasks: (i) converting the TES pluses from μA to ADC units ($917.504\ \mu\mathrm{A} = 1\ \mathrm{ADC}$), (ii) simulating and adding noise to the TES pulses (if NoiseSim is turned on), (iii) digitizing the combined TES currents to their nearest integer value and finally (iv) writing out the number of ADC counts in each time bin in the standard raw data format as the DAQ as described above [73].

Note that NoiseSim does its work by taking in a PSD file (described in Section 4.3) measured from the real data as an input and generates simulated noise pulses that have the same characteristics as the real data noise. For doing so, NoiseSim starts by assigning random values to the real and imaginary components of the frequency. The random values are selected from a normal Gaussian distribution with a mean of 0 and a RMS of 1. Then these random values are multiplied by the square root of the PSD at each frequency. Finally, the simulated noise trace in the frequency domain is converted to the time domain by calculating the inverse Fast Fourier Transform (FFT) [83]. We assume the noise and signal shape are uncorrelated so they are simply added before digitization. In the next chapter, we describe the results of the simulation chain, as well as the reconstruction of the data using the standard optimal filter algorithms.

7. Simulation Results for Single-Photon Interactions

In this chapter, we present the results of the simulation for the case where only one photon interacts with the detector at a time. To be clear we are simulating samples with multiple events, but each event includes only a single-photon interaction. We do this in anticipation of multi-photon simulations for a laser which we will come back to in the next chapter. In particular, since the number of photons emitted at a single time is expected to follow a Poisson distribution, but this is not what we see in Figure 5.5, we begin by focusing on the simpler case and come back to the more complex case after that.

In Section 7.1, we present an overview of the simulated sample and show the results from SourceSim. In Section 7.2, we focus on the detector response. In particular, we show the results for the total collected phonon energy in the crystal without impurities using CrystalSim and the results from TESSim, DAQSim, and NoiseSim. We add more complexity to our simulation in Section 7.3, where we simulate the effects of impurities in the crystal (charge trapping and impact ionization). Finally, in Section 7.4, we run our simulated sample through the reconstruction software and show the calibrated results.

7.1 Overview of the Simulation Configuration

In this section, we give an overview of the simulation configuration for the case of single-photon interactions with the detector using SourceSim. We start with a review of the important parameters in the real experiment and then describe the simulation configurations and show the results.

In our experiment, the laser shoots red photons which uniformly illuminates a circle on the top surface of the detector with a radius of $\sim$3 mm. We refer to this as the X and Y directions as shown in Figure 7.1, with the Z direction pointing upwards from the bottom of the device and the top surface being at Z = 2 mm. To simulate the single-photon interactions, we create a sample of 1,000 direct 1.95 eV electron recoil events with the full set of simulation parameters in Table 7.1.

Figure 7.1 shows a scatter plot of the position of energy deposits in the XY plane, and Figure 7.2 shows the position distribution in the X, Y, and Z directions.

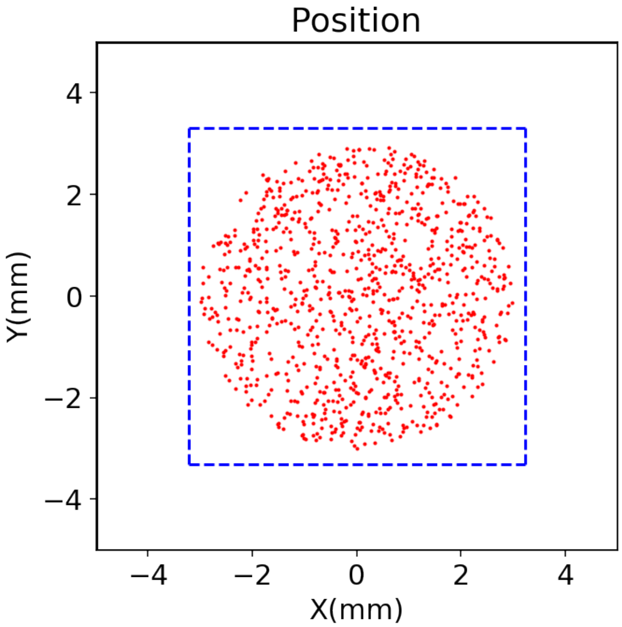

Figure 7.1: This figure shows a scatter plot of the position of the photon interactions on the top surface of the detector for our laser simulation using SourceSim. The sample contains 1,000 electron recoil direct energy deposits, each with a single photon hitting the top surface with 1.95 eV of energy and a uniform distribution for R < 3 mm. The surface area of the detector chip is 5 mm× 5 mm and the blue square shows the boundary between the two channels.

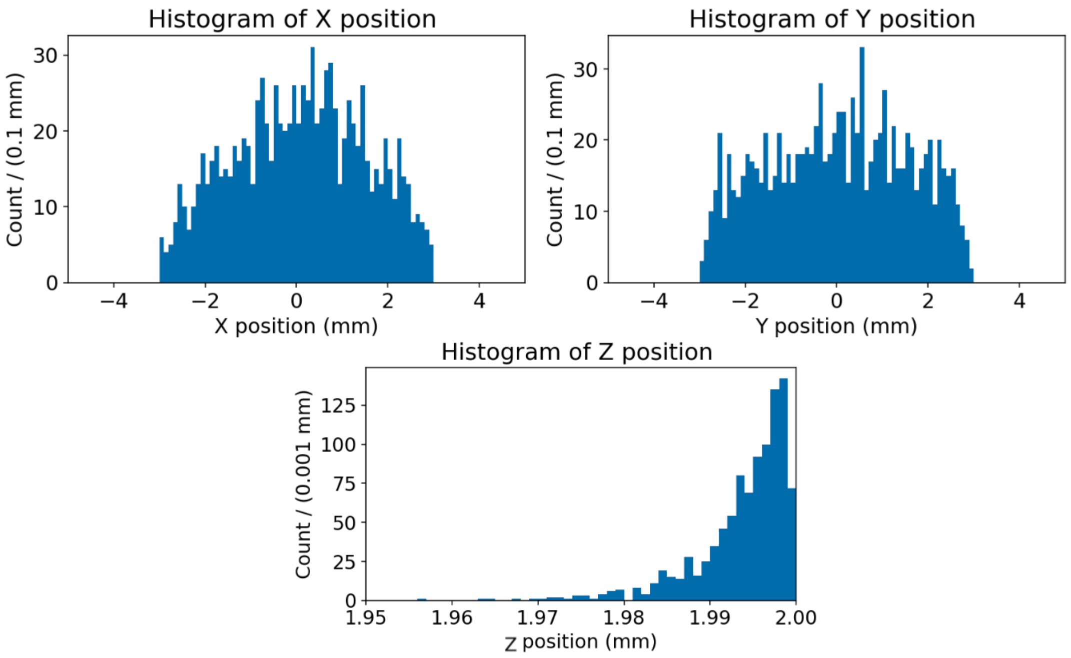

Figure 7.2: The distribution of the photon interaction positions for the sample of events shown in Figure 7.1 as a function of the interaction location. Note that the number of photons drops as a function of the depth of penetration in the Z direction, and shows no events more than ~ 0.05 mm from the top surface of the detector.

Simulation Parameter	**Value**
Number of Simulated Events	1,000 Events
Orientation of the Crystal	011
Voltage Bias Applied to the Detector	-100 V
Energy of Each Deposit	1.95 eV
Number of the Energy Deposits in Each Event	1
Position of the Energy Deposits	R: Uniform with R < 3 mm Z: Falling Exponential with 5.3 μm Depth
Crystal Impurities (Added in Section 7.3)	Charge Trapping Mean Free Path = 260 mm Impact Ionization Mean Free Path = 2700 mm

Table 7.1: A summary of the simulation configuration values used to make the two samples of events used in this chapter. The versions of GEANT4, SuperSim, and G4CMP packages used were 4-10-06-patch-02 [MT], V08-13-00, and V07-12-03, respectively.

7.2 Detector Response

In this section, we show the results for the single-photon interactions with no charge trapping or impact ionization for multiple stages of the simulation. In particular, we begin by looking at the collected phonon energy based on the simulation of the crystal for both channels as well as the sum of the two channels in Section 7.2.1. Then we will add the simulation of the TES, data acquisition system, and noise and show the simulated pluses at each stage of the simulation in Section 7.2.2.

7.2.1 Total Collected Phonon Energy in the Crystal

In our experiment, the most important parameter to measure is E_{Phonon} which is a measure of the amount of deposited energy as described in Section 2.2. In this section, we look at E_{Phonon} as absorbed by the TES which is reported by CrystalSim. We show the distribution of the collected phonon energies for each channel first and then show the same distribution for the sum of the two channels. We then quantify the probability of getting full Luke amplification as a function of the distance the photon hits below the top surface of the detector.

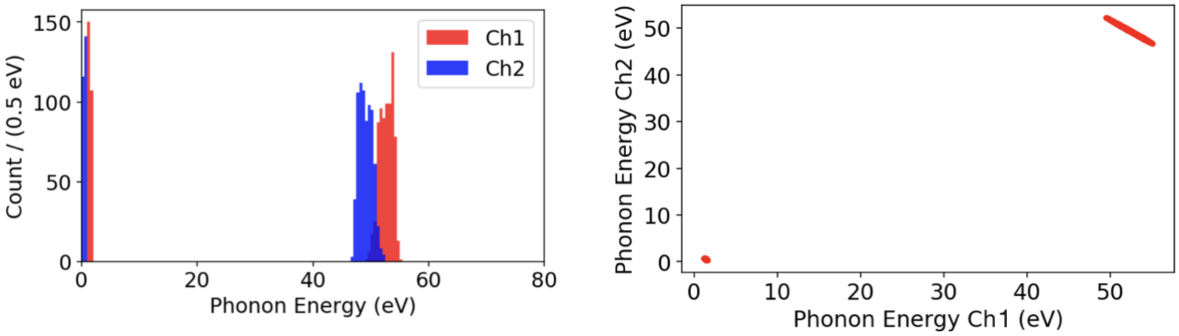

Figure 7.3: Two plots showing the distribution of E^{Ch1}_{Phonon} and E^{Ch2}_{Phonon} (left) and the relationship between them (right) for the sample of events shown in Figures 7.1 and 7.2. The figures show two groupings of energies for each channel. The high-energy peaks are all in the same events and are from the case the electron-hole pair gets full Luke amplification. The low-energy peaks are from the case where the electron-hole pair gets absorbed by the detector surfaces or recombines immediately. Note that most of the phonon energy is collected by Ch1 because the energy deposits near the center of the detector. On the other hand, there is almost the same amount of phonon energy collected in Ch2 because the phonons bounce many times before being collected.

As shown in Figure 7.1 there is an inner channel and an outer channel. We will refer to them as Ch1 and Ch2 respectively and the energy deposited in each as E^{Ch1}_{Phonon} and E^{Ch2}_{Phonon}. Figure 7.3 shows the distribution of the energies for our sample. The plots show two peaks for each channel and a comparison of the events shows that they are the same events for both channels. As shown next, the low-energy peaks correspond to events where the electron-hole pair got recombined or absorbed by a detector surface immediately after the creation and the high-energy peaks occur when there is full Luke amplification. We can understand these distributions using the equation:

$$E_{Phonon} = E^{Ch1}_{Phonon} + E^{Ch2}_{Phonon} \tag{7.1}$$

We note that even though the recombination occurred well within the inner channel (Ch1), the phonons moved throughout the crystal and bounced against the surfaces many times. For this reason, a good fraction of the phonon energy ends up in the outer channel (Ch2). More detail about the relationship between the energy sharing between the channels is given in Appendix A.

Figure 7.4 shows the E_{Phonon} distribution for the sum of both channels. The top plot depicts the full range and the bottom plots are the zoomed-in version of the low-energy peak and the high-energy peak. The low-energy peak contains events where the electron-hole pair got recombined or absorbed by a detector surface immediately after the creation and no additional Luke phonons were created. On the other hand, the higher energy peak contains the events where the electron-hole pair went through the full Luke amplification, and the total phonon energy is the sum of the energy of the incoming photons and the Luke phonons. Comparing to the values expected from Equation 2.5 we note that both peaks have slightly less energy than expected because some of the phonons will not make it to the superconducting sensors. Similarly, we note the variation in the energy which is a measure of the resolution of the method. Finally, we point out that only $\sim \%74$ of the electron-hole pairs go through the full amplification.

The fraction of the time a photon creates an electron-hole pair that goes through the full Luke amplification depends on the distance of the photon hit from the top surface of the detector. When

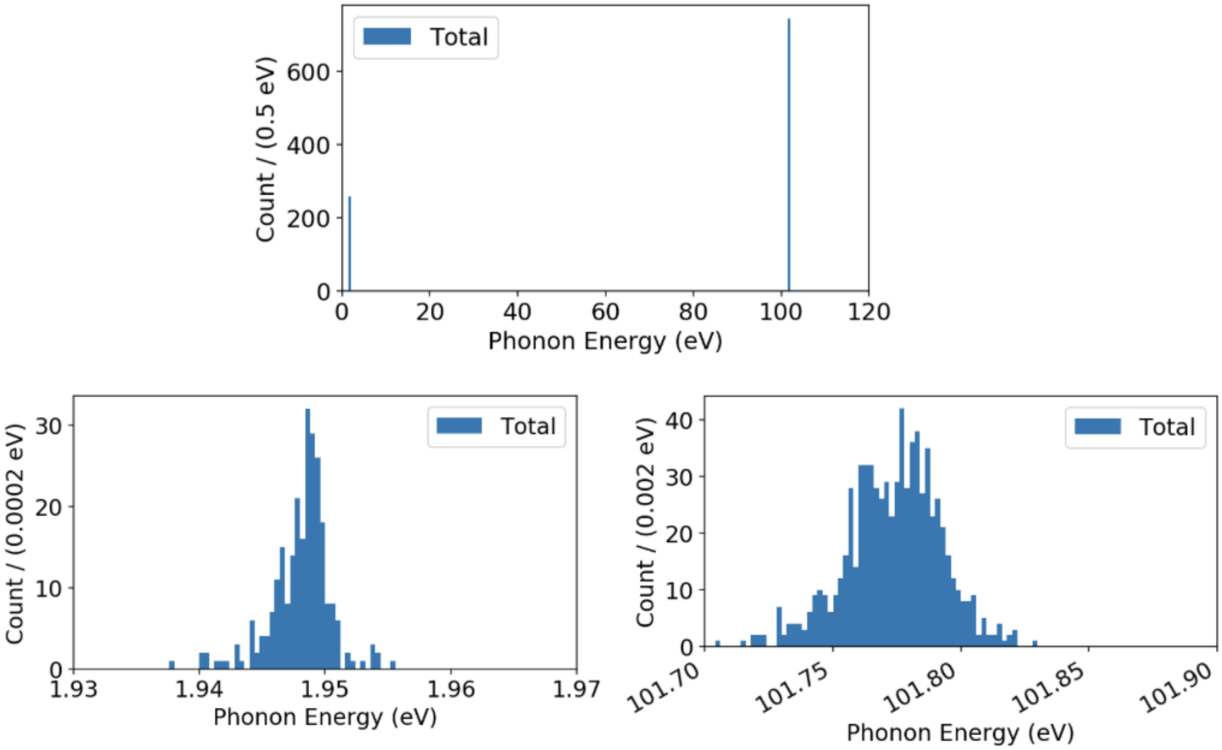

Figure 7.4: Three plots showing the distributions of the sum of the collected phonon energy, E_{Phonon}, from the two channels for the same sample. The top plot shows the full range while the bottom plots are zoomed-in to the low-energy and the high-energy peaks. The results are consistent with the expectations of Equation 2.5 modulo some phonon energy loss and resolution effects of the detector.

an incident photon hits the detector near the top surface, the liberated charges are more likely to be absorbed immediately by the detector surface. Consequently, the photon impact will not generate any Luke amplification. The top plot of Figure 7.5 depicts the distribution of the position of the direct energy deposits in the Z direction, for our sample, separated into fully amplified (red) and non-amplified (blue) events. The bottom plot shows the fraction of the time that there is full amplification, which we label the efficiency, as a function of the Z position. The probability of getting full amplification rises as the distance of the photon impact from the top surface of the detector increases and quickly becomes 100% by a hundredth of a mm.

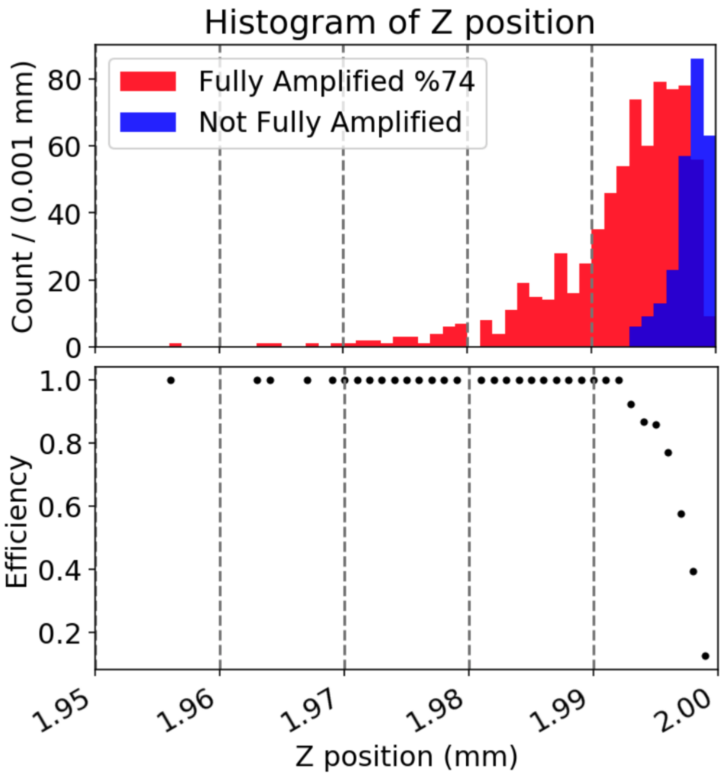

Figure 7.5: This figure shows two versions of the detector response as a function of the Z position of the photon interaction for the sample of events shown in Figures 7.1-7.4. While $\sim 74\%$ of all events get full amplification, the top plot shows the Z distribution of the events (Z = 2.00 mm is the top of the detector), where the events that are fully amplified are shown in red and those which are not are shown in blue. The bottom plot shows the efficiency of getting full amplification as a function of the distance from the top surface, Z. Most of the electron-hole pairs that are created very close to the top surface of the detector get absorbed and have a small probability of getting full Luke amplification.

7.2.2 Pulse Simulation Results: TES, DAQ, and Noise Simulation

In this section, we show the TES pulse results from the simulation of the sensors, the data acquisition system, and the electronic noise. We will also highlight the main effects that are simulated at each stage. Each will be important in the measurement of the signal that is the readout of the detector so we can use it for determining the amount of energy deposited by the optimal filter analysis as well as its contribution to the resolution of the energy measurement.

The energy and arrival times of the phonons absorbed by the QET in CrystalSim are fed into

TESSim which calculates the expected TES current as a function of time as described in Section 3.3 for each channel. Note that the output TESSim pulse is in μA and does not include the effects of the DAQ. Figure 7.6 displays the TESSim pulse for an example event as a function of time for both channels as well as a zoomed-in version with the two pulses superimposed.

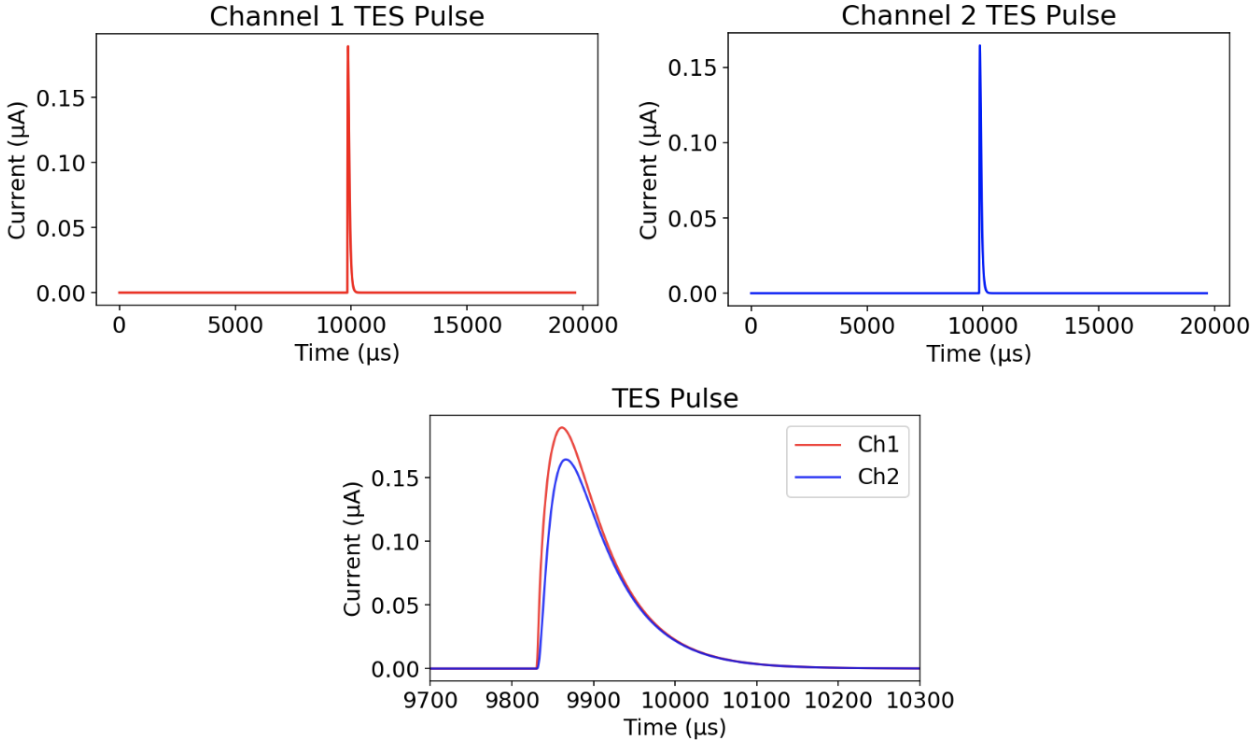

Figure 7.6: These plots show the simulated TES current (out of TESSim) for an example event as a function of time for Ch1 (top left), Ch2 (top right), and a zoomed-in version for both channels superimposed (bottom) for comparison.

The results of both TESSim channels are fed into DAQSim, which simulates both the data acquisition system as well as the noise. Figures 7.7 and 7.8 show the same pulses from Figure 7.6 after each has been processed by DAQSim with and without noise, respectively. A comparison between the TESSim pulse and the real data template taken from Figure 4.6 and scaled to the peak value of the TESSim pulse, is shown in Figure 7.9. As shown in the plots, there is a small but clear difference between the simulation and data at large times, which is because we have used the default parameter values in the simulation of the TES. On the other hand, as we will see in the next chapter, this provides only a small contribution to the resolution of the measurement so no effort was made to tune them for this study. We will come back to the E_{Phonon} distribution after adding charge trapping and impact ionization.

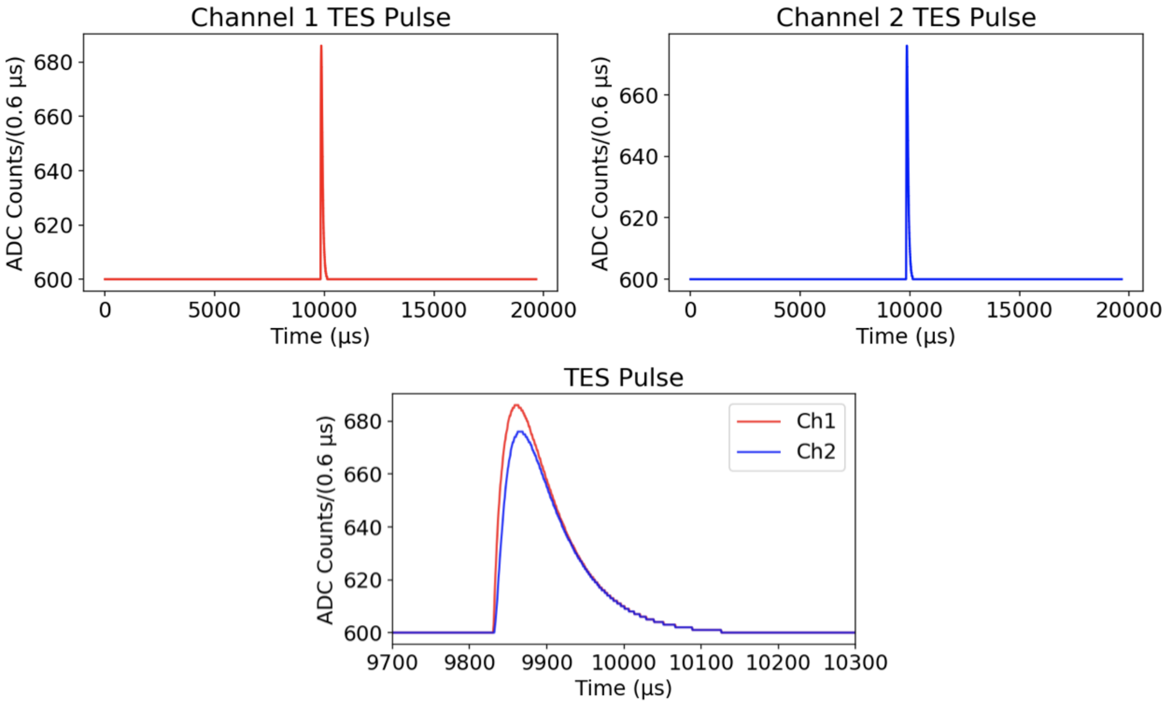

Figure 7.7: These plots show the same pulses as shown in Figure 7.6, but after the pulse has been processed by the DAQ simulation (DAQSim) which is responsible for the digitization of the pulses and conversion to Analog to Digital Converter (ADC) units. The digitization effect of DAQSim is most visible around Time=10100 μs in the bottom plot.

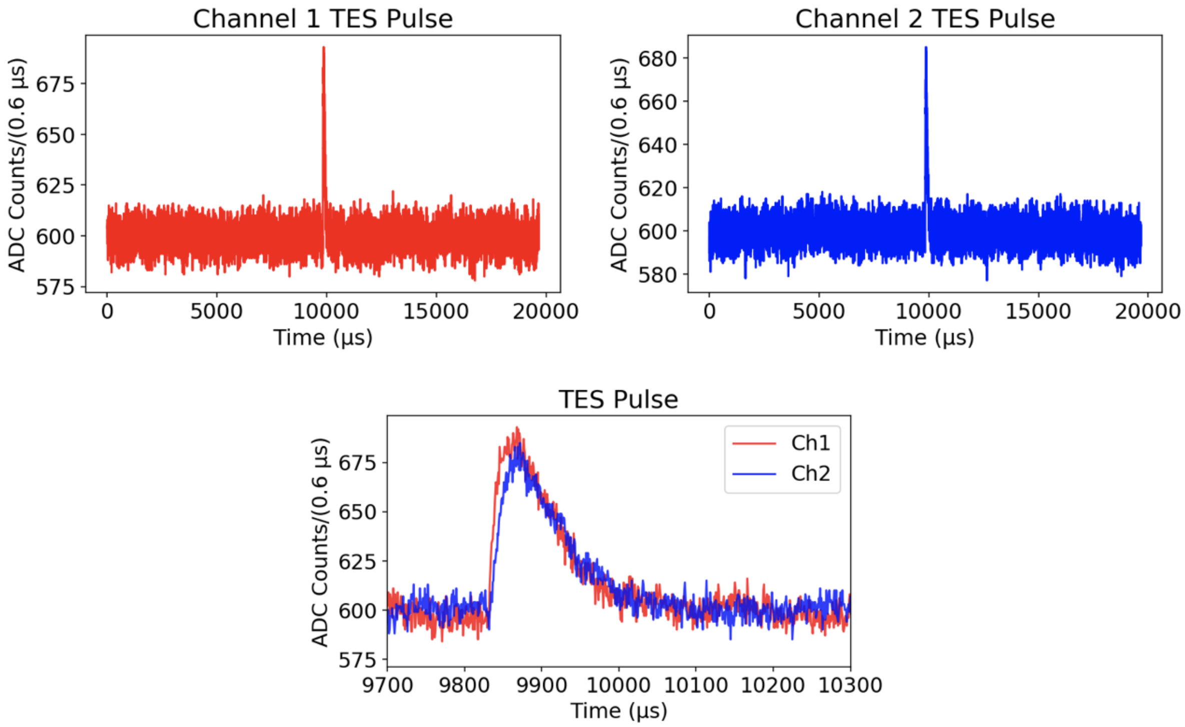

Figure 7.8: These plots show the same pulses as shown in Figure 7.7 but include the noise simulation (NoiseSim) which is added to the pulse before digitization.

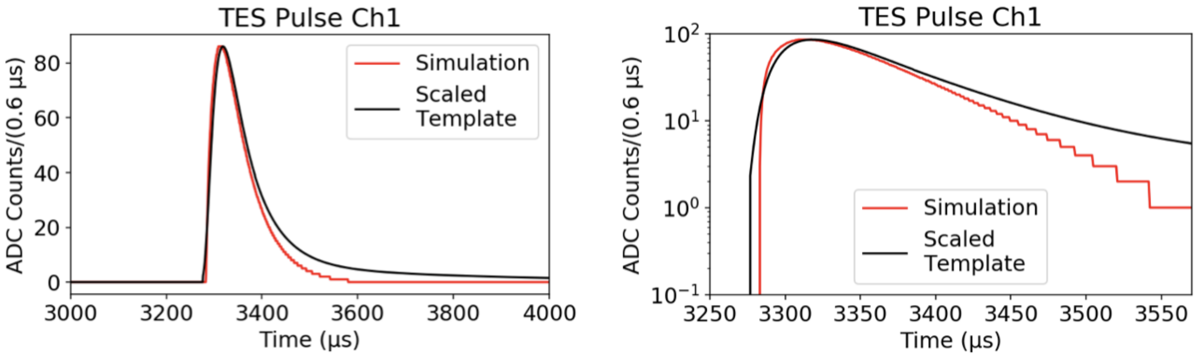

Figure 7.9: These plots show comparisons between an example fully simulated TES pulse and the real data template (scaled to the TES pulse) in linear (left) and log (right) scales. We note that there is good agreement for most of the pulse, but they diverge at the largest times.

7.3 Results After Adding Charge Trapping and Impact Ionization Effects

In this section, we study the impact of simulating the imperfections in the real crystal as described in Section 2.5. Figure 7.10 shows the E_{Phonon} distribution in three scenarios out of CrystalSim so we can measure the contribution from each effect. The cases are where we have (i) only charge trapping, (ii) only impact ionization, and (iii) both effects contributing to the simulation. As shown in the plots, when we add the simulation of the charge trapping, there are events with energies between the zeroth and first electron-hole pair peaks. This is because some otherwise fully-amplified electron-hole pairs will get trapped in the defects/impurities during their travel path and lose a portion of their Luke amplification. On the other hand, when we add the simulation of the impact ionization, we will get some events with energies higher than the first electron-hole pair peaks because some of the charges will ionize other charges in overcharged impurity regions and create more charges which can produce more Luke amplification. For the figure, we have set the charge trapping mean free path (CT MFP) to 260 mm, and the impact ionization mean free path (II MFP) to 2700 mm. Note that these values are chosen based on the results from a sample of events described in the next chapter.

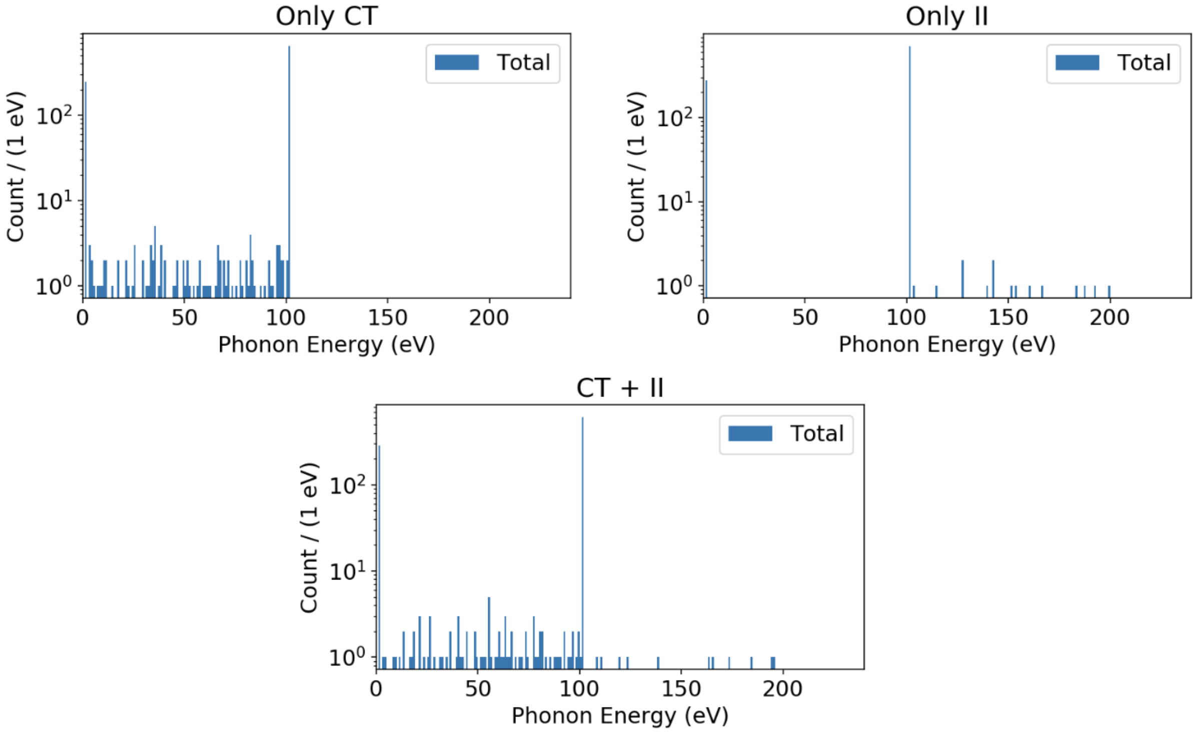

Figure 7.10: This figure shows the E_{Phonon} distribution out of the crystal simulation for samples of events with single-photon interactions in three different configurations: 1) charge trapping only (top left), 2) impact ionization only (top right), and 3) both (bottom). As described in Section 2.5 trapping will only create events with energies between the zeroth and first electron-hole pair peaks because the charge gets trapped and loses some of the Luke amplification. Impact ionization will only create events with energies higher than the first electron-hole pair peak because, in this case, an extra charge will be liberated and will produce extra Luke amplification. The charge trapping mean free path (CT MFP) is set to 260 mm and the impact ionization mean free path (II MFP) is set to 2700 mm. Note that these values are chosen based on the results for a Poisson laser that we will introduce in the next chapter.

7.4 Results After Adding Noise and Running the Simulated Data Through Reconstruction Software

In this section, we look at the results for our single-photon sample run through the full simulation chain. This includes all simulation effects turned on, running it through the reconstruction algorithm with a given threshold as well as the energy calibration (using the calibration methods described in Section 5.2). The results are shown in Figure 7.11. Note that compared to the bottom plot of Figure 7.10, there are two main changes in this plot: (i) the width of the first electron-hole pair peak is increased, because the simulation of electronic noise is included, and (ii) the low-energy events have been removed, because the reconstruction software has applied a trigger to the data (more on this in Section 8.4). We are now ready to look at multi-phonon events.

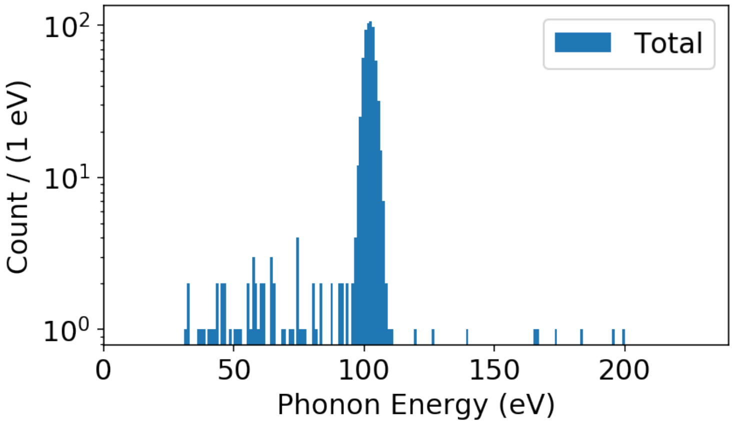

Figure 7.11: This figure shows the E_{Phonon} distribution for the same sample as the bottom plot in Figure 7.10 after TESSim, DAQSim and NoiseSim as well as running the data through the reconstruction software (CRP), and adding calibration. Note that the width of the peak is larger because of the effects of the electronic noise. Another important point worth mentioning is that the low-energy events are removed because of the trigger effect which is part of the reconstruction software.

8. Simulation Results for Multiple-Photon Interactions

In Chapter 7 we studied the simplified case of single-photon interactions with the detector using simulations. In reality, the laser shoots multiple photons to the detector at the same time so this needs to be taken into account in the simulations. In this chapter, we study multiple-photon interactions with the detector and present the simulation results. The simulation configuration for the data analyzed in this chapter is the same as Chapter 7 except for one major difference; the number of photons hitting the detector at the same time can be more than one, which is denoted in each plot.

In Section 8.1, we focus on the detector response to multiple-photon interactions. We first discuss the expected outcome for simplified cases and then present the simulation results. In Section 8.2, we show the results after adding charge trapping and impact ionization to the simulation. In Section 8.3, we add noise to the simulation and run the final simulation results through the reconstruction software. In Section 8.4, we focus on how the trigger affects the number of events in the final dataset as a function of energy. Finally, in Section 8.5 we study the different contributions to the resolution of the phonon energy measurement.

8.1 Detector Response

In this section, we discuss the detector response to the multiple-photon interactions. Before starting, we note that each of the electron recoils is not expected to affect each other in the crystal so no attempt is made to correlate their results in the simulation. We first discuss the expected value of the collected phonon energy, E_{Phonon}, in the crystal for two simplified cases: (i) when only one photon hits the center of the detector and (ii) when two photons hit the center of the detector at the same time. This helps us to develop an understanding of the expected outcomes when multiple photons hit the detector at the same time. With that in mind, we present the DetectorSim results for the multiple-photon interactions with no charge trapping or impact ionization. In Section 8.1.1, we show the E_{Phonon} distribution for different number of incident photons. In Section 8.1.2, we show the E_{Phonon} distribution for the case where the number of photons hitting the detector at the same time is no longer constant but follows a Poisson distribution with $\lambda = 1$.

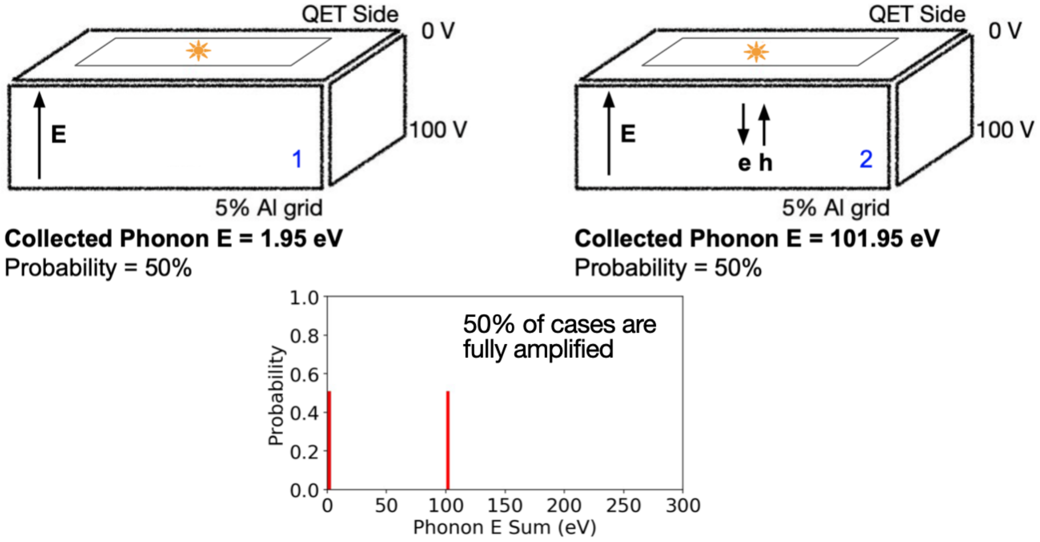
QET Side
0 V
E
1
100 V
5% Al grid
Collected Phonon E = 1.95 eV
Probability = 50%
QET Side
0 V
E
e h
2
100 V
5% Al grid
Collected Phonon E = 101.95 eV
Probability = 50%
50% of cases are fully amplified
Probability
1.0
0.8
0.6
0.4
0.2
0.0
0
50
100
150
200
250
300
Phonon E Sum (eV)

Figure 8.1: An illustration of the detector phonon energy readout for two simplified cases when a single photon interacts with the detector (shown as the box) at the point indicated with a yellow star. The top left shows the case where the electron-hole pair created by the photon immediately gets absorbed or recombined which means E_{Phonon} = 1.95 eV (the energy of the incident photon). The top right shows the case where the electron-hole pair goes through the full Luke amplification, in which case the detector will readout 1.95 eV from the incident photon energy plus the 100 eV from the Luke amplification. The bottom plot shows the expected E_{Phonon} distribution for the case where 50% of the photons are fully-amplified.

Figure 8.1 illustrates two simplified scenarios of the detector phonon energy readout when a single photon interacts with the detector. There are two possible outcomes: (i) The electron-hole pair created by the photon gets absorbed or recombined instantly. In this case, E_{Phonon} = 1.95 eV which is the energy of the incident photon (top left). (ii) The electron-hole pair undergoes the full Luke amplification, in which case the detector will read out 1.95 eV from incident photon energy in addition to the 100 eV from Luke amplification (top right). If we assume that for each photon, the probability of getting full amplification is 50%, the bottom plot represents the expected E_{Phonon} distribution.

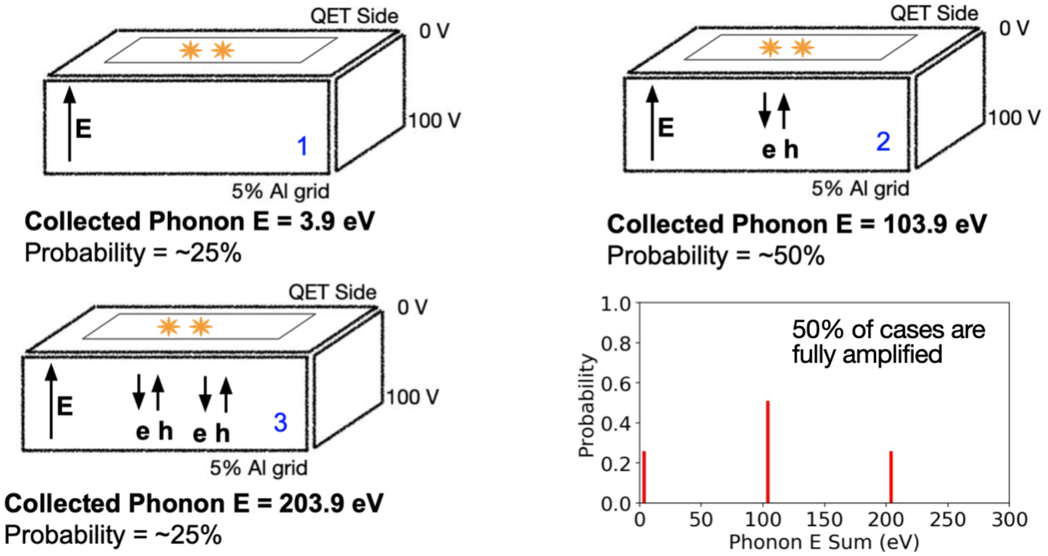
QET Side
0 V
100 V
E
1
5% Al grid
Collected Phonon E = 3.9 eV
Probability = ~25%
QET Side
0 V
100 V
E
e h
2
5% Al grid
Collected Phonon E = 103.9 eV
Probability = ~50%
QET Side
0 V
100 V
E
e h
e h
3
5% Al grid
Collected Phonon E = 203.9 eV
Probability = ~25%
50% of cases are fully amplified
Probability
1.0
0.8
0.6
0.4
0.2
0.0
0
50
100
150
200
250
300
Phonon E Sum (eV)

Figure 8.2: The same simplified scenario as in Figure 8.1, but with two incident photons at the same time at the points indicated with yellow stars. The top left shows the case where both electron-hole pairs created by the photon get recombined immediately, in which case the detector will readout 3.9 eV which is the combined energy of the incident photons. The top right shows the case where only one electron-hole pair goes through the full Luke amplification, in which case the detector will read out 3.9 eV from the incident photons plus the 100 eV from the Luke amplification. The bottom left shows the case where both electron-hole pairs go through the full Luke amplification, in which case the detector will read out 3.9 eV from the incident photons plus 200 eV from the Luke amplification. The bottom right plot shows the expected E_{Phonon} distribution for the case where 50% of the photons are fully-amplified.

Figure 8.2 depicts a scenario similar to that in Figure 8.1, but with two incident photons hitting the detector simultaneously. In this case, there are three possible outcomes: (i) Both electron-hole pairs created by the photons get absorbed or recombined immediately, yielding $E_{Phonon} = 3.9$ eV which is the energy of the incident photons (top left). (ii) Only one electron-hole pair undergoes the full Luke amplification, in which case, we get E_{Phonon} = 103.9 eV where 3.9 eV from the incident photons and 100 eV is from the Luke amplification. (iii) Both electron-hole pairs undergo the full amplification, which provide 3.9 eV from the incident photons, and 200 eV from the Luke amplification. Similar to Figure 8.1, the expected E_{Phonon} distribution is shown in the bottom plot assuming that for each photon the probability of getting full amplification is 50%.

8.1.1 Total Collected Phonon Energy in the Crystal as a Function of the Number of Incident Photons

With an understanding of the two simplified cases mentioned in the last section, we can now move on to the simulation results for the cases where one or more photons hit the detector at the same time. Figure 8.3 depicts a series of plots that show the E_{Phonon} distribution for various numbers of incident photons. The number of photons hitting the detector simultaneously is denoted by the letter N. As shown in the previous chapter the simulations estimate that in reality, each photon has a $\sim 74\%$ chance of creating an electron-hole pair that goes through the full amplification. As the number of photons hitting the detector at the same time increases, the number of possible outcomes increases. For example, when we simulate a sample with $N = 3$, we will see four peaks in our simulation results because there are four possible outcomes for the amount of Luke amplification, it can be 0 eV, 100 eV, 200 eV, or 300 eV which corresponds to the number of the electron-hole pairs that go through the full Luke amplification as described in Equation 2.6.

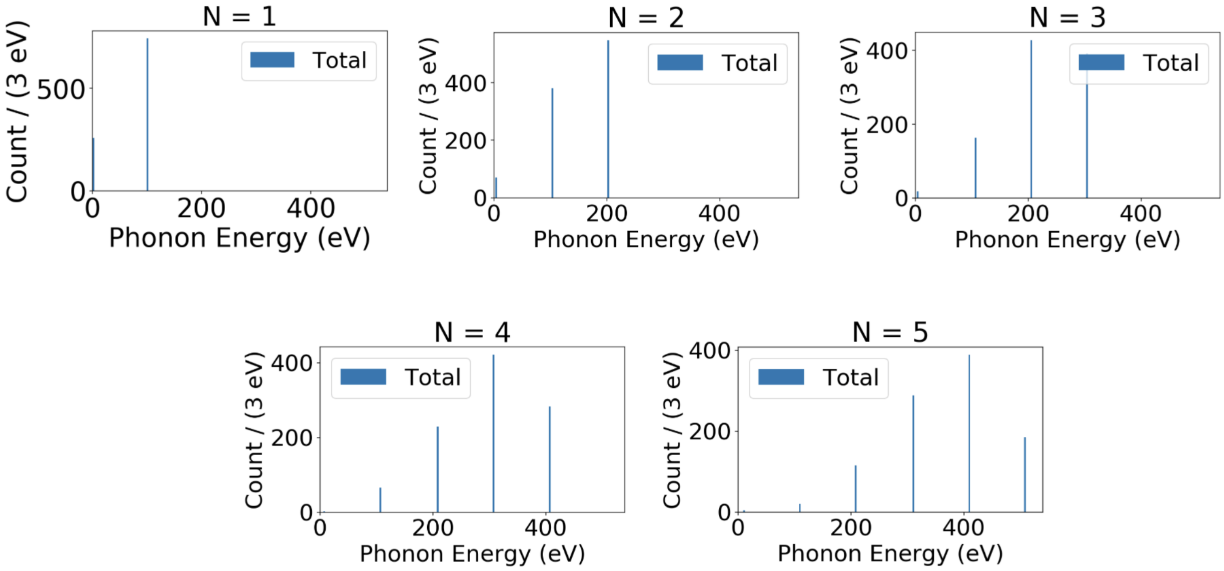

Figure 8.3: A set of plots showing the E_{Phonon} distribution directly out of the full crystal simulation, for a different number of incident photons, labeled with N, each of which has an $\sim$75% chance of getting full amplification. As N increases, the number of possible outcomes increases as expected.

8.1.2 Example Results for a Laser that Emits Photons According to a Poisson Distribution

As shown previously in Figure 5.5, the number of photons emitted from a laser at the same time follows a near-Poisson distribution. For this reason, we start by configuring SourceSim with a Poisson distribution of the number of simulated photon hits and fix it later.

The top plot of Figure 8.4 displays the E_{Phonon} distribution from CrystalSim for a set of photons produced by a laser which emits photons according to a Poisson distribution with $\lambda = 1$. The bottom plots are zoomed-in versions for individual peaks. The fluctuation in the number of the electron-hole pairs that undergo full Luke amplification, M, is what causes the large peaks in the top plot. The fluctuation in the number of photons, N, is what causes the minor peaks in the bottom four panels. Following Equation 2.5, we can create a better version of Equation 2.6 where E_{Phonon} can be calculated based on the number of the electron-hole pairs that went through the

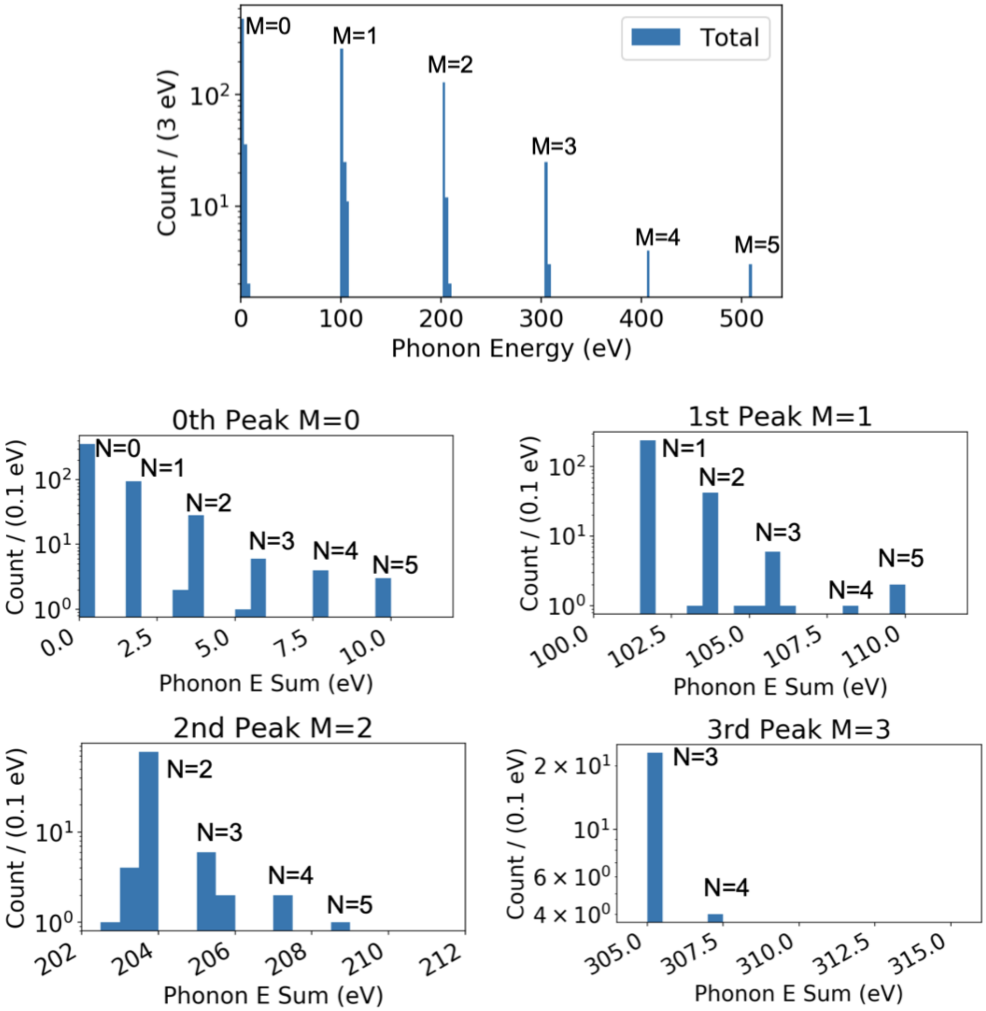

Figure 8.4: This figure shows the E_{Phonon} distribution for a set of photons emitted with a laser for which the number of emitted photons follows a Poisson distribution with $\lambda = 1$ (Poisson laser) (top) and zoomed-in histograms for individual peaks (bottom). The large peaks in the top plot are caused by the variation in the number of electron-hole pairs that went through the full amplification, M. The small peaks in the bottom four plots are caused by the variation in the number of incident photons, N.

full amplification and the number of photons that hit the detector via:

$$E_{Phonon} = 100 \cdot M + 1.95 \cdot N, \tag{8.1}$$

where M is always smaller than or equal to N.

The top plot in Figure 8.4 and Equation 8.1, both illustrate why we have the peaks in the data, but also show that the contributions to each, including the RMS of the distribution, is more complicated than the simple assumption that it represents the number of photons from the laser. On the other hand, we see describing them as being the number of fully-amplified electron-hole pairs is a good approximation since the contributions from multiple values of N are small and do not affect our calibration procedure substantially.

8.2 Results After Adding Charge Trapping and Impact Ionization Effects

In this section, which follows the same format as Chapter 7, we examine the effects of adding the simulation of impurities/defects in the crystal. Figure 8.5 shows the E_{Phonon} distribution after adding charge trapping and impact ionization to the simulation for a Poisson laser. For now, we note that the charge trapping mean free path (CT MFP) is set to 260 mm and the impact ionization mean free path (II MFP) is set to 2700 mm. These values are derived by comparing the simulation data for different values of the parameters to the real data and determining the final value for a Poisson laser. This process is described later, in Section 9.3.3.

8.3 Results after Adding Noise and Running the Simulated Data Through Reconstruction Software

In this section, we include the simulation of the TES, the DAQ, and the electronic noise in our sample and run it through the reconstruction algorithm which includes the trigger threshold. The results are shown in Figure 8.6, and there are two main differences from Figure 8.5. The first is that adding simulated noise to the simulated TES pulses increases the width of the peaks. The second is that the low-energy events have been eliminated from the plot, as they are not recognized as events by the trigger because their energy is below the threshold. Note that the trigger threshold in

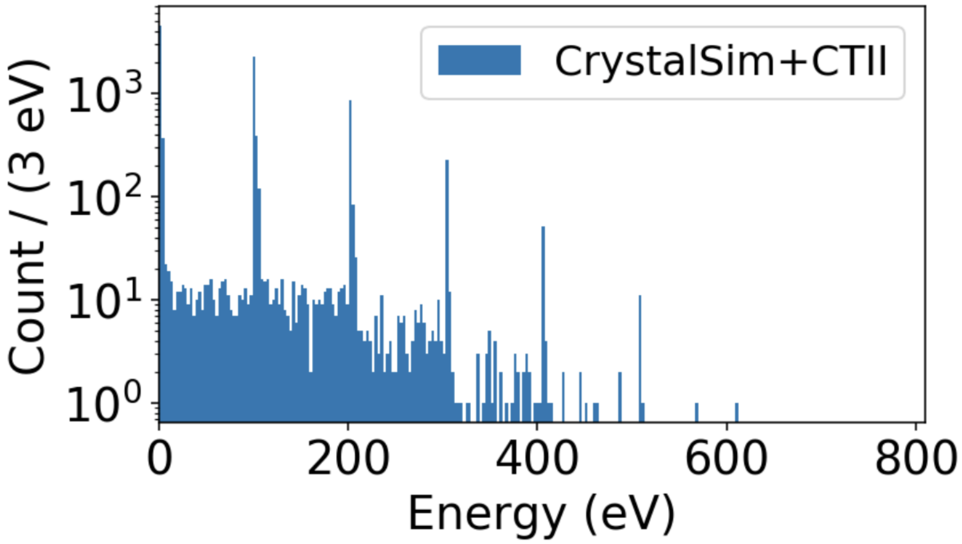

Figure 8.5: This figure shows the E_{Phonon} distribution using the Poisson laser model after adding charge trapping and impact ionization to the simulation. The charge trapping mean free path (CT MFP) is set to 260 mm and the impact ionization mean free path (II MFP) is set to 2700 mm for reasons described in the next chapter.

the reconstruction, as well as the calibration procedures, assumes the results described in the next chapter.

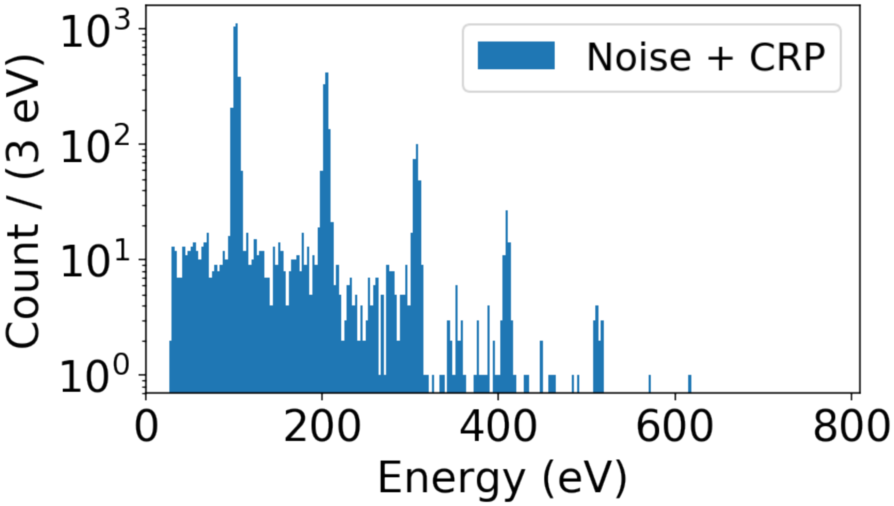

Figure 8.6: This figure shows the same results as Figure 8.5 but for the case where we have added the TESSim, DAQSim, and NoiseSim portions of the simulation and run the data through the reconstruction software, and calibration procedures. Note that the low-energy events do not contribute because the events with energy less than the threshold are not identified as events by the trigger. We also see that noise contributes to the width of the peaks (resolution).

8.4 The Trigger Response as a Function of Energy

In this section, we describe the effect of the trigger as a function of E_{Phonon}. For doing so, we run the simulated sample previously shown in Figure 8.6 through the reconstruction algorithm with two different thresholds so we can see the difference between them, in particular which events are removed at the higher threshold. For simplicity, we have set the thresholds at 40 ADC and 50 ADC with the results shown on the left-hand side of Figure 8.7. Since all events above 25 eV pass the lower energy threshold we can look to see what fraction passes the higher threshold as a function of energy. The right-hand side of Figure 8.7 shows this fraction, which is referred to as the trigger efficiency. Setting the threshold such that it reproduces the turn-on curve of Figure 1.9 allows us to determine the final trigger threshold for the simulations, which we will do in the next chapter.

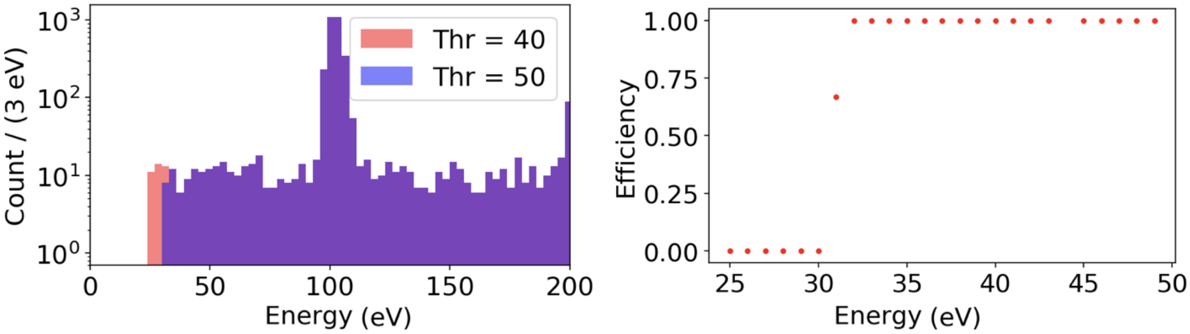

Figure 8.7: This figure shows the effect of the trigger threshold on the data. The plot on the left shows the calibrated E_{Phonon} distribution out of the reconstruction software with a low and high trigger threshold requirement on A_{OF}. The ratio of the two distributions illustrates which events are removed by the trigger, and is known as an efficiency curve. The removal of all events below a threshold follows the typical trigger turn-on curve shape [20].

8.5 Contributions to the Energy Measurement Resolution

We next turn to the resolution of our energy measurements. In Section 5.4, our simplified model described the RMS of the peaks as the resolution of the energy measurement and a resolution of 3% of the electron-hole pair peak energy showed qualitative agreement. One major advantage of using simulations is that we can access otherwise-inaccessible information to enhance our understanding of the detectors. As we have seen in Figures 7.4, 7.10, 7.11, and 8.4 there are a number of contributors to the full RMS of the peaks in the data. To quantify the contributions of each of these effects we can simulate samples with different configurations and then study the results of each stage of the simulation to disentangle the contribution of each. While we will see that the RMS of each peak increased as a function of the energy in the data, we will focus on the contribution to the RMS of the first electron-hole pair peak. In this section, we calculate the contribution of different effects to the RMS in the data assuming that the resolution due to each effect is uncorrelated, Gaussian, and can be determined by taking their contributions in quadrature. We consider effects from CrystalSim, TESSim, Continous Readout Processing (CRP), noise, multiple photons, charge trapping, and impact ionization.

We start with studying the contributions of CrystalSim, multiple photons, charge trapping, and impact ionization. For doing so, we simulate three samples where (i) only one photon hits the detector at a time ($N = 1$), (ii) the number of photons hitting the detector at the same time follows a Poisson distribution ($\lambda = 1$) and (iii) the same as sample (ii) but with the addition of charge trapping and impact ionization. Figure 8.8 shows the E_{Phonon} distribution for all three samples, which confirms that adding each increases the RMS of the peaks. To measure the RMS of the energy distribution we consider the events between 95 eV and 110 eV and summarize the results in Table 8.1.

We continue our resolution study by running each of the three samples through the next steps of the simulations including TESSim, CRP, and NoiseSim. Figure 8.9 shows the E_{Phonon} distribution for the three samples after running each through the full simulation infrastructure. Note that the left plot does not include NoiseSim while the right plot does. Comparing the left and right plots, it

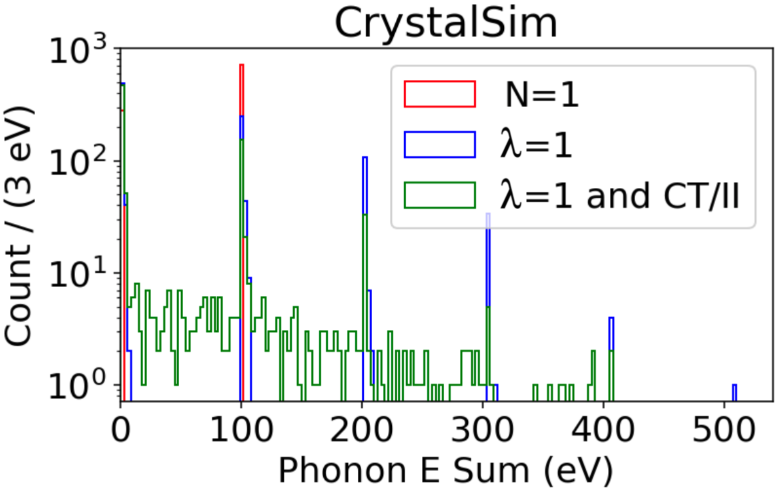

Figure 8.8: The E_{Phonon} distribution from CrystalSim for different simulation configurations to determine the various contributions to the width of the first electron-hole pair peak. The distribution in red shows the results for a sample of events where only a single photon interacts with the detector ($N = 1$). The distribution in blue is when the number of photons hitting the detectors follows a Poisson distribution with $\lambda = 1$. The distribution in green has the same simulation configuration as blue except charge trapping and impact ionization effects are turned on in the simulations. This shows that having a Poisson laser and impurities both contribute to the width of the peaks.

is evident that adding noise increases the RMS of the peaks as expected. Zoomed-in versions are shown in Figure 8.10 with the RMS measurement values summarized in Table 8.1.

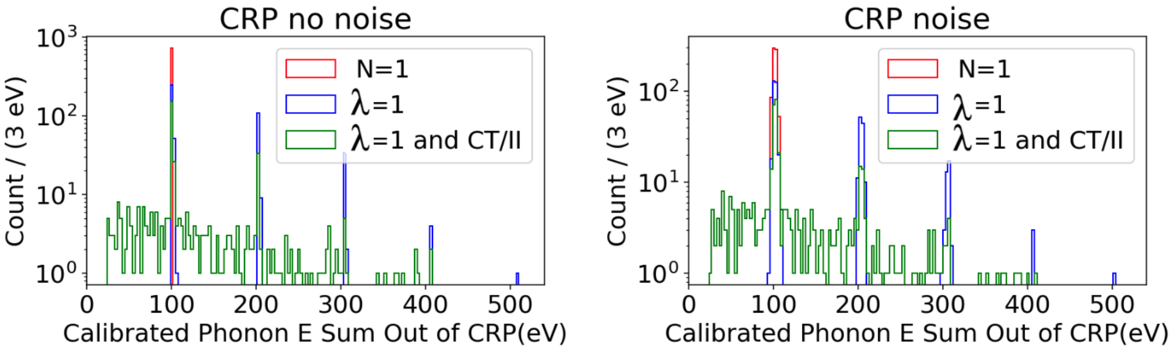

Figure 8.9: This figure shows the same results as Figure 8.8 but after running the simulated data through the reconstruction algorithm and after calibration, both without noise (left) and with noise (right) which shows that adding noise widens the width of the peaks.

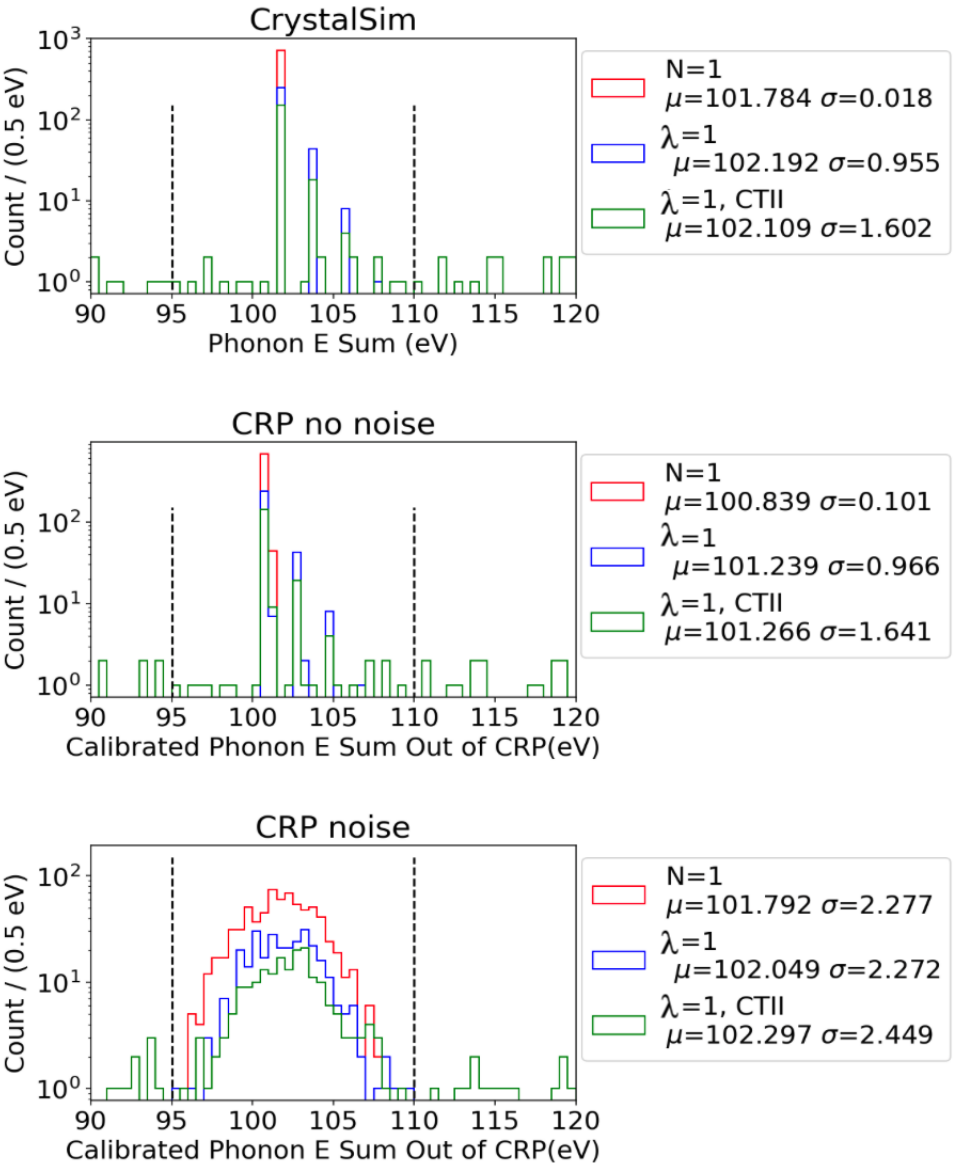

Figure 8.10: Zoomed-in versions of Figures 8.8 and 8.9 which shows the E_{Phonon} distributions for different stages and configurations of the simulation along with the mean and RMS for the 1st electron-hole pair peak. Note that RMS is calculated for the data between 95 eV and 110 eV, indicated with the vertical dashed lines. We can calculate the RMS due to different effects using the width of the peak in the different configurations.

With the simplifying assumption that none of the effects are correlated, we can estimate the contribution of each effect by calculating the differences of the results from Table 8.1 in quadrature. For example, to measure the contribution due to the multiple photons, we calculate the in-quadrature difference between the CrystalSim resolution of the $\lambda = 1$ and the $N = 1$ samples which are 0.955 eV and 0.018 eV, respectively. The results are summarized in Table 8.2, which shows the contribution from each effect to the RMS. The main contribution comes from noise. The following two largest contributions are from CT/II and multiple photons.

As seen in Figures 8.8 and 8.9, the RMS of the peaks is larger for the higher energy peaks. Thus, the quantitative results in Table 8.2 are only applicable for that case for the $M = 1$ case. For example, there is no contribution to the RMS from the zeroth electron-hole peak from II in the $M = 1$ estimate. Looking forward to the final simulation we expect that the contribution to resolution due to noise will remain constant. On the other hand we expect the contribution for CT and II and to play a larger role. A full quantification at higher energies will depend on the number of photons from the laser. With an estimate of the contributions to the RMS of the distributions, we move to a full comparison of the simulation and data in the next chapter.

	RMS of the First Peak (eV)		
Sample	**N = 1**	$\boldsymbol{\lambda = 1}$	$\boldsymbol{\lambda = 1}$ **and CT/II**
CrystalSim	0.018	0.955	1.602
+TESSim	0.019	0.954	1.321
+CRP	0.101	0.966	1.641
+Noise	2.277	2.272	2.449

Table 8.1: This table shows the measured RMS of the phonon energy distributions for the set of events with 95 eV < E_{Phonon} < 110 eV after adding each effect to the simulation for three different simulation configurations including (i) $N = 1$, where only a single photon interacts with the detector, (ii) $\lambda = 1$, where the number of photons hitting the detector at the same time follows a Poisson distribution and (iii) same sample except charge trapping and impact ionization are turned on in the simulations. Each is repeated with the addition running through the reconstruction, with and without noise. If we assume that the resolution due to each effect adds in quadrature, then we can calculate the contribution of each effect. The results are listed in Table 8.2.

Effect	**Contribution to the RMS of the First Peak (eV)**
CrystalSim	0.018
TESSim	0.006
CRP	0.099
Noise	2.274
Multiple Photons	0.955
CT/II	1.286
Total	2.783

Table 8.2: This table shows the contribution from each effect to the resolution. The values are calculated by taking the quadrature difference for different effects in Table 8.1. Noise has the biggest contribution to the resolution. The next two biggest contributions are from CT/II and multiple photons, respectively.

9. Comparison of the HVeV Laser Data to the Simulation

Having shown the simulation results for the Poisson laser simulation and mentioning the final values of the parameters, in this chapter we show how each is determined and do final comparisons. We note at the outset that since this is an iterative and approximative process we will not show all the steps along the way, but rather describe the methods and show that they are reasonable final values.

In Section 9.1, we present an overview of the simulation parameters and additional tools used for reproducing the HVeV laser spectrum and list the final values for all parameters. In Section 9.2, we assume some of the final parameter results for a first comparison of the data with the Poisson laser simulation and then we explain how to build a custom laser simulation. In Section 9.3, we explain how to determine final parameter values. In Section 9.4, we present the final data and simulation comparison. Finally, we end this chapter with a summary in Section 9.5.

9.1 Overview of Simulation Parameters and Additional Tools Used for Reproducing the HVeV Laser Spectrum

In this section, we overview the simulation parameters and additional tools used for reproducing the HVeV laser spectrum. Since our goal is to understand the detector, comparing the simulation data results as we tune the various parameters gives insight about the various effects modeled. We start with describing the different parameters that we need to determine in the simulation and discuss which regions of the data are used to set each.

Figure 9.1 shows the number of events as a function of reconstructed energy for the HVeV laser experiment along with the data regions used for determining the final simulation parameter values. We first present a quick overview of the parameters here and note that the final values for each are listed in Table 9.1. We will describe in detail how we determined each parameter in Section 9.3.

- Laser Description: The number of events in each peak is determined by a combination of the original distribution of the number of photons hitting the detector at the same time as well

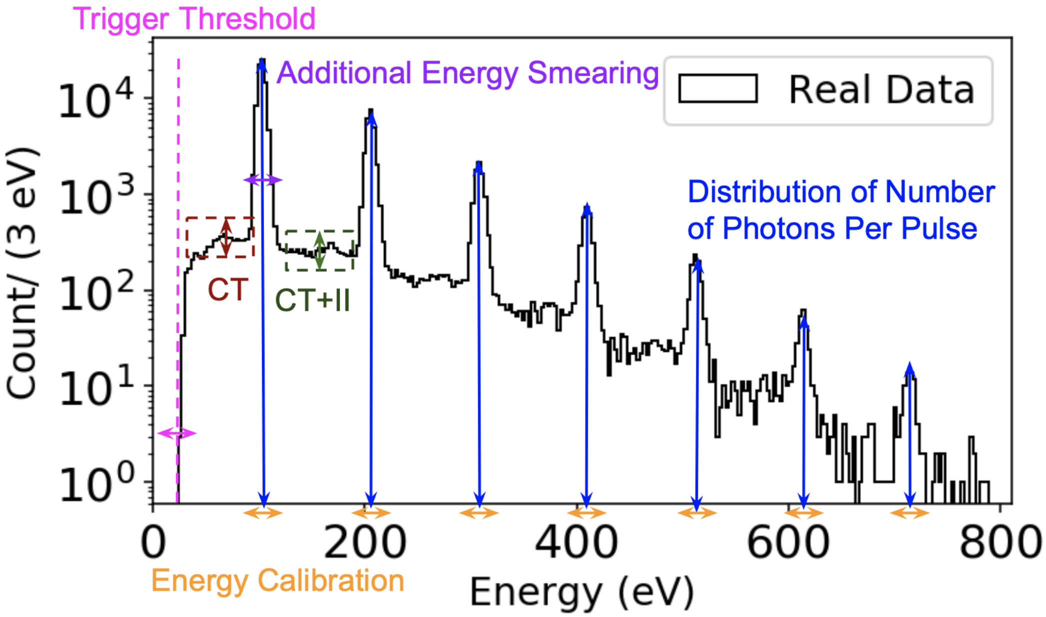

Figure 9.1: The number of events in the HVeV laser experiment as a function of reconstructed energy as well as indicators that show which regions are used to measure a number of our simulation parameters. These include the trigger threshold region to determine the OF amplitude minimum value for the processing, the CT and CT+II region used to determine the CT MFP and II MFP parameter values, the energy calibration regions used to determine the calibration constants, and the additional energy smearing needed. Also shown are arrows to indicate the maximum number of events in each peak to determine the number of photons to simulate in our laser model.

as the penetration depth and the rate at which recombination of electron and hole occur near the top surface of the detector.

- Trigger Threshold: In the processing of the data, the optimal filter returns a value of the amplitude A_{OF}. The threshold of the trigger requires that all events have $A_{OF} > A_{OF}^{Trigger}$.
- Crystal Impurity Parameters: The level of impurities in the crystal is parameterized by the mean free path of the charge trapping and impact ionization mechanisms.
- Energy Calibration Constants: The relationship between the energy measurements out of the DAQ and processed by the optimal filter needs to be corrected back to the expected total phonon energy using the same methods as the data using Equation 5.1.
- Additional Energy Smearing Constants: The RMS of the peaks have contributions from

many of the above effects, but in total, they do not reproduce the full width. Additional energy smearing is needed to provide the best fit of the data.

While an iterative process is used to find the final values of each of the free parameters, we start by showing the results for simulation in the case of the Poisson laser, as was shown in the previous chapter. Then, instead of showing all of the iterations, we typically use all but one of the final values and walk through the process of finding them one at a time as a way of illustrating our choices for the values and how well each works. We note that there are 17 parameters listed in Table 9.1, some of which are easy to change in the tuning, while others require significant re-running of the entire simulation process. For this reason we have not finely tuned each of the parameters, but rather stopped when they were close enough by eye. We will consider the χ^2 agreements, but note that none of them have been fully minimized. For example, with further tuning we can get a better match between the data and the simulation for the number of photons per pulse, especially for $N = 1$.

<table>
<tr><th colspan="2">Laser Description</th><th colspan="2">Trigger Threshold</th></tr>
<tr><td>N of Photons Per Pulse</td><td>Number of Events</td><td>A_{OF}^{min}</td><td>48 ADC</td></tr>
<tr><td>1</td><td>67171</td><td colspan="2">Crystal Impurity Parameters</td></tr>
<tr><td>2</td><td>39062</td><td>CT MFP</td><td>265 mm</td></tr>
<tr><td>3</td><td>17559</td><td>II MFP</td><td>2700 mm</td></tr>
<tr><td>4</td><td>8942</td><td colspan="2">Energy Calibration Constants</td></tr>
<tr><td>5</td><td>2901</td><td>a</td><td>601</td></tr>
<tr><td>6</td><td>2659</td><td>b</td><td>0.115</td></tr>
<tr><td>7</td><td>300</td><td colspan="2">Additional Energy Smearing Constants</td></tr>
<tr><td>8</td><td>150</td><td>a</td><td>0.0016</td></tr>
<tr><td>9</td><td>50</td><td>b</td><td>2.36</td></tr>
<tr><td>10</td><td>20</td><td></td><td></td></tr>
</table>

Table 9.1: This table shows a summary of all tunable parameters along with the final values to produce the simulated phonon energy distribution shown in Figure 9.12. Note that the functions used for energy calibration and additional energy smearing are $E_{Phonon} = a \cdot A_{OF} \cdot (1 + b \cdot A_{OF})$, and *Additional Energy Smearing* = $(a \cdot E_{phonon} + b)$, respectively.

9.2 First Comparison of Data and Simulation and Moving to a Custom Laser Model

In this section, we do a first comparison to the data with the Poisson laser simulation and describe the process of moving to a custom laser simulation. We start by showing the results of from Chapter 8 (Figure 8.6) along with the real data. We see that the Poisson laser is effective in reproducing the data distribution at low energies, but not high energies, so a more sophisticated model is required. Then we describe how we build a custom laser with a configurable number of photons hitting the detector at the same time. This will make us well set up for tuning the rest of the parameters.

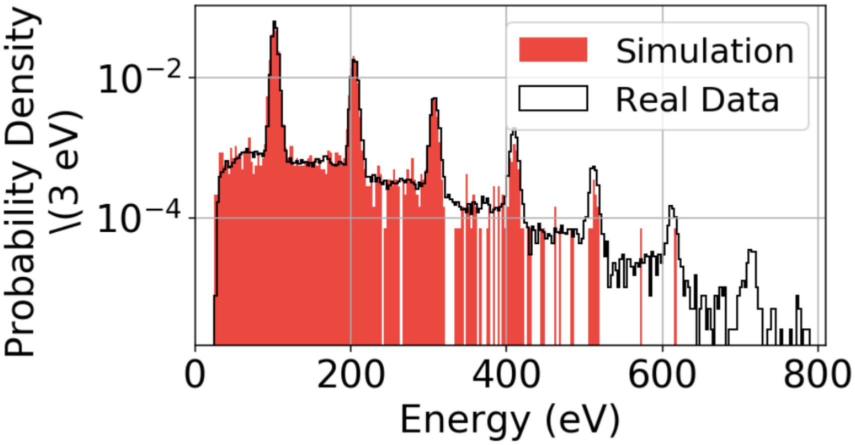

Figure 9.2: A comparison between the measured phonon energy spectrum from the real data and the full simulation using the final parameter simulations except for the use of the Poisson laser model with $\lambda = 1$ and CT MFP which is 260 mm here. This plot shows that a Poisson laser, originally shown in Figure 8.6, does not describe the data well at energies higher than about 300 eV.

Figure 9.2 shows a comparison between the measured phonon energy distribution from the real data and the full simulation of a Poisson laser using the rest of the final parameter values in Table 9.1 except CT MFP which is 260 mm here. As seen in the figure, there is a good agreement with the data only in energies lower than 300 eV. Although we knew this from Section 5.4, where we used a toy model, it is a useful starting point for tuning the parameters. In particular, using the

Poisson laser simulation, we get a good initial estimate for charge trapping and impact ionization mean free path values (CT MFP = 260 mm and II MFP = 2700 mm) using the methods described in Section 9.3.3 and will refine it later.

We next move on to building a custom laser in which we can set the number of photons per pulse to reproduce the number of events in the peaks in the real data more closely. The process is to simulate ten different samples where the number of photons hitting the detector at the same time, N, is set to 1 through 10. This automatically takes into account the Z distribution of the photon interactions, the probability of Luke amplification as a function of Z, and the first estimate of CT MFP and II MFP. Ultimately, each sample is combined with a configurable weight as part of our iterative process. Figure 9.3 shows the distribution for the ten samples.

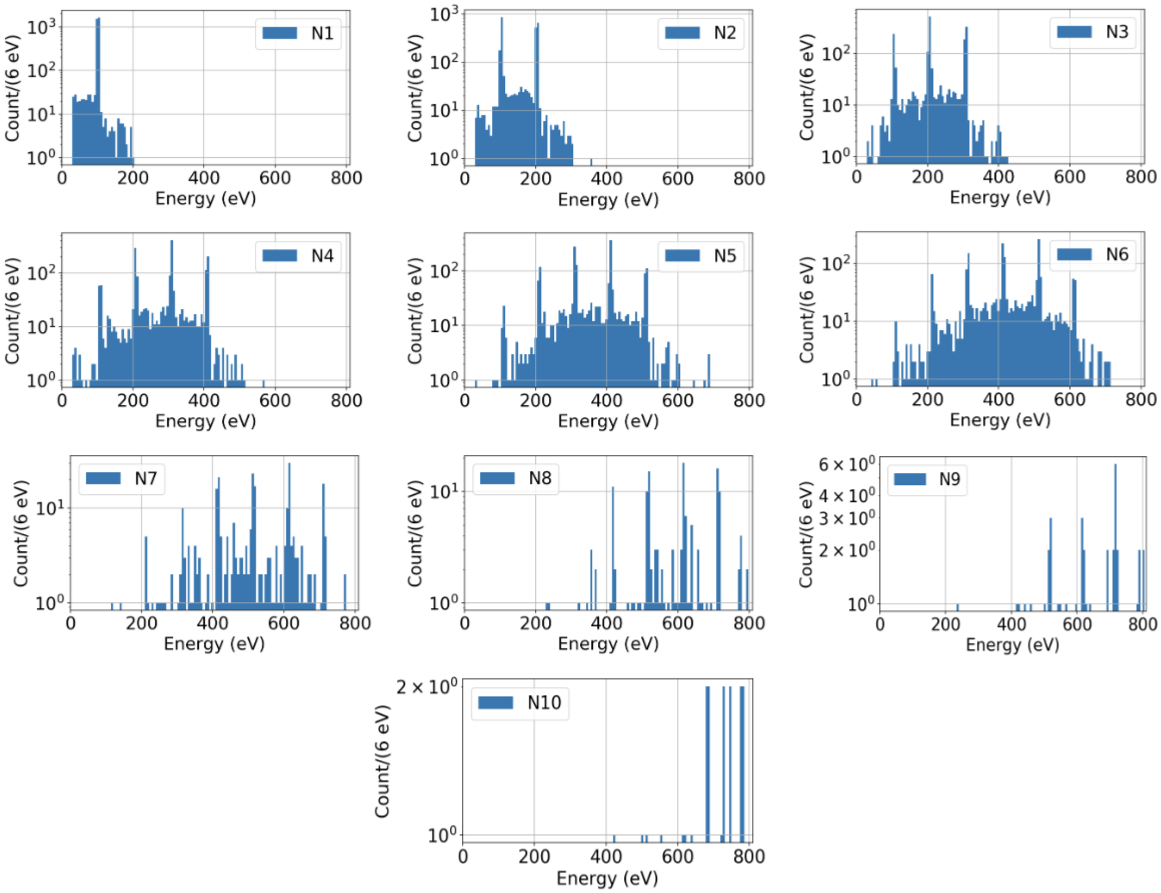

Figure 9.3: This figure contains the E_{Phonon} distributions for the ten different simulation samples, each with a value of the number of photons per laser pulse from $N = 1$ to $N = 10$. We simulate a custom laser by combining these samples and applying weights to them. We note that there are different numbers of events for each sample.

9.3 Describing How we Determined the Final Parameter Values

In this section, we focus on describing how we found the final values for the simulation parameters outlined in Section 9.1.

9.3.1 Weights for Combining Samples

The process for determining the number of photons per pulse is done semi-systematically as we iterate and regenerate samples of events over all the parameters. The results, with all-but-the energy smearing, is shown in Figure 9.4 along with the data. We see a good match except for the RMS of the peaks as expected.

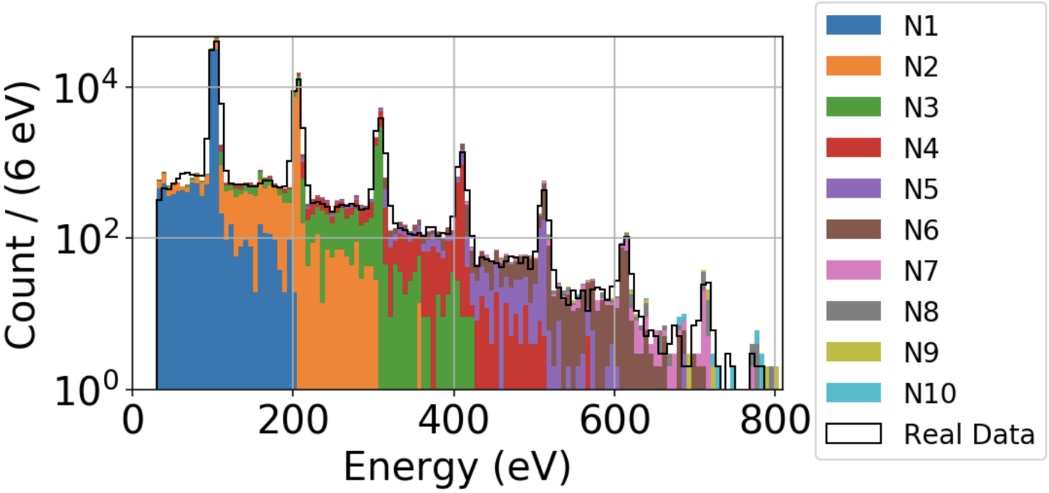

Figure 9.4: This figure shows the data along with the results of the combined simulation samples created with the ten samples shown in Figure 9.3 after applying weights and the final parameter values of Table 9.1 except for the additional energy smearing. It shows good agreement except for the RMS of the peaks as expected.

9.3.2 Trigger Threshold

In this section, we describe how the trigger threshold is determined. As a reminder, the trigger threshold is applied to both simulation and data in the reconstruction step (also known as continuous readout processing or CRP [14]). Figure 9.5 shows the energy distribution for the data and the simulation for the events below the second electron-hole pair peak for three different possible trigger thresholds, A_{OF}^{min}, using all the final values of the simulation with the Poisson laser model for simplicity. As shown in the figure the $A_{OF}^{min} = 48$ ADC result shows the best visual agreement between the data and simulation turn-on curves, so we use this value in our analysis.

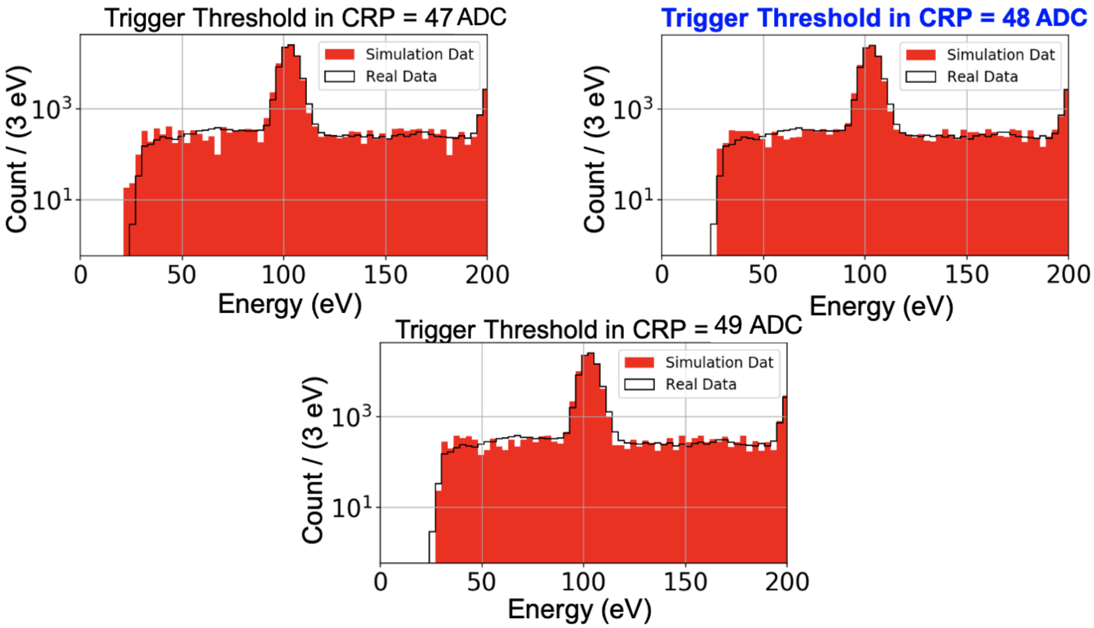

Figure 9.5: Three versions of the energy distribution below the second peak for the data (shown in the black curve) and the simulation with three different trigger thresholds for use in determining the trigger threshold. Note that the simulation is done with the Poisson laser distribution for simplicity, but the final values of the CT MFP and II MFP are used and additional energy smearing is applied to the simulation data (described in Section 9.3.5). Comparing the results by eye, we chose $A_{OF}^{min} =$ 48 ADC because it produces the best match between data and simulation turn-on curves.

9.3.3 Charge Trapping and Impact Ionization Mean Free Path

In this section, we describe how we determined the final values for the charge trapping and impact ionization mean free path values. In Section 5.4, we learned that we can determine the values for charge trapping and impact ionization one-by-one because only charge trapping contributes to the background below the first electron-hole pair peak. Here, we first explain how we use the data from three regions to measure the CT MFP and II MFP parameter values and then determine the parameters.

The values of the CT MFP and II MFP are determined using the ratio of the number of events in three regions of the data. As shown in Figure 9.6 and described in Table 9.2 we consider: (i) R1: the background before the first electron-hole pair peak, (ii) R2: the first electron-hole pair peak, and (iii) R3: the background between the first and the second electron-hole pair peaks. To quantitatively assess the agreement, we define two parameters: (i) R1/2, which is the ratio of the number of events below the first peak to the number in the first peak, and (ii) R3/2, which is the ratio of the number of events between the first and second peaks to the number in the first peak.

While the first determination of the mean free path parameters was done with the Poisson laser simulation and gave final values of CT MFP=260 mm and II MFP = 2700 mm as shown in Figure 9.2, we next move to do it again with the custom laser. To determine the CT MFP value, we simulate four samples with different values of the CT MFP while the II MFP is set to infinity, and then compare the R1/2 values between the data and simulation. The simulated distributions and the data are shown in Figure 9.6. Figure 9.7 shows the value of R1/2 for the four simulated values of the CT MFP. The R1/2 value for the data is marked with a solid black line. As shown in these figures, CT MFP = 265 mm produces the best match between the simulation and data so we fix the value of CT and then move to determine the value of the II MFP.

While we do not show the full set of points for the II MFP determination, Figure 9.8 and Table 9.2, show the agreement between the data and the simulation for the final CT MFP and II MFP values. The best agreement again comes from II MFP = 2700 mm, and the bottom left shows that there is no need to re-tune the final CT MFP. We will come back to how well these parameters

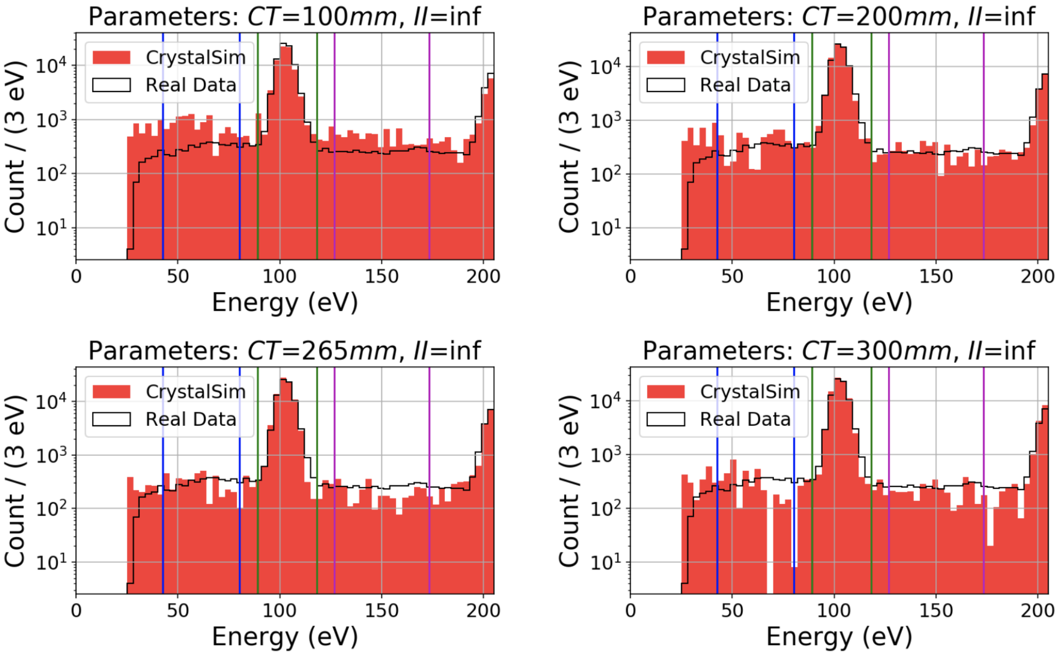

Figure 9.6: This figure shows how we estimate the mean free path value for charge trapping. The black curve shows the E_{Phonon} distribution for the data and the red shows the simulation. Also indicated with the vertical blue, green and magenta lines are the regions used to determine those values which are given in Table 9.2. The II MFP is set to infinity (impact ionization is turned off) while we have simulated four different values of the CT MFP (100 mm, 200 mm, 265 mm, and 300 mm) to determine which best describes the data below the first peak. This quantitative comparison is shown in Figure 9.7 and the final CT MFP value is 265 mm.

do for the large energy regions in Figure 9.12.

Purpose	**Param**	**Energy range**	**Data**	**Sim**
Events below the first peak	R1	42 eV < E_{Phonon} < 80 eV	4257	4219
Events in the first peak	R2	89 eV < E_{Phonon} < 118 eV	80264	82686
Events between the first and the second peaks	R3	126 eV < E_{Phonon} < 173 eV	4314	4751
Ratio of events below first peak and in first peak	R1/2	-	0.0530	0.0510
Ratio of events between first and second peak and in first peak	R3/2	-	0.0537	0.0574

Table 9.2: This table summarizes the regions and ratios used to determine the crystal impurity parameters. The ratios R1/2 and R3/2 are used to determine the final CT MFP and II MFP parameter values.

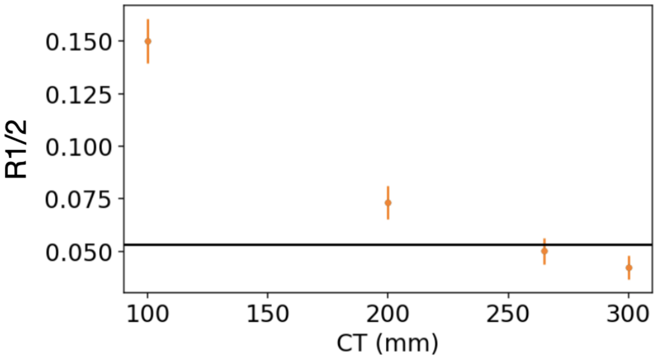

Figure 9.7: The plot of the ratio of the number of events in the regions below and in the first peak as described in Table 9.2 as a function of charge trapping mean free path (CT MFP) for the custom laser and the data shown in Figure 9.6. The solid black line shows the R1/2 for real data. We get the best match between data and simulation for CT MFP = 265 mm.

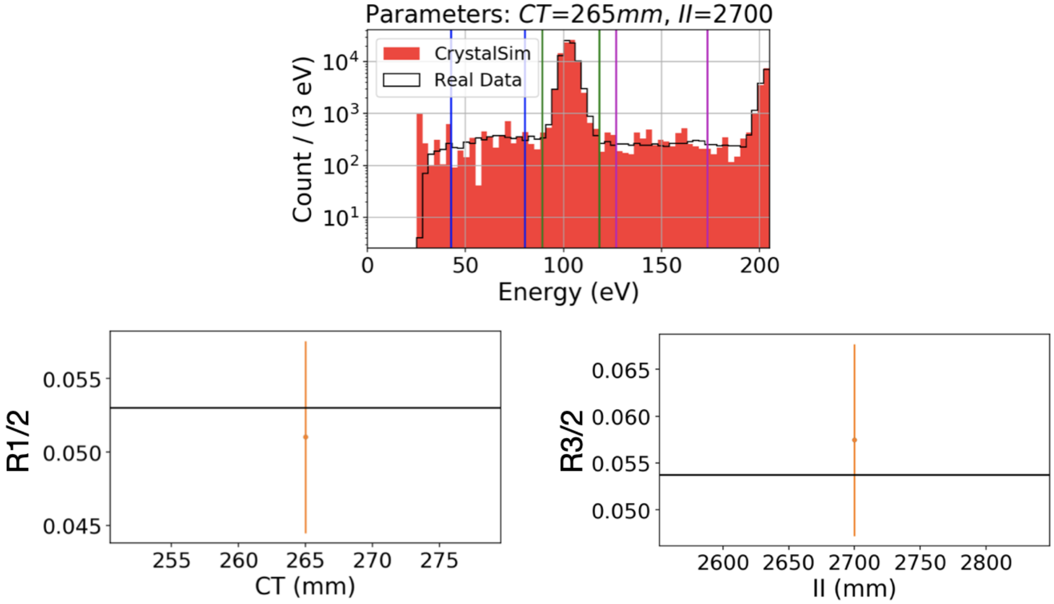

Figure 9.8: A comparison between the E_{Phonon} distribution from the real data and the simulation with the final CT MFP and II parameters (top) and two plots showing that the values of the chosen CT MFP and II MFP reproduce the ratio of events in the data for the regions below and above the first peak (bottom). We take 265 mm and 2700 mm as the final CT MFP and II MFP values, respectively. The observed number of events between the higher energy peaks, as shown in Figure 9.12 gives us confidence that the simulation is working as expected.

9.3.4 Energy Calibration

After determining the custom laser weights, the trigger threshold, and the CT/II MFP values, we turn to the calibration of the energy measurement of the simulated data. In Chapter 5, we learned that calibration is required because of the non-linear TES response. Using the methods of Figure 5.1 and Equation 5.1, we find the final values for our simulated data to be: $a = 601$ and $b = 0.115$. We note that our calibration constants for the simulation are close to the real data which vary on a day-by-day basis but an example of the calibration constants for the data are $a = 603$ and $b = 0.095$. Figure 9.9 shows the distributions before and after calibration but before the additional energy smearing. The right plot also contains the data and shows a good match except that the RMS of the peaks is smaller in the simulation. In the next section, we consider this difference and add additional energy smearing to the simulation to get a better match between the data and the simulation.

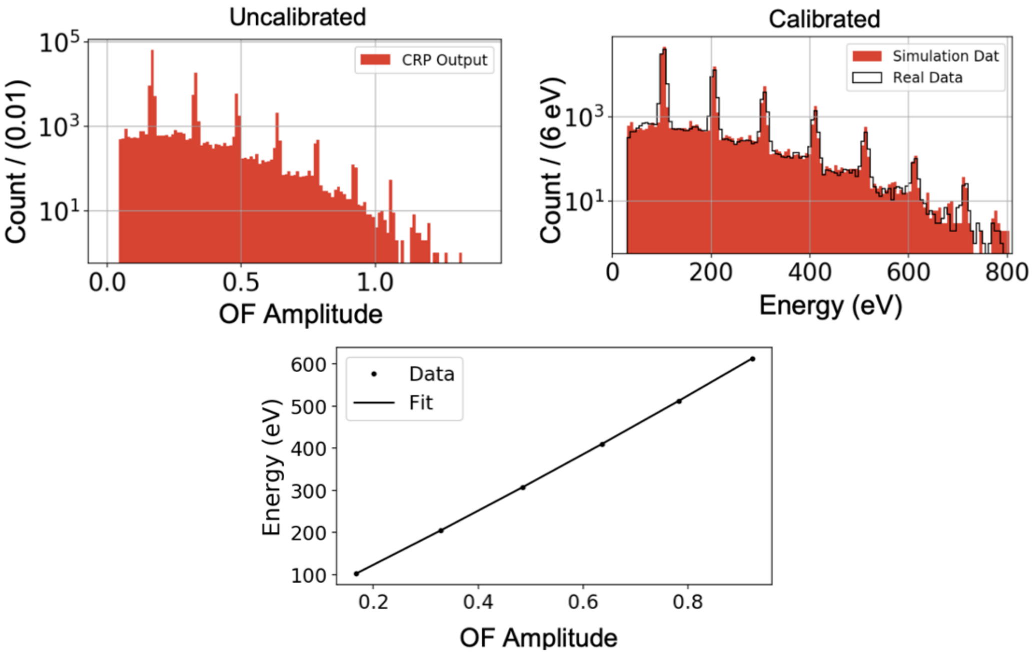

Figure 9.9: This figure shows the distributions of A_{OF} and E_{Phonon} using the full custom laser model and the final values of all the parameters except the additional energy smearing. Calibration is done using the same functional form from Equation 5.1 and yields value of $a = 601$ and $b = 0.115$. The comparison to data shows good agreement except for the RMSs of the peaks.

9.3.5 Additional Energy Smearing

In this section, we consider the differences between the RMS of the peaks in the data and the simulation and what we can learn from it. We start with fitting the first six electron-hole pair peaks shown in Figure 9.9 to Gaussian functions for both data and simulation. The results for the RMSs, along with the reported uncertainties, are shown in Figure 9.10.

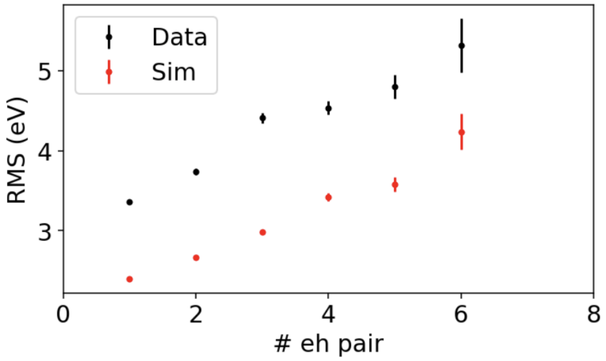

Figure 9.10: A comparison between the RMS of the first six electron-hole peaks for the data and simulation with all but the additional energy smearing as shown on the right-hand side of Figure 9.9. We add the additional energy smearing to take into account the fact that the width of the peaks is systematically smaller in the simulation.

The differences between the data and simulation in Figure 9.10 show that there is likely something important missing in our simulations. Not only are the differences substantive, but they show an important trend when we take the differences in quadrature as shown in Figure 9.11. The first thing we note is that there is approximately 2.5 eV of in-quadrature difference for the first peak. This suggests that, whatever the missing effect in simulations is, it is the dominant contributor to the RMS compared to the results of Table 8.2.

The second thing we note is that the data is consistent with a linearly rising trend as a function of energy, which suggests we are missing something from our simulation. A large but constant difference would have suggested that the noise had somehow been underestimated. The fact that

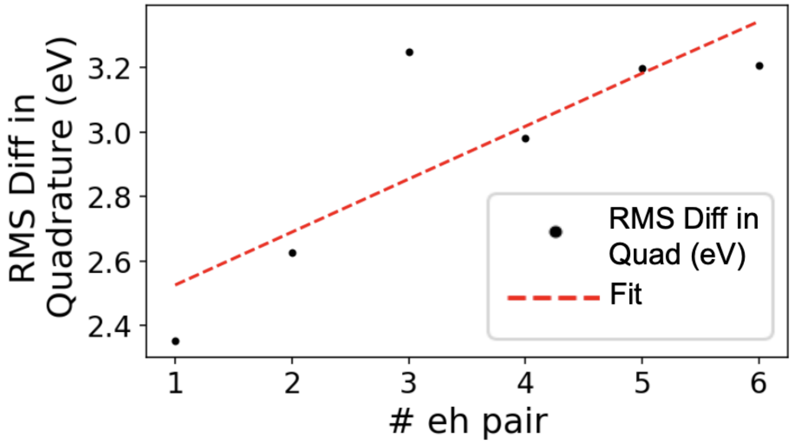

Figure 9.11: The difference in quadrature between the RMS values in Figure 9.10 along with a linear fit to the results. We take *Additional Energy Smearing* = $(0.0016 \cdot E_{phonon} + 2.36)$.

it rises with energy further suggests that it is probably an effect that has statistical variation i.e., correlated with the number of phonons or quasiparticles. For example, if there were a mechanism of energy loss in the QET, or some other inefficiency in the way energy is transferred from the aluminum to the tungsten. Since the addition of new effects to the simulation is beyond the scope of this work, we simply model this additional contribution by smearing the energy distribution as a function of energy. Using the values in Figure 9.11 and the best-fit linear function we add the following Gaussian smearing to the simulated data: *Additional Energy Smearing* = $(0.0016 \cdot E_{phonon} + 2.36)$

Figure 9.12 shows the comparison between the data and the full simulation result using the final parameters given in Table 9.1. As shown in the figure, our result shows a good match between the data and the simulation. In the next section, we present a quantitative comparison between the data and the simulation.

9.4 Final Data and Simulation Comparison

In this section, we present quantitative comparisons between the data and the final simulation results. We start with comparing the number of events in various regions of interest. We then fit the peak regions to Gaussian functions and compare the calculated fit parameters for the data and

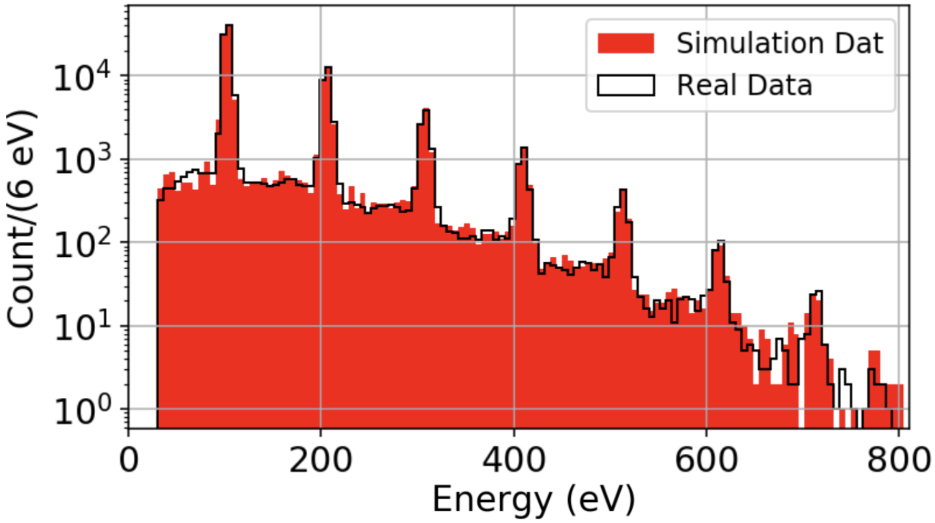

Figure 9.12: The final comparison between E_{Phonon} distribution from the real data and the full simulation with all the final parameter values, including additional energy smearing. We see a good match between the two by eye.

the simulation. We note at the outset that some of these comparisons should be taken with a grain of salt because of the number of by-hand parameters involved. Similarly, since best-fit methods were not used because of the iterations involved, a full estimate of the degrees of freedom is not possible.

Figure 9.13 shows a number of regions of interest, the number of events in each region, and a comparison between the number of events in the data and simulation. In particular, the bottom plot shows the number of events in the data and the simulation using the regions which are marked with blue lines in the top plot. The right plot shows the difference between the data and the simulation for the ten regions. We see good agreement with the possible exception that another iteration of the number of events in the custom laser simulation might have helped.

Another effective method for comparing the simulation and the data is fitting the electron-hole pair peaks to Gaussian functions and then comparing the calculated fit parameters (Amplitude, Mean, and RMS) for the data and the simulation. Figure 9.14 shows the results for the first electron-hole peaks for the data (left) and the simulation (right). Figure 9.15 shows the results as a function

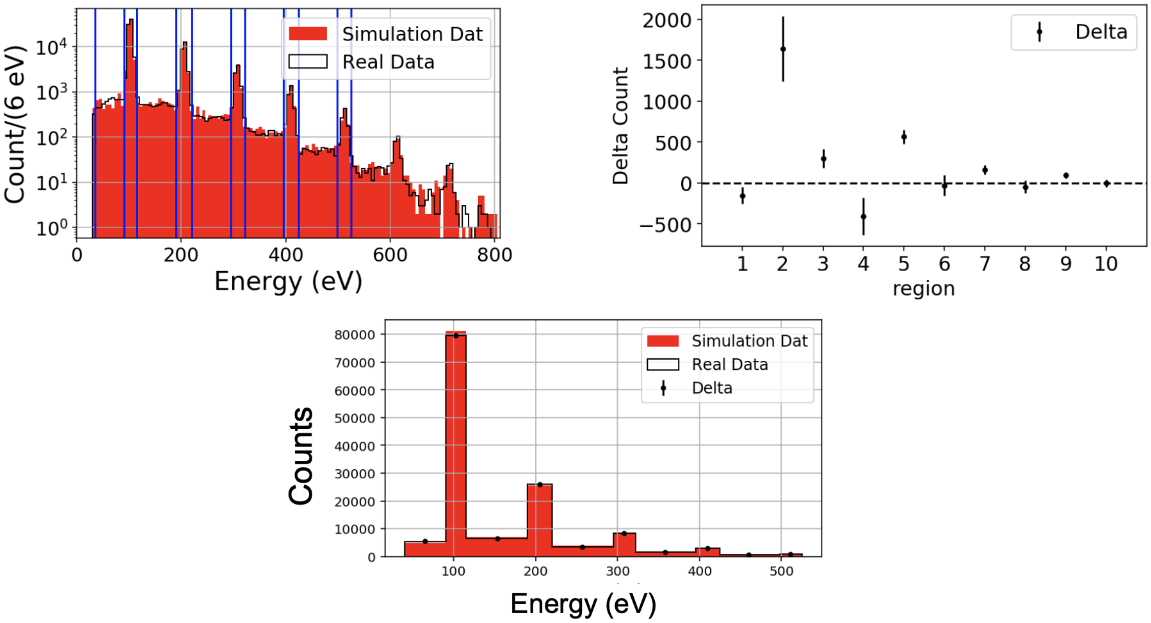

Figure 9.13: This figure shows three comparisons between the E_{Phonon} distribution from the HVeV laser data and the simulation after all tunings. The top left shows the spectrum and ten custom ranges. The bottom left shows the number of events in each region. The plot on the right shows the difference between the simulation and the data for each range.

of the number of electron-hole pairs. As shown in the figure, there is a good match between the data and the simulations. The differences are plotted in Figure 9.16, which shows that the simulation matches with data and shows no discernible trend. The χ^2 values for the Mean, and RMS are 13.7 and 11.2 for the six points respectively.

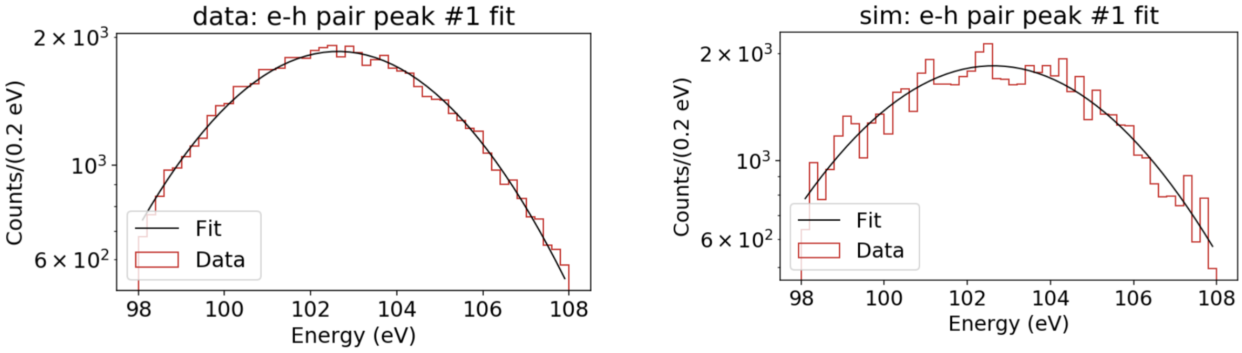

Amp = 66962 +- 258
Mean = 102.635 +- 0.018
RMS = 3.358 +-0.022

Amp = 67797 +- 260
Mean = 102.624 +- 0.018
RMS = 3.450 +-0.024

Figure 9.14: This figure shows the fitting results for the first of the electron-hole peaks in Figure 9.12 to a Gaussian function for the data (left) and the simulation (right). The calculated fit parameters (Amplitude, Mean, and RMS) along with the corresponding uncertainties are noted in the plots.

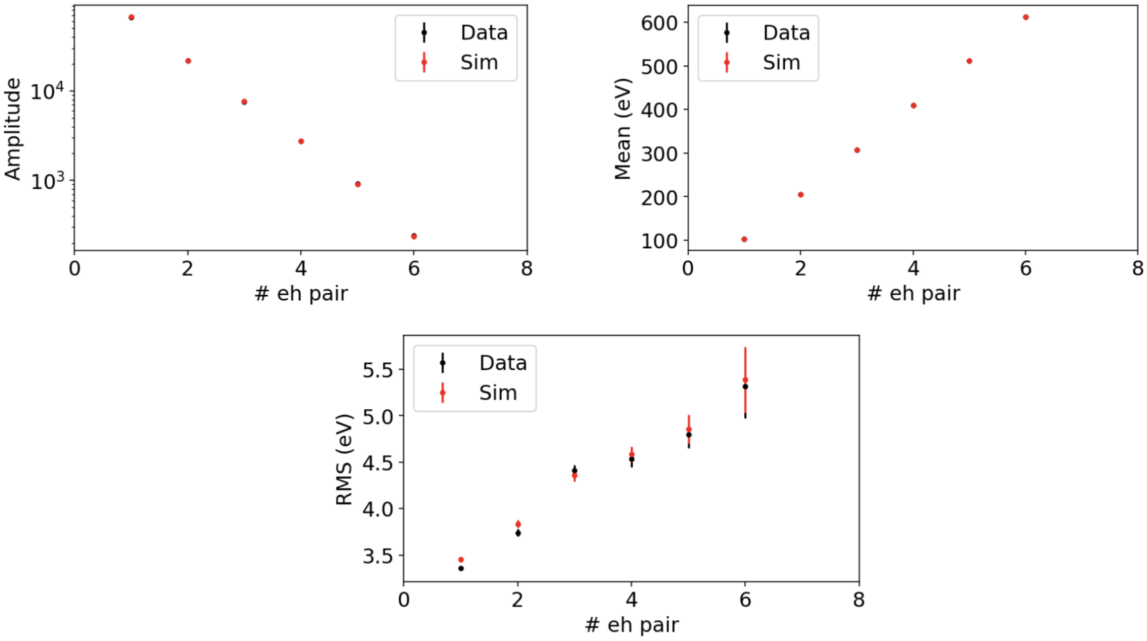

Figure 9.15: The calculated fit parameters (Amplitude, Mean, and RMS) for the simulation and the data as a function of the number of electron-hole pairs from Figure 9.12. There is a good match between the simulation and the data for amplitude and mean. The differences are shown in Figure 9.16.

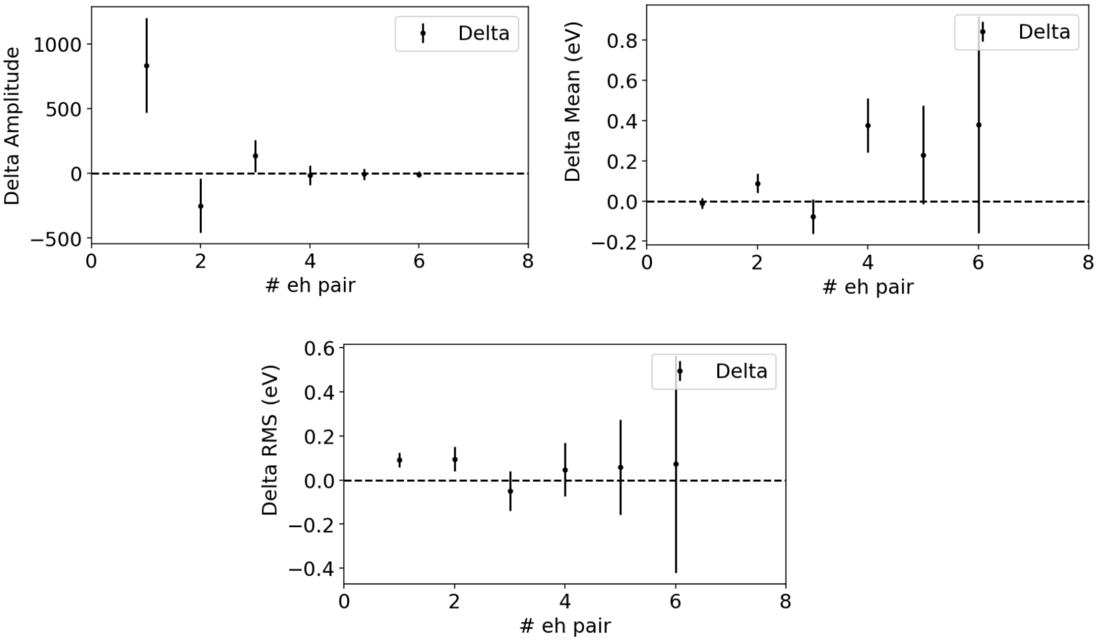

Figure 9.16: Differences between the calculated fit parameters (Amplitude, Mean, and RMS) for simulation and data as a function of the number of electron-hole pairs.

9.5 Summary

In this chapter, we used a combination of the tuned standard tools from the full simulation infrastructure as well as some custom tools to reproduce the real data with simulations. In general, we were able to get good qualitative and quantitative agreement especially in the high energy regions where many of the predictions are extrapolations. On the other hand, the methods show that there are a number of things we do not understand. For example, the Poisson laser model did not well describe the data. Similarly, we saw that the resolution of the simulation was significantly below that of the data. Perhaps more importantly, the observation that the difference between data and simulation rises with energy suggests there may well be mechanisms for energy loss that are not modeled in our simulations.

10. Conclusions

Now that our study has come to a close, we turn to summarize our important findings and their limitations in light of our main goals described in Section 1.8. We also present some thoughts regarding upcoming work on the SuperCDMS simulation program as well as future directions for using simulations in dark matter searches.

Understanding the nature of dark matter and detecting it in an experiment has been a long-term goal of scientists. In recent years, there has been a focus on searching for lower-mass dark matter candidates, which requires enhanced detector technologies. The SuperCDMS program, and its high voltage detectors, are well-equipped for searching lower-mass dark matter candidates because they are sensitive to low-energy interactions at $\mathcal{O}(1\ \mathrm{eV})$. However, expanding our sensitivity reach to lower dark matter masses is particularly challenging because our understanding of the new detector technologies and the physics at these low energies is limited. Learning more about the physics of the processes that become dominant at these energies can be accomplished through the use of fully-validated simulations. In this work, we studied eV photon interactions with HVeV detectors using simulations.

Through the use of our powerful simulation infrastructure, our understanding of low-energy interactions with the HVeV detector has significantly improved. We have verified that our baseline understanding of the detector provides a good qualitative agreement with the data. The data is well-described by the photons liberating a single electron-hole pair in a silicon crystal, and that the Luke amplification and phonon collection methods using QETs work as expected. We were also able to show that if we model the impurities with a mean free path of charge trapping and impact ionization, we improve our agreement and understanding of the physics.

The ability to separate these effects, and turn them on and off, allowed us to estimate the relative importance of each. Our studies/results show that electronic noise, crystal impurities, and multiple photons from the laser have the biggest contribution to the energy measurement resolution (RMS of the electron-hole pair peaks).

On the other hand, the full set of tools and the high-quality qualitative agreement allow us to see more clearly the places where more work is needed to get better quantitative agreement. The biggest example is that while we assumed our laser should be sending out photons with a number density that should follow a Poisson distribution, that clearly did not describe our data. It may be that the laser was not functioning as designed or something else was going on. Either way, our use of a custom laser simulation was able to get agreement.

Perhaps, the most important issue is that our simulation clearly did not reproduce the TES signal shape correctly with the default parameterization, nor did the full set of effects we simulated provide a full accounting of the RMS of the peaks. This suggests that the tuning of the TES description parameters was not correct. We note that after this work was completed, a re-turning of the parameters was able to get a much closer agreement. However, doing so did not worsen the resolution. In fact, it made it better, suggesting that there may be a full class of processes that are not yet simulated.

We are not surprised that we are missing things in the simulations. For example the Geant4 package, at the time of running, did not include the ability to simulate the interactions between eV photons and silicon. While we simulated this by approximating the photon response as a simple electron recoil energy deposit, and it seemed to be fine, it may well be that this is not as good an approximation as we hoped. Work on this task is in progress as well.

In conclusion, this work establishes that simulations can be used to effectively model most of the important aspects of the SuperCDMS dark matter search program. As such, it lays the groundwork for using simulations in the next dark matter searches with the HVeV detectors as well as their successors. It gives us hope that when we simulate the more difficult sources of backgrounds for our detectors, we will be able to cope with them using that better understanding. With that, the next generation of researchers are well-prepared to simulate the dark matter interactions with the detectors and conduct an optimized simulation-based dark matter search. We are well-situated to make a major discovery.

REFERENCES

[1] E. Corbelli and P. Salucci, “The extended rotation curve and the dark matter halo of M33,” *Monthly Notices of the Royal Astronomical Society*, vol. 311, no. 2, pp. 441–447, 2000.

[2] L. Bergstrom, “Dark matter evidence, particle physics candidates and detection methods,” *Annalen der Physik*, vol. 524, no. 9-10, pp. 479–496, 2012.

[3] R. Nemiroff and J. Bonnell, “A Horseshoe Einstein Ring from Hubble.” [Online]. Available: https://apod.nasa.gov/apod/ap111221.html

[4] M. Williams, “Astronomers figure out how to use gravitational lensing to measure the mass of white dwarfs.” [Online]. Available: https://www.universetoday.com/138832/astronomers-figure-use-gravitational-lensing-measure-mass-white-dwarfs

[5] M. Markevitch, A. Gonzalez, D. Clowe *et al.*, “Direct constraints on the dark matter self-interaction cross section from the merging galaxy cluster 1E 0657–56,” *The Astrophysical Journal*, vol. 606, no. 2, p. 819, 2004.

[6] D. Clowe, M. Bradač, A. H. Gonzalez *et al.*, “A direct empirical proof of the existence of dark matter,” *The Astrophysical Journal*, vol. 648, no. 2, p. L109, 2006.

[7] P. A. Ade, N. Aghanim, M. Arnaud *et al.*, “Planck 2015 results-XIII. Cosmological parameters,” *Astronomy & Astrophysics*, vol. 594, p. A13, 2016.

[8] J. Sander, Z. Ahmed, A. Anderson *et al.*, “SuperCDMS status from Soudan and plans for SNOLAB,” in *AIP Conference Proceedings*, vol. 1534, no. 1. American Institute of Physics, 2013, pp. 129–135.

[9] M. R. Buckley and P. J. Fox, “Dark matter self-interactions and light force carriers,” *Physical Review D*, vol. 81, no. 8, p. 083522, 2010.

[10] A. Boveia and C. Doglioni, “Dark matter searches at colliders,” *Annual Review of Nuclear and Particle Science*, vol. 68, pp. 429–459, 2018.

[11] S. Maestre, “What’s Fermi level and why is it important in a semiconductor?” [Online]. Available: https://www.circuitbread.com/ee-faq/whats-fermi-level-and-why-is-it-important-in-a-semiconductor

[12] J. Singleton, *Band theory and electronic properties of solids*. Oxford University Press, 2001.

[13] R. A. Moffatt, “Two-dimensional spatial imaging of charge transport in Germanium crystals at cryogenic temperatures,” Ph.D. dissertation, Stanford University, 2016.

[14] R. Ren, C. Bathurst, Y. Chang *et al.*, “Design and characterization of a phonon-mediated cryogenic particle detector with an eV-scale threshold and 100 keV-scale dynamic range,” *Physical Review D*, vol. 104, no. 3, p. 032010, 2021.

[15] SuperCDMS Collaboration, “SuperCDMS technical design report.” [Online]. Available: https://supercdms-docdb.fnal.gov/cgi-bin/private/RetrieveFile?docid=2316&filename=supercdms-snolab-fdr.pdf&version=1

[16] J. D. Morales Mendoza, “Simulation of the charge measurements for the SuperCDMS Soudan experiment,” Ph.D. dissertation, Texas A&M University, 2020.

[17] D. Amaral, T. Aralis, T. Aramaki *et al.*, “Constraints on low-mass, relic dark matter candidates from a surface-operated SuperCDMS single-charge sensitive detector,” *Physical Review D*, vol. 102, no. 9, p. 091101, 2020.

[18] HVeV Run 2 Analysis Group, “HVeV Run 2 Summary Documentation.” [Online]. Available: https://confluence.slac.stanford.edu/display/CDMS/HVeV+Run+2+Summary+Documentation+v2

[19] J. Allison, K. Amako, J. Apostolakis *et al.*, “Geant4 developments and applications,” *IEEE Transactions on Nuclear Science*, vol. 53, no. 1, pp. 270–278, 2006.

[20] J. S. Wilson, H. M. z. Theenhausen, B. von Krosigk *et al.*, “The level-1 trigger for the SuperCDMS experiment at SNOLAB,” *Journal of Instrumentation*, vol. 17, 2022.

[21] M. J. Wilson, "A new search for low-mass dark matter and an examination and reduction of the uncertainty due to the photoelectric absorption cross section using a cryogenic Silicon detector with single-charge sensitivity," Ph.D. dissertation, University of Toronto, 2022.

[22] M. Herrero, "The standard model," in *Techniques and Concepts of High Energy Physics X*. Springer, 1999, pp. 1–59.

[23] A. Maeder, "An alternative to the ΛCDM model: The case of scale invariance," *The Astrophysical Journal*, no. 2, p. 194, 2017.

[24] T. Padmanabhan, *Structure formation in the universe*. Cambridge University Press, 1993.

[25] T. Treu and R. S. Ellis, "Gravitational lensing: Einstein's unfinished symphony," *Contemporary Physics*, vol. 56, no. 1, pp. 17–34, 2015.

[26] Particle Data Group, "Review of particle physics," *Progress of Theoretical and Experimental Physics*, vol. 2020, no. 8, pp. 1–2093, 2020.

[27] L. Baudis, "Direct dark matter detection: The next decade," *Physics of the Dark Universe*, vol. 1, no. 1-2, pp. 94–108, 2012.

[28] R. Agnese, T. Aralis, T. Aramaki *et al.*, "First dark matter constraints from a SuperCDMS single-charge sensitive detector," *Physical Review Letters*, vol. 121, no. 5, p. 051301, 2018.

[29] G. P. Kuiper, "The empirical mass-luminosity relation." *The Astrophysical Journal*, vol. 88, p. 472, 1938.

[30] E. F. Bell, D. H. McIntosh, N. Katz *et al.*, "The optical and near-infrared properties of galaxies. I. luminosity and stellar mass functions," *The Astrophysical Journal Supplement Series*, vol. 149, no. 2, p. 289, 2003.

[31] M. Klasen, M. Pohl, and G. Sigl, "Indirect and direct search for dark matter," *Progress in Particle and Nuclear Physics*, vol. 85, pp. 1–32, 2015.

[32] M. Persic, P. Salucci, and F. Stel, “The universal rotation curve of spiral galaxies—I. The dark matter connection,” *Monthly Notices of the Royal Astronomical Society*, vol. 281, no. 1, pp. 27–47, 1996.

[33] S. Dye and S. Warren, “Decomposition of the visible and dark matter in the Einstein ring 0047–2808 by semilinear inversion,” *The Astrophysical Journal*, vol. 623, no. 1, p. 31, 2005.

[34] D. Fixsen, “The temperature of the cosmic microwave background,” *The Astrophysical Journal*, vol. 707, no. 2, p. 916, 2009.

[35] J. Silk, *The big bang*. Macmillan, 2000.

[36] P. Peebles, “Recombination of the primeval plasma,” *The Astrophysical Journal*, vol. 153, p. 1, 1968.

[37] S. Dodelson, *Modern cosmology*. Elsevier, 2003.

[38] NOVA, “Universe timeline.” [Online]. Available: https://www.pbs.org/wgbh/nova/universe/historysans.html

[39] S. D. White, M. Davis, and C. S. Frenk, “The size of clusters in a neutrino-dominated universe,” *Monthly Notices of the Royal Astronomical Society*, vol. 209, no. 1, pp. 27–31, 1984.

[40] A. Cuoco, M. Krämer, and M. Korsmeier, “Novel dark matter constraints from antiprotons in light of AMS-02,” *Physical Review Letters*, vol. 118, no. 19, p. 191102, 2017.

[41] E. Charles, M. Sanchez-Conde, B. Anderson *et al.*, “Sensitivity projections for dark matter searches with the Fermi large area telescope,” *Physics Reports*, vol. 636, pp. 1–46, 2016.

[42] P. Jackson, N. Soni, M. Alam *et al.*, “Search for dark matter candidates and large extra dimensions in events with a jet and missing transverse momentum with the ATLAS detector,” *Journal of High Energy Physics*, vol. 17, no. 4, pp. 075–075, 2013.

[43] D. Abercrombie, N. Akchurin, E. Akilli *et al.*, “Dark matter benchmark models for early LHC run-2 searches: report of the ATLAS/CMS dark matter forum,” *Physics of the Dark Universe*, vol. 27, p. 100371, 2020.

[44] J. Grym, *Semiconductor technologies*. BoD–Books on Demand, 2010.

[45] C. Yao and Y. Ma, “Superconducting materials: Challenges and opportunities for large-scale applications,” *Iscience*, vol. 24, no. 6, p. 102541, 2021.

[46] F. Sauli, *Gaseous radiation detectors: fundamentals and applications*. Cambridge University Press, 2014, no. 36.

[47] G. F. Knoll, *Radiation detection and measurement*. John Wiley & Sons, 2010.

[48] P. Luke, “Voltage-assisted calorimetric ionization detector,” *Journal of Applied Physics*, vol. 64, no. 12, pp. 6858–6860, 1988.

[49] R. Agnese, A. Anderson, T. Aramaki *et al.*, “Projected sensitivity of the SuperCDMS SNOLAB experiment,” *Physical Review D*, vol. 95, no. 8, p. 082002, 2017.

[50] M. Albakry, I. Alkhatib, D. Amaral *et al.*, “A strategy for low-mass dark matter searches with cryogenic detectors in the SuperCDMS SNOLAB facility,” *arXiv preprint arXiv:2203.08463*, 2022.

[51] S. Chatrchyan, V. Khachatryan, A. M. Sirunyan *et al.*, “Observation of a new boson at a mass of 125 GeV with the CMS experiment at the LHC,” *Physics Letters B*, vol. 716, no. 1, pp. 30–61, 2012.

[52] F. Abe, H. Akimoto, A. Akopian *et al.*, “Observation of top quark production in p p collisions with the collider detector at Fermilab,” *Physical Review Letters*, vol. 74, no. 14, p. 2626, 1995.

[53] Z. Hong, R. Ren, N. Kurinsky *et al.*, “Single electron–hole pair sensitive silicon detector with surface event discrimination,” *Nuclear Instruments and Methods in Physics Research*

Section A: Accelerators, Spectrometers, Detectors and Associated Equipment, vol. 963, p. 163757, 2020.

[54] N. Ashcroft, N.D. Mermin, *Solid state physics*. Saunders College Publishing, 1976.

[55] B. K. Ridley, *Quantum processes in semiconductors*. Oxford University Press, 2013.

[56] B. M. Askerov, *Electron transport phenomena in semiconductors*. World Scientific, 1994.

[57] C. Kittel and P. McEuen, *Introduction to solid state physics*. John Wiley & Sons, 2018.

[58] C. A. Klein, "Bandgap dependence and related features of radiation ionization energies in semiconductors," *Journal of Applied Physics*, vol. 39, no. 4, pp. 2029–2038, 1968.

[59] G. Wang, "Phonon emission in Germanium and Silicon by electrons and holes in applied electric field at low temperature," *Journal of Applied Physics*, vol. 107, no. 9, p. 094504, 2010.

[60] B. Neganov and V. Trofimov, "Colorimetric method measuring ionizing radiation," *Otkryt. Izobret*, vol. 146, no. 215, p. 53, 1985.

[61] H. J. Maris, "Phonon propagation with isotope scattering and spontaneous anharmonic decay," *Physical Review B*, vol. 41, no. 14, p. 9736, 1990.

[62] S. Tamura, J. Shields, and J. Wolfe, "Lattice dynamics and elastic phonon scattering in Silicon," *Physical Review B*, vol. 44, no. 7, p. 3001, 1991.

[63] B. Cabrera, S. Leman, K. McCarthy *et al.*, "CDMS Detector Monte Carlo Documentation." [Online]. Available: https://gitlab.com/supercdms/DMC/CDMS_DetectorMC/-/blob/master/CDMS_DMC_Manual.pdf

[64] K. McCarthy, "Detector simulation and WIMP search analysis for the Cryogenic Dark Matter Search experiment," Ph.D. dissertation, Massachusetts Institute of Technology, 2013.

[65] F. Ponce, W. Page, P. Brink *et al.*, "Modeling of impact ionization and charge trapping in SuperCDMS HVeV detectors," *Journal of Low Temperature Physics*, vol. 199, no. 3, pp. 598–605, 2020.

[66] F. Ponce, C. Stanford, S. Yellin *et al.*, “Measuring the impact ionization and charge trapping probabilities in SuperCDMS HVeV phonon sensing detectors,” *Physical Review D*, vol. 101, no. 3, p. 031101, 2020.

[67] V. L. Ginzburg and L. D. Landau, “On the theory of superconductivity,” in *On superconductivity and superfluidity*. Springer, 2009, pp. 113–137.

[68] E. Kaxiras, *Atomic and electronic structure of solids*, 2003.

[69] K. D. Irwin, S. W. Nam, B. Cabrera *et al.*, “A quasiparticle-trap-assisted transition-edge sensor for phonon-mediated particle detection,” *Review of Scientific Instruments*, vol. 66, no. 11, pp. 5322–5326, 1995.

[70] K. Irwin, “An application of electrothermal feedback for high resolution cryogenic particle detection,” *Applied Physics Letters*, vol. 66, no. 15, pp. 1998–2000, 1995.

[71] N. Kurinsky, “The low-mass limit: Dark matter detectors with eV-scale energy resolution,” Ph.D. dissertation, Stanford University, 2018.

[72] B. A. Hines, K. M. Sundqvist, D. N. Seitz *et al.*, “Flux-coupled direct feedback in a SQUID amplifier,” *IEEE Transactions on Applied Superconductivity*, vol. 21, no. 3, pp. 262–266, 2010.

[73] E. Gatti and P. F. Manfredi, “Processing the signals from solid-state detectors in elementary-particle physics,” *La Rivista del Nuovo Cimento*, vol. 9, no. 1, pp. 1–146, 1986.

[74] J. Clarke, “SQUIDs,” *Scientific American*, vol. 271, no. 2, pp. 46–53, 1994.

[75] M. Battaglieri, A. Belloni, A. Chou *et al.*, “US cosmic visions: new ideas in dark matter 2017: community report,” *arXiv preprint arXiv:1707.04591*, 2017.

[76] M. Albakry, I. Alkhatib, D. Amaral *et al.*, “Investigating the sources of low-energy events in a SuperCDMS-HVeV detector,” *Physical Review D*, vol. 105, no. 11, p. 112006, 2022.

[77] K. M. Sundqvist, “Carrier transport and related effects in detectors of the Cryogenic Dark Matter Search,” Ph.D. dissertation, Carrier transport and related effects in detectors of the Cryogenic Dark Matter Search, 2012.

[78] G. Jellison Jr, “Optical functions of Silicon determined by two-channel polarization modulation ellipsometry,” *Optical Materials*, vol. 1, no. 1, pp. 41–47, 1992.

[79] C. Jacoboni, *Theory of electron transport in semiconductors: a pathway from elementary physics to nonequilibrium Green functions*. Springer Science & Business Media, 2010, vol. 165.

[80] S. W. Leman, “Invited Review Article: Physics and Monte Carlo techniques as relevant to cryogenic, phonon, and ionization readout of Cryogenic Dark Matter Search radiation detectors,” *Review of Scientific Instruments*, vol. 83, no. 9, p. 091101, 2012.

[81] E. M. Purcell and D. J. Morin, *Electricity and magnetism*. Cambridge University Press, 2013.

[82] J. S. Wilson, “Notes on TES simulation.” [Online]. Available: https://confluence.slac.stanford.edu/download/attachments/120202114/notes-tes-simulation.pdf

[83] H. J. Nussbaumer, “The fast Fourier transform,” in *Fast Fourier Transform and Convolution Algorithms*. Springer, 1981, pp. 80–111.

[84] R. Agnese, Z. Ahmed, A. Anderson *et al.*, “Silicon detector results from the first five-tower run of CDMS II,” *Physical Review D*, vol. 88, no. 3, p. 031104, 2013.

APPENDIX A

DETECTOR RESPONSE AS A FUNCTION OF INTERACTION POSITION

Since there is a well-known effect in all the SuperCDMS detectors that we will not get a full phonon energy measurement when a particle interaction happens close to the detector sidewalls [84], it is useful to study this for the HVeV detectors. Specifically, for any electron created near the sidewall, there is a good chance that the crystal lattice constraints, described in Section 2.4 will cause the electron to hit the sidewall and be absorbed. Thus, we do not get the full Luke amplification and consequently, we will not get a full energy measurement.

Since the study of the different parts of the detector is important for using the HVeV detectors in searches for dark matter, it is important to understand which parts provide a good measurement and which do not. In the HVeV laser calibration experiment, the laser coverage was approximately uniform for R < 3 mm and centered on the top surface of the detector. While this is good for studying the well-measured region, it means there is not much data for interactions near the sidewalls. However, using simulations we can generate particle interactions near the sidewall and study them.

In this appendix, we use simulations to study the detector response as a function of interaction position. In particular, we determine the detector regions with full phonon energy measurement. In the next appendix, we focus on a detector observable and what it can tell us about the interaction position.

A.1 Sample Descriptions and Detector Response

In this appendix and the next, we use two samples for understanding which regions of the HVeV detector provide a full phonon energy measurement and what we can learn from the detector observable described in the next Appendix. The first sample, described here, is used to study the response in the full XY plane, and the second, described in the next appendix, is to study the response as a function of the depth of the detector (in the Z direction).

For the first sample we use a configuration that is identical to Table 7.1 with the exception that 30 k events are simulated, the photon interactions cover the full detector surface, but the Z location of all photon interactions is set to 1.9 mm (0.1 mm below the top surface) to avoid the surface absorption effects previously shown in Figure 7.5. Figure A.1 shows a scatter plot of the position of the photon interactions on the top surface of the detector in the XY plane, while Figure A.2 shows the distributions in the X, Y, and Z directions.

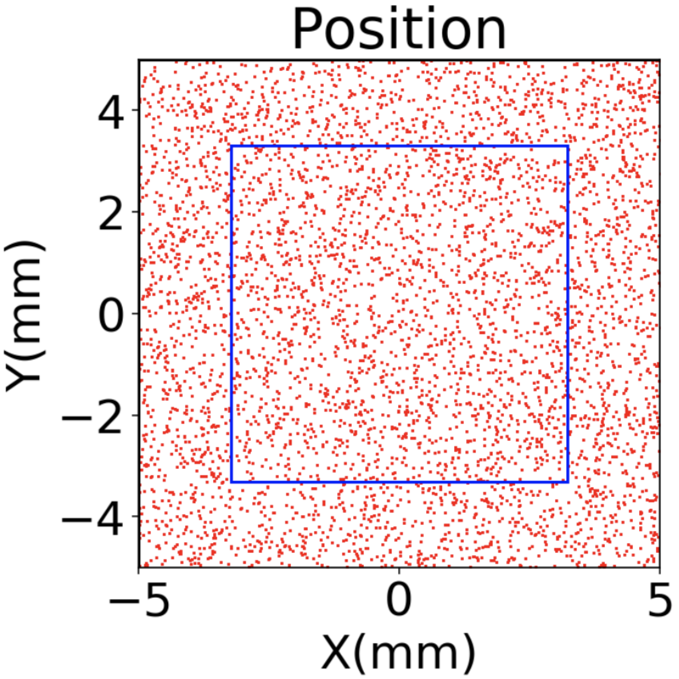

Figure A.1: This figure shows the position of the photon interactions for a sample of 30 k events using the same simulation configuration as Table 7.1, but extended to cover the full detector surface but restricted in the Z location to be at 1.9 mm, 0.1 mm below the top surface, so we do not get surface recombination effects as shown in Figure 7.5.

The E_{Phonon} distribution out of CrystalSim is shown in Figure A.3. As expected and seen in the plot, while the majority of the photon interactions create electron-hole pairs that go through the Luke amplification, some do not. Figure A.4 shows the collected phonon energy in Ch2 vs Ch1 with the left plot showing the full data and the right plot showing the results after removing all

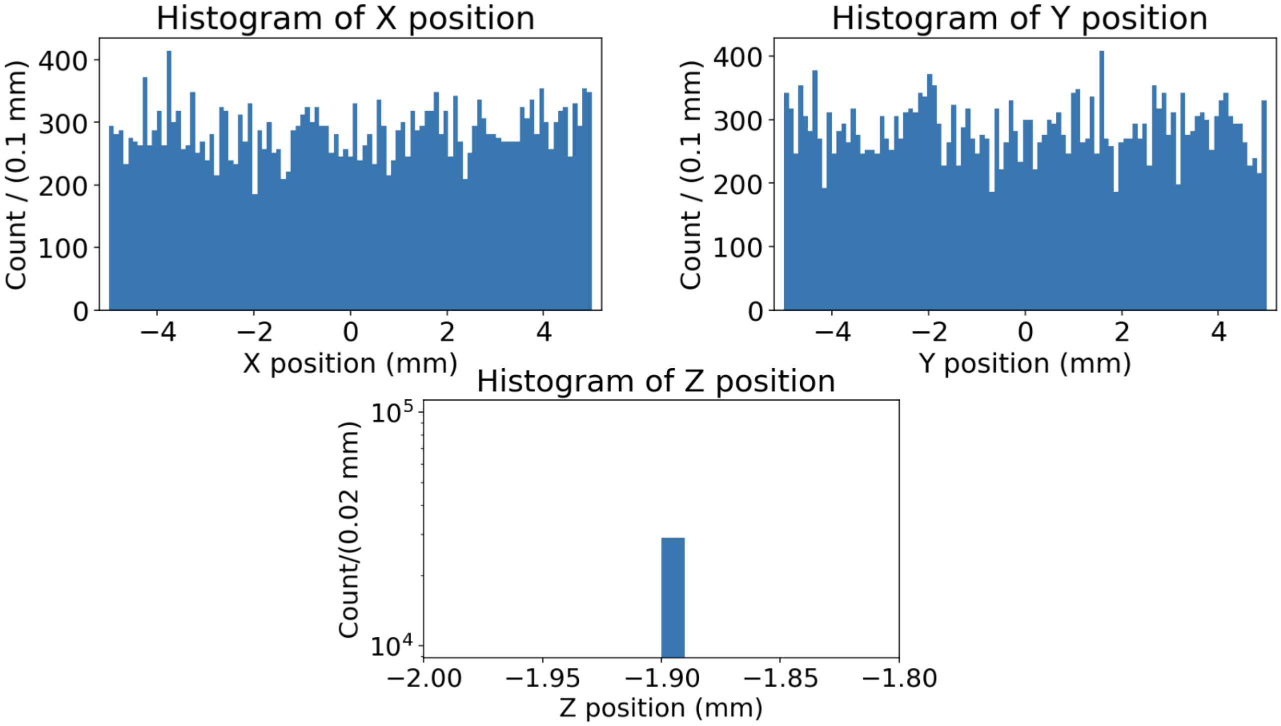

Figure A.2: The distribution of the position of the photon interactions for the sample of events shown in Figure A.1 as a function of interaction location. The events cover the full top surface of the detector and are positioned at Z = 1.9 mm.

events with a partial phonon energy collection ($E_{Phonon} < 101$ eV). We also see that there is more collected phonon energy in Ch1 when we have a full measurement, while in the case of a partial measurement, there is more collected phonon energy in Ch2. This indicates that partial measurements are most likely to happen when the photon interacts in Ch2, which is expected because Ch2 borders with the sidewalls. This observation is used in the following appendix when attempting to estimate the position of the interaction using detector observables.

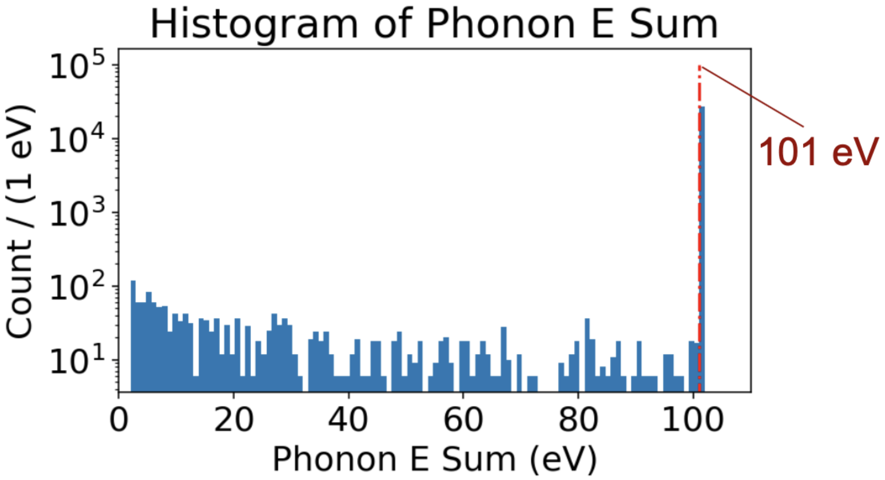

Figure A.3: The E_{Phonon} distribution from the sample of events shown in Figures A.1 and A.2, which shows that most, but not all, of the photon interactions produce full Luke amplification (end up in the first electron-hole pair peak).

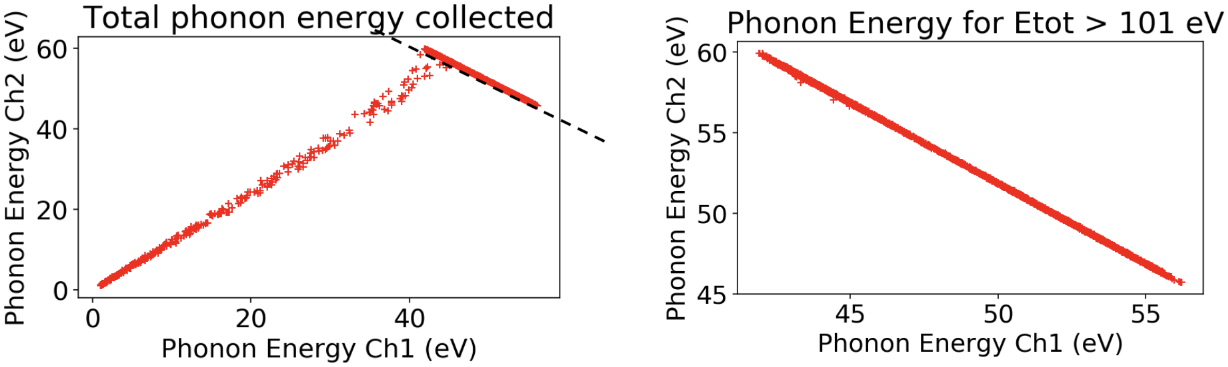

Figure A.4: These two plots show the relationship of E^{Ch2}_{Phonon} vs. E^{Ch1}_{Phonon} for the same sample of events. The left plot is the full data and the right plot is after removing all events with $E_{Phonon} <$ 101 eV, where we have a partial energy measurement.

A.2 Determining the Detector Regions with Full Phonon Energy Measurement

While we do not have a way to estimate the location of the interactions in the experiment, the simulation allows us to determine the regions of the detector where photon interactions get a full measurement. Figure A.5. shows the location of all of the events with $E_{Phonon} < 101$ eV. As expected, they are all near a sidewall of the detector; the distance to the nearest wall is plotted on the right-hand side of the figure showing all interactions have a distance of less than 0.6 mm from a sidewall. Since it is useful to have a simple way to select them for study in simulation, an effective approach to select fully-measured events is to require that events must be more than 0.6 mm away from a sidewall. We refer to the region of the detector where we get full measurements as the fiducial region and call the selection of them the fiducial cuts.

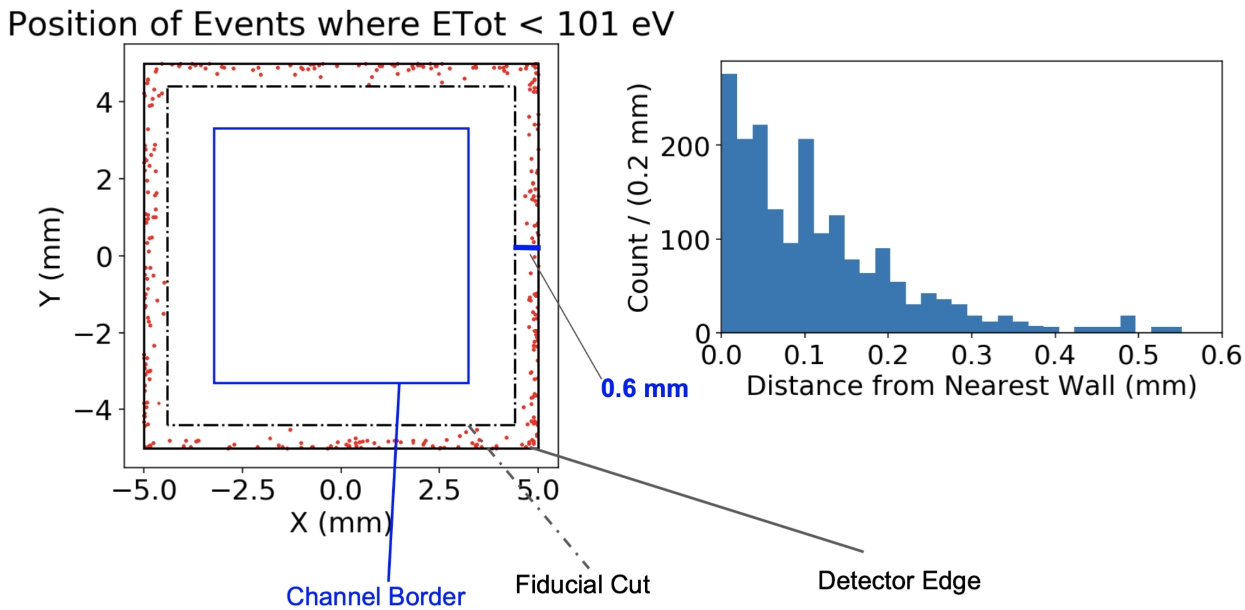

Figure A.5: This figure shows the position of the photon interactions that do not undergo full Luke amplification. The plot on the left shows the XY position of the photon interactions on the top surface of the detector for the events that did not get the full Luke amplification ($E_{Phonon} < 101$ eV). The plot on the right shows the distribution of the distances from the nearest wall for those events. All the events with a partial energy measurement are within 0.6 mm off of a sidewall. We note that requiring events to be further than 0.6 mm from a sidewall (which we can do in simulation but not in the real data) provides an effective way to select only fully-measured events. This is also known as applying a fiducial cut.

To study the effectiveness of the fiducial cut, we look at the heat plot of E_{Phonon}^{Ch2} and E_{Phonon}^{Ch1} before and after applying the fiducial cut, which are shown in Figures A.6 and A.7. As shown in Figure A.6, when the interaction occurs in the center of the detector, most of the phonon energy will be collected in Ch1. As the interaction happens farther away from the center, the amount of collected phonon energy drops until we get very close to the sidewalls, where we no longer get the full collection. Figure A.7 shows that all partially-measured events are removed after applying the fiducial cut confirming that our fiducial cut is effective. On the other hand, the cut removes $\sim 22\%$ of the data, but only $\sim 7\%$ are poorly-measured.

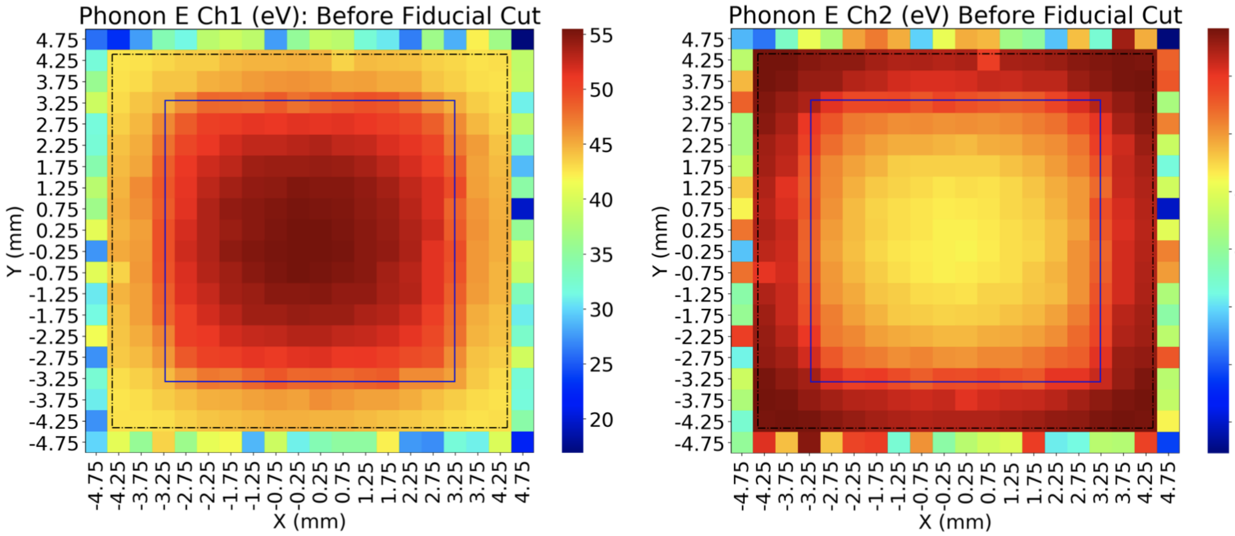

Figure A.6: This figure shows the two heat plots of the collected phonon energy of E_{Phonon}^{Ch1} and E_{Phonon}^{Ch2} before applying the fiducial cut. This is interesting because we see that when the event occurs in the center of the detector the majority of the event is deposited in Ch1 and the fraction in Ch1 drops as we move away from the center. The regions close to the sidewalls show significant energy loss.

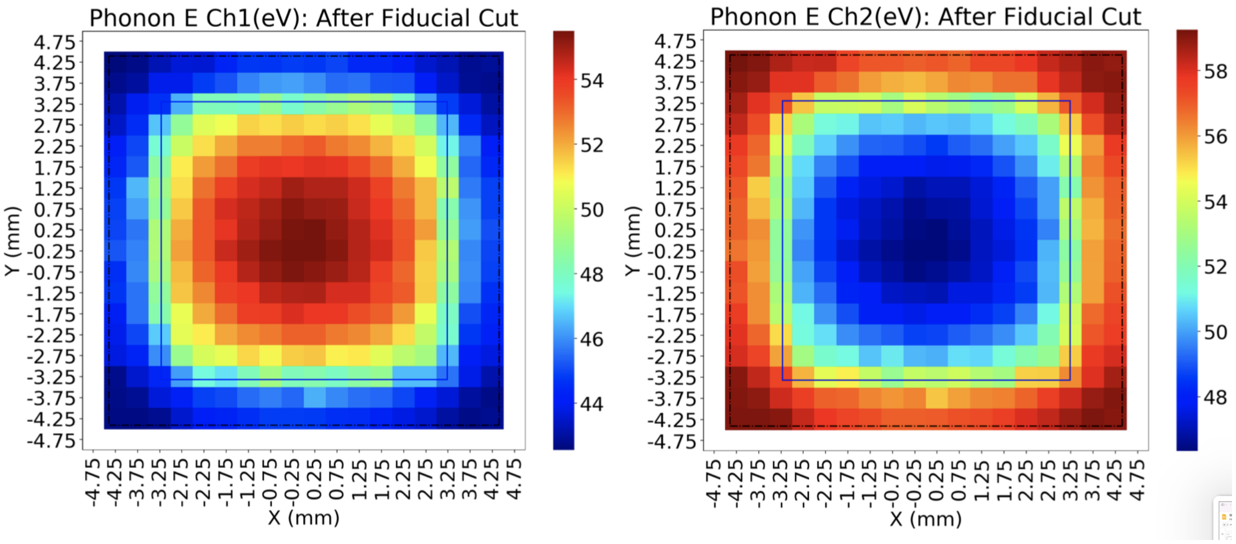

Figure A.7: This figure shows the two heat plots of the collected phonon energy of E^{Ch1}_{Phonon} and E^{Ch2}_{Phonon} after applying the fiducial cut (note the compressed heat map color representation), which confirms that the fiducial cut effectively removes the events with a partial energy measurement, which occurs when the energy deposit is close to a detector wall.

APPENDIX B

DETECTOR RESPONSE OBSERVABLE

While we have seen that we do not always get full Luke amplification when an interaction deposits energy in the detector, the differences between the inner and outer channel responses can be used to provide information about the interaction location. In this appendix we define an observable, called Asymmetry, and study how it changes as a function of the location of the particle interaction.

As shown in Figure A.7 the amount of energy in the two readout channels is a function of the position of the interaction. In particular as the distance from the center increases, more of the energy is deposited in Ch2 and less is deposited in Ch1. This can be quantified with a variable called Asymmetry, A, which we define via:

$$A = \frac{E^{Ch1}_{Phonon} - E^{Ch2}_{Phonon}}{E^{Ch1}_{Phonon} + E^{Ch2}_{Phonon}}. \tag{B.1}$$

While this variable will not be helpful for immediate recombination near the top surface of the detector, we see that a positive (negative) Asymmetry value indicates that the particle interaction happened near the detector center (sidewalls).

B.1 Asymmetry in XY Plane

We start by studying the Asymmetry dependence on the location of the particle interaction in the XY plane using the sample described in Section A.1. For doing so, we calculate the Asymmetry value for each event and study its dependence on location. Figure B.1 shows two scatter plots of the Asymmetry value (marked with colors) as a function of the position of the photon interaction before and after applying the fiducial cut. As seen in the plots, the value of Asymmetry is affected both by the distance of the interaction from the center (X = Y = 0) and also the detector geometry which has a square shape.

To understand this better, we look at the value of Asymmetry in cylindrical coordinates, where R is the distance from the Z-axis at the center of the detector, and theta is the angle from the positive X-axis. Figure B.2 shows two plots of the Asymmetry as a function of R before and after applying the fiducial cut. The result is interesting because the Asymmetry value clearly shows the Ch1 and Ch2 separation at $\sim$3 mm and applying the fiducial cut removes the particle interaction that happened near the sidewalls. On the other hand, simply rejecting all events with an Asymmetry below 0.0 would have also removed many well-measured events. For this reason, we consider the Asymmetry as we slice the data into regions of R and theta.

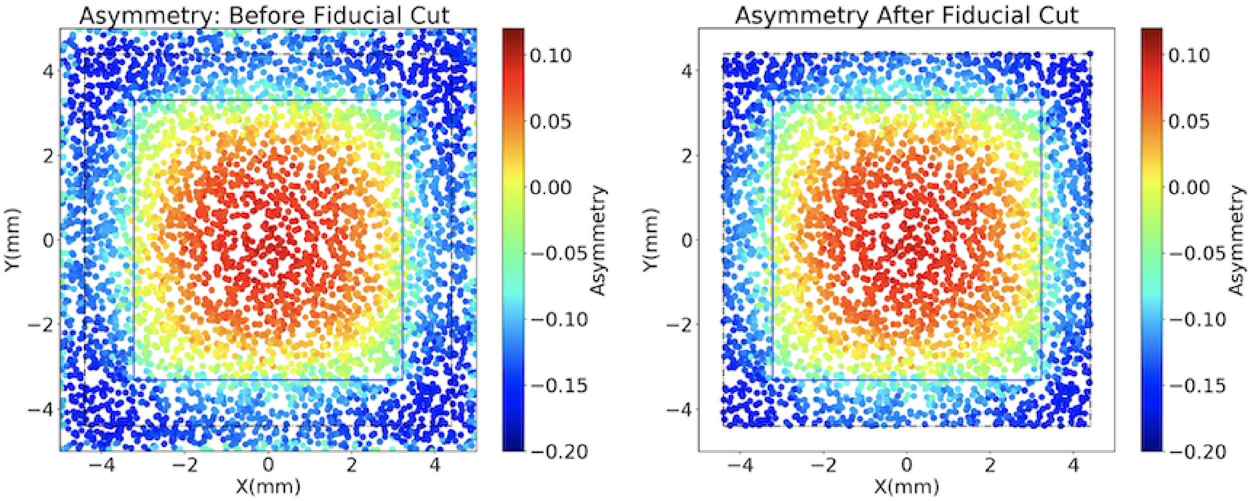

Figure B.1: This figure shows two scatter plots of the Asymmetry value (marked with colors) as a function of the position of the photon interaction in the XY plane before and after applying the fiducial cut for the sample described in Appendix A. As shown in the plots, the square-shaped detector geometry and the interaction's distance from the center of the detector (X = Y = 0) both have an impact on the value of Asymmetry.

The Asymmetry as a function of theta for slices of R, and as a function of R for slides of theta are shown in Figures B.3 and B.4. The corner effects can be seen more clearly in Figure B.3 where the Asymmetry is displayed as a function of theta for various ranges of R. As shown in these plots, for $R < 2$ mm, the Asymmetry is independent of theta, and the corner effects appear for $R > 2$ mm. Similarly, Figure B.4 shows a scatter plot with the location of the particle interaction

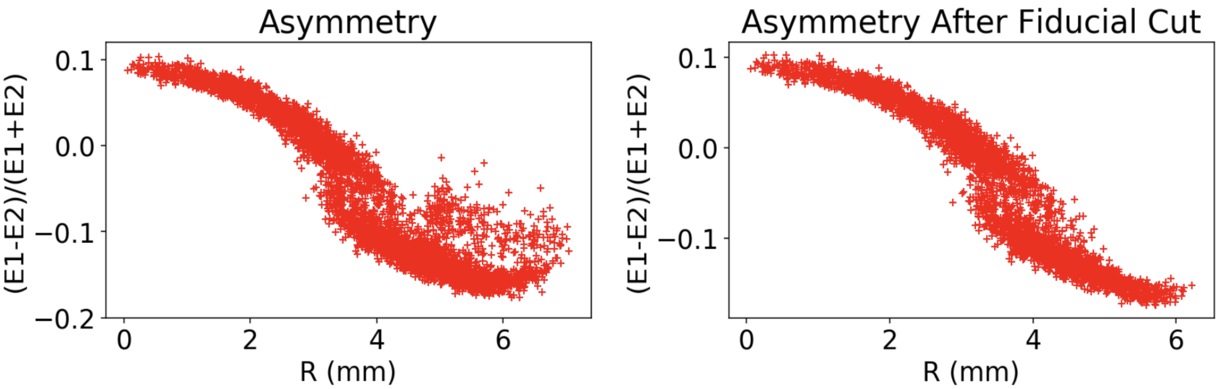

Figure B.2: Two plots showing the Asymmetry as a function of the distance of the particle interaction from the center of the detector (R) before and after applying the fiducial cut for the same sample as Figure A.1. The Ch1 and Ch2 separation is visible at $\sim\ 3\,\mathrm{mm}$. As shown in the plots, applying the fiducial cut removes the events that deposited energy near the sidewalls. Note that our detector has a square shape, which determines the shape of the Asymmetry as a function of R.

in cylindrical coordinate and the color-coded Asymmetry range that goes with it, along with the detector edges and the channel border marked with the black and blue solid lines. Before drawing conclusions, we consider what happens for other values of the Z interaction position.

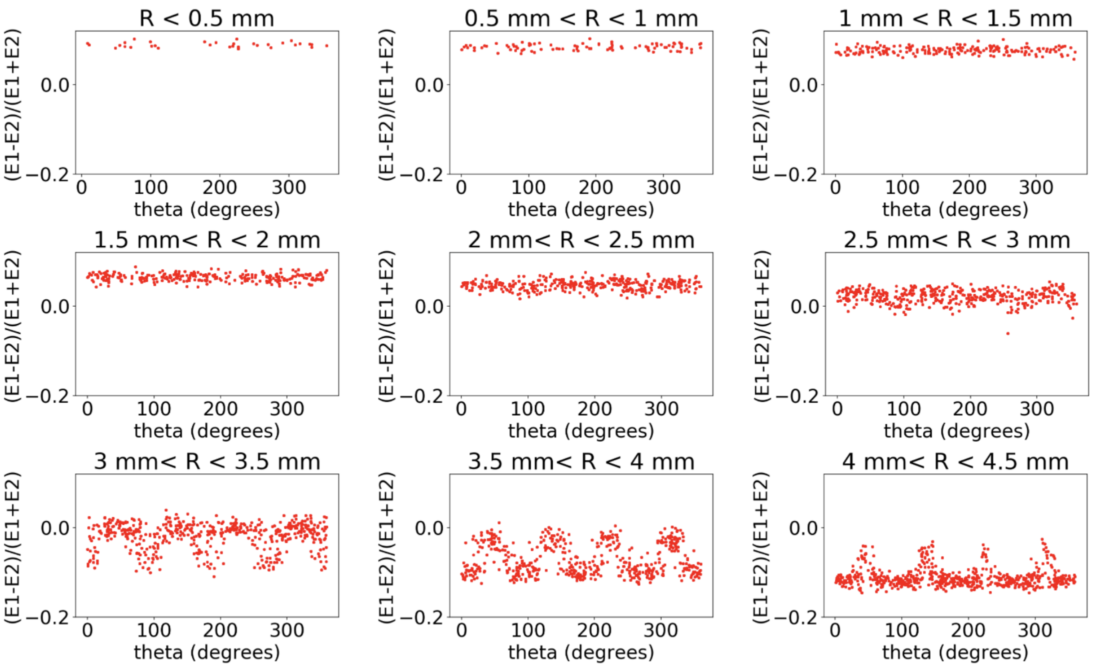

Figure B.3: Nine plots showing the Asymmetry as a function of angle (theta) for different ranges of R. These plots show that Asymmetry does not depend on theta for R < 2 mm and the corner effects emerge at R > 2 mm.

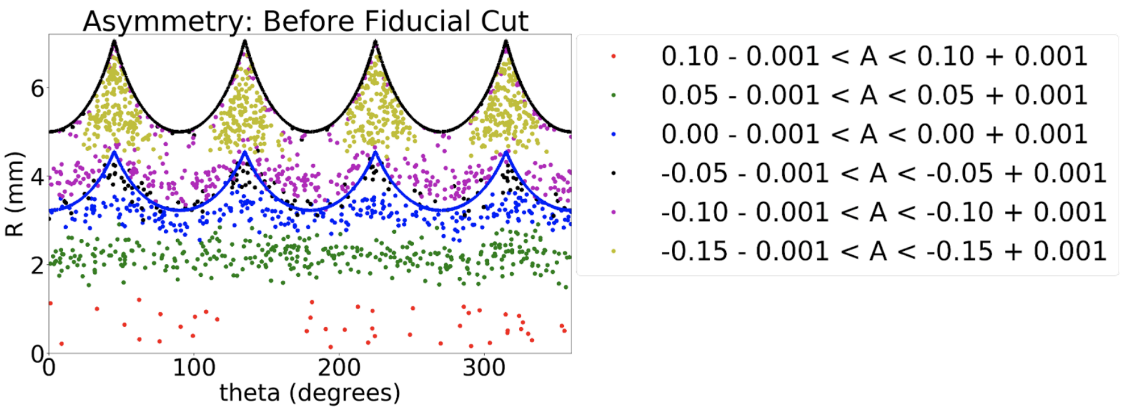

Figure B.4: A scatter plot of the position of the particle interaction in cylindrical coordinates and corresponding Asymmetry range marked with colors. This plot shows that for R < 2 mm the Asymmetry only depends on R, while for R > 2 mm the Asymmetry depends on both R and theta because of the corner effects. The black solid line shows the detector edges and the blue line shows the channel border.

B.2 Asymmetry in Z Direction

We next study the Asymmetry dependence on the location of the particle interaction in the Z direction. For doing so, as shown in Figure B.5, we simulate a sample of 3 k events with the same simulation configuration as Table 7.1 but, with R confined to R < 0.1 mm and Z covering the full depth of the detector (-2 mm < Z < 2 mm). The results are shown in Figure B.6, confirming that all of the particle interactions get full measurement as they are away from the detector sidewalls. Only a tiny fraction of events are so close to the top or bottom surface that they get absorbed before amplification so they can be neglected for this study. The E^{Ch1}_{Phonon} and E^{Ch2}_{Phonon} values as a function of the particle interaction position in the Z direction show that the measurement has a slight dependence on Z when the particle interaction occurs close to the QET sensor (Z = 2 mm). This can be understood from the trajectory of the charges in the crystal lattice, as well as the angle of emission of the Luke phonons as shown in Figure 2.3. Since some of the Luke phonons are absorbed by the QETs before reaching Ch2, the measured phonon energy in Ch1 is slightly greater near the top surface. The same effect is more clearly visible in the Asymmetry scatter and profile plots as a function of R and Z, shown in Figure B.7.

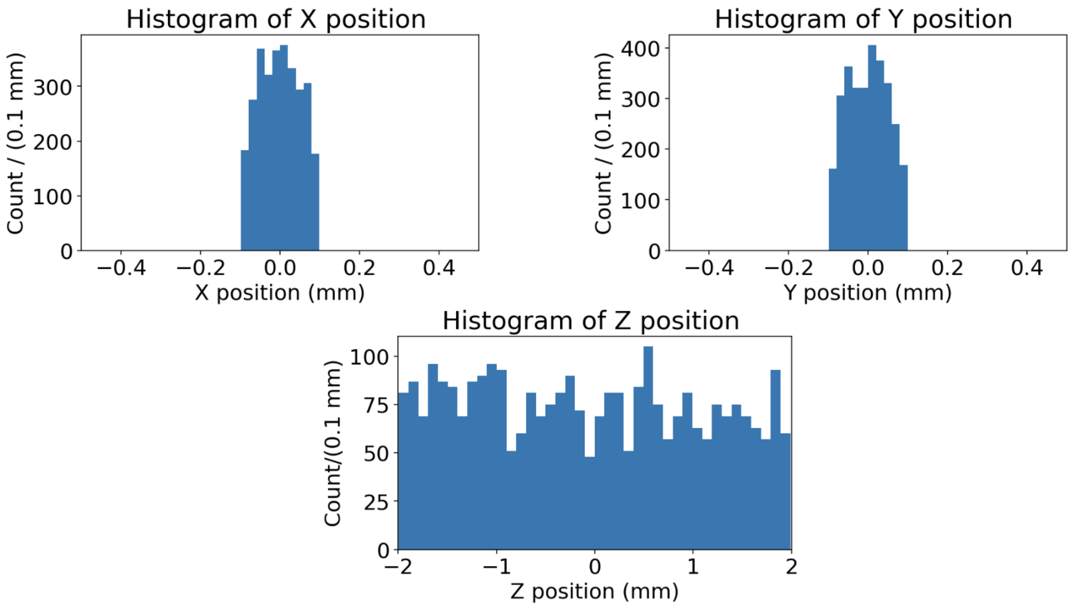

Figure B.5: The distribution of the positions of the particle interaction for a sample of events as a function of interaction location simulated for studying the Asymmetry dependence on Z. The simulation configuration is the same as Table 7.1 except that 3 k events are simulated and the particle interactions are confined to R < 0.1 mm and cover the full depth of the detector - 2 mm < Z < 2 mm.

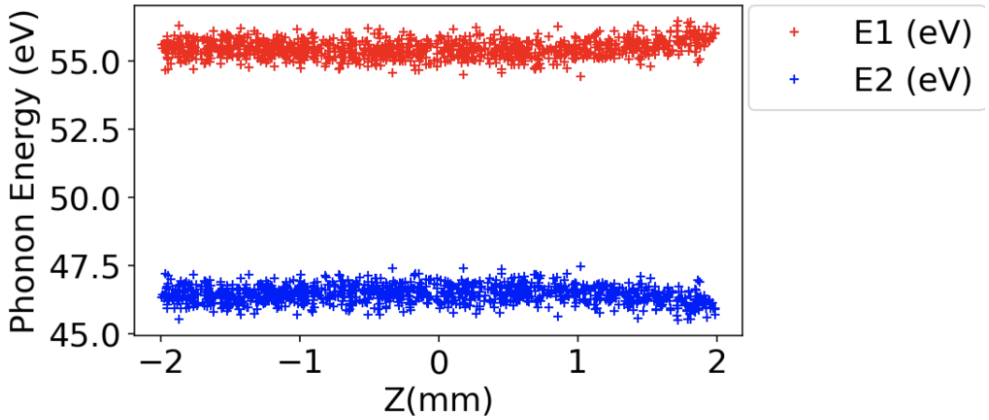

Figure B.6: This figure shows E^{Ch1}_{Phonon} and E^{Ch2}_{Phonon} values as function of the particle interaction position in the Z direction for the sample in Figure B.5. It shows that phonon energy measurement does not depend on Z except for the cases where Z is close to 2 mm, which is the top surface of the detector (where the QETs are placed). Near the top surface, the collected phonon energy in Ch1 is slightly larger because some Luke phonons get absorbed by the QET before making it to Ch2.

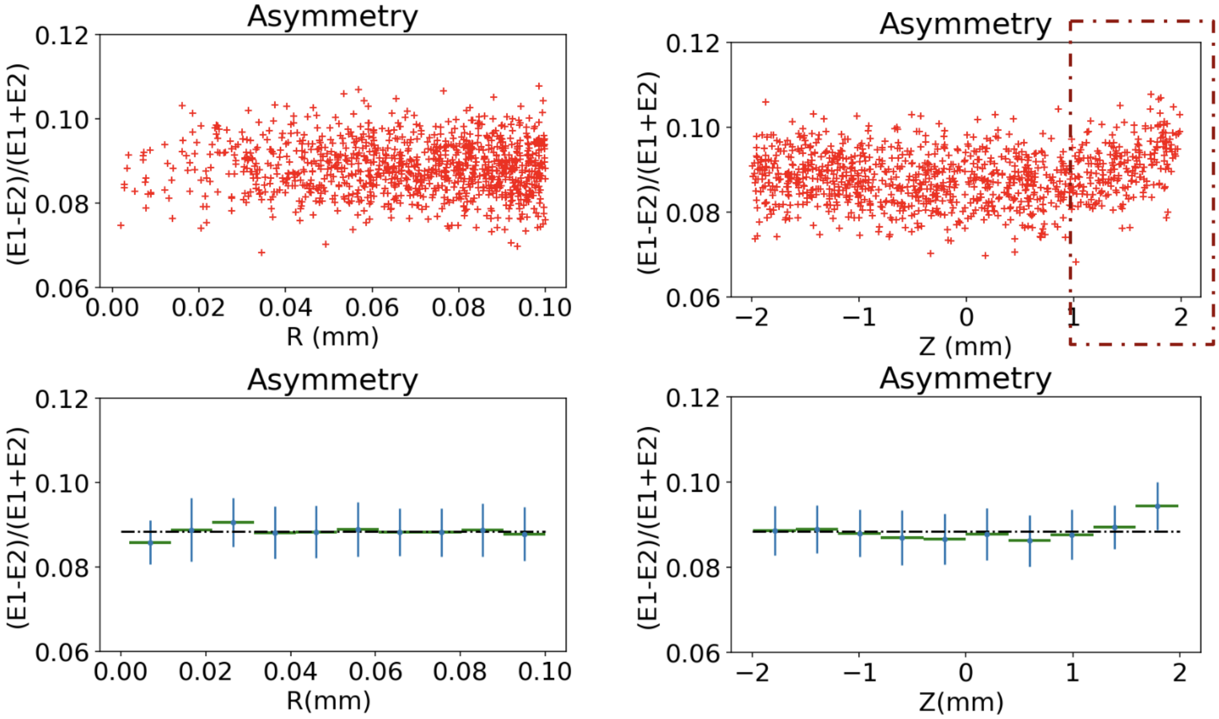

Figure B.7: This figure shows scatter plots (top) and profile plots (bottom) of the Asymmetry as a function R (left) and Z (right) for the sample of events in Figure B.5. As shown in the left plots, since all particle interaction are very close to the center of the detector in the XY plane, there is no dependence on R, which means we can isolate the effect of the position in the Z direction. As shown in the right plots, the Asymmetry has a Z dependence only for Z > 1 mm because in that case, more of the Luke phonons that originate close to the sensors are directly absorbed.

B.3 Conclusions

To summarize, using simulations we showed that the Asymmetry variable provides some information about the location of the interaction. While it is not terribly useful for the analysis of the laser data, where all the events occur near the center of the detector, an understanding of the measurement is crucial for dark matter searches, where interactions are expected to be uniform throughout the detector. From Appendix A we saw that only events within 0.6 mm of the surface of the detector are likely to be poorly-measured (either because of recombination of the electron-hole pair, or the electron hitting the sidewall as it moves through the lattice), these events can be removed with an Asymmetry cut. While our results show a simple cut of $A > 0$ would likely be effective for removing all events near a sidewall, and be fine for all values of Z, such a cut would remove a good number of our dark matter events as well. An optimization using this variable would require more knowledge about the backgrounds involved.